

AD-A168 373

ACTIVE CONTROL OF FORWARD SWEPT WINGS WITH DIVERGENCE  
AND FLUTTER AEROELA. (U) AIR FORCE INST OF TECH

1/2

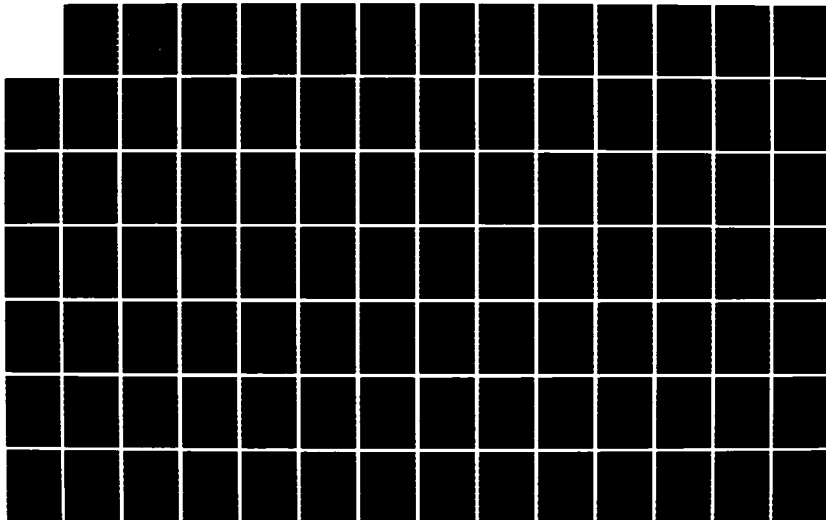
WRIGHT-PATTERSON AFB OH SCHOOL OF ENGI.. K E GRIFFIN

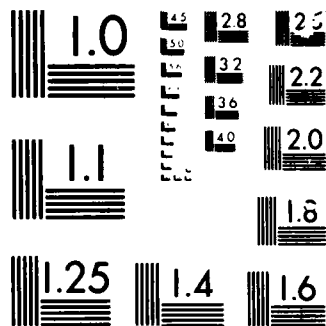
UNCLASSIFIED

81 MAY 84 AFIT/DS/AA/84-1

F/O 20/4

NL





MICROCOPY

CHART

AD-A168 373

AFIT/DS/AA/84-1

(1)

ACTIVE CONTROL OF FORWARD SWEPT WINGS  
WITH DIVERGENCE AND FLUTTER AEROELASTIC INSTABILITIES

DISSERTATION

AFIT/DS/AA/84-1

Kenneth E. Griffin  
Major USAF

DTIC  
ELE  
S JUN 9 1986  
A

AD-A151-897

DTIC FILE COPY

Approved for public release; distribution unlimited

086 56 2 107

# REPORT DOCUMENTATION PAGE

1a. REPORT SECURITY CLASSIFICATION Unclassified			1b. RESTRICTIVE MARKINGS None		
2a. SECURITY CLASSIFICATION AUTHORITY			3. DISTRIBUTION/AVAILABILITY OF REPORT Approved for public release; distribution unlimited		
2b. DECLASSIFICATION/DOWNGRADING SCHEDULE					
4. PERFORMING ORGANIZATION REPORT NUMBER(S) AFIT/DS/AA/84-1			5. MONITORING ORGANIZATION REPORT NUMBER(S)		
6a. NAME OF PERFORMING ORGANIZATION Air Force Inst. of Tech.		6b. OFFICE SYMBOL (If applicable) AA	7a. NAME OF MONITORING ORGANIZATION		
6c. ADDRESS (City, State and ZIP Code) Wright-Patterson AFB, Ohio 45433			7b. ADDRESS (City, State and ZIP Code)		
8a. NAME OF FUNDING/SPONSORING ORGANIZATION AFWAL		8b. OFFICE SYMBOL (If applicable) FIBA	9. PROCUREMENT INSTRUMENT IDENTIFICATION NUMBER		
8c. ADDRESS (City, State and ZIP Code) Wright-Patterson AFB, Ohio 45433			10. SOURCE OF FUNDING NOS.		
			PROGRAM ELEMENT NO.	PROJECT NO. <b>AEROELASTIC</b>	TASK NO. WORK UNIT NO.
11. TITLE (Include Security Classification) Active Control of Forward Swept Wings with Divergence and Flutter Instabilities (U)					
12. PERSONAL AUTHOR(S) Major Kenneth E. Griffin					
13a. TYPE OF REPORT Dissertation		13b. TIME COVERED FROM 1979 To 1984		14. DATE OF REPORT (Yr., Mo., Day) 84-05-01	
15. PAGE COUNT					
16. SUPPLEMENTARY NOTATION					
17. COSATI CODES			18. SUBJECT TERMS (Continue on reverse if necessary and identify by block number)		
FIELD	GROUP	SUB. GR.	Aeroelasticity, Aerodynamics, Control.		
01	03				
20	11				
19. ABSTRACT (Continue on reverse if necessary and identify by block number) Active feedback control is applied to cantilever forward-swept wings (FSW) providing significant increases in the critical airspeeds of aeroelastic flutter and divergence. Feedback compensation improves the critical airspeed for a divergence critical FSW by 25% and improves the critical airspeed for a flutter critical FSW example by 30%. These improvements are limited by the emergence as most critical, instabilities that were only secondary without feedback. The method of analysis is linear control theory in the Laplace domain. A significant improvement is made in the Padé Approximant method for calculating damped unsteady aerodynamic forces in the Laplace domain.					
20. DISTRIBUTION/AVAILABILITY OF ABSTRACT UNCLASSIFIED/UNLIMITED <input checked="" type="checkbox"/> SAME AS RPT <input type="checkbox"/> DTIC USERS <input type="checkbox"/>			21. ABSTRACT SECURITY CLASSIFICATION Unclassified		
22a. NAME OF RESPONSIBLE INDIVIDUAL Major Kenneth E. Griffin			22b. TELEPHONE NUMBER (Include Area Code) AV 350 3320		22c. OFFICE SYMBOL 6520 1st Grp/INAF

AFIT/DS/AA/84-1

ACTIVE CONTROL OF FORWARD SWEPT WINGS  
WITH DIVERGENCE AND FLUTTER AEROELASTIC INSTABILITIES

DISSERTATION

Presented to the Faculty of the School of Engineering  
of the Air Force Institute of Technology

Air University

in Partial Fulfillment of the  
Requirements for the Degree of  
Doctor of Philosophy

by

Kenneth E. Griffin, B.S., M.S.

Major

USAF

Approved for public release; distribution unlimited

ACTIVE CONTROL OF FORWARD SWEPT WINGS  
WITH DIVERGENCE AND FLUTTER AEROLASTIC INSTABILITIES

by

Kenneth E. Griffin, B.S., M.S.

Major

USAF

Approved:

*Franklin E. Easter* 2 May 1984  
Chairman  
*Ken J. Torunk* 2 May 84  
*Dennis W. Linn* 3 May 84  
*Robert A. Parker* 3 May 84

Accepted:

*J. J. Ziemieniec* 10 May 1984  
Dean, School of Engineering

Accession For	
NTIS	<input checked="checked" type="checkbox"/>
DTIC TAB	<input type="checkbox"/>
Unannounced	<input type="checkbox"/>
Justification	
Availability Codes	
Avail and/or	
Dist	Special
A-1	

DTIC  
COPY  
INSPECTED  
1

QUALITY  
INSPECTED  
3

## ACKNOWLEDGMENT

First and foremost this has been possible by Him who can make anything possible: "But if any of you lacks wisdom, he should pray to God, who will give it to him; because God gives generously and graciously to all."  
(James 1:5)

This work is dedicated to my wife Sandra, and my sons David and Michael. Their constant support, love, and understanding made it possible to follow through to the finish. My Mom and Dad, Lorraine and Joe Griffin, gave continued encouragement and inspired the patience necessary to continue on. Thanks also to my Advisory Committee chairman, Dr. F. E. Eastep; Committee Members: Dr. P. J. Torvik, Dr. R. Calico, Dr. D. W. Quinn, and former member Dr. D. W. Breuer.

A very special thanks to Mike Shirk of AFWAL for his sponsorship and support of this research. And finally, thanks to Ms. Erika Tucker for careful and patient typing of the manuscript and to Major Bob Hogge of the Department of English at the USAFA for helping to make it readable.

## Contents

	Page
Acknowledgements.....	iii
List of Figures.....	v
List of Tables.....	viii
List of Symbols.....	ix
Abstract.....	xiv
I. Introduction.....	1
a. Background.....	1
b. Aeroelastic Divergence And Flutter.....	4
c. Aeroelastically Tailored Composite Materials.....	5
d. Active Feedback Control.....	6
e. Approach.....	7
f. History.....	7
g. Overview.....	8
II. Wing Analysis.....	11
a. Equations Of Motion.....	11
b. Structural Representation.....	16
c. Aerodynamic Forces.....	22
d. Control Surface Aerodynamic Forces.....	29
e. Feedback Control Laws.....	34
f. Stability Solution Method.....	38
III. Wing Active Control Studies.....	43
a. Case 1 Study.....	48
1. Displacement Sensing.....	50
2. Velocity Sensing.....	61
3. Acceleration Sensing.....	65
4. Summary Of Case 1 Results.....	70
b. Case 2 Study.....	70
1. Displacement Sensing.....	71
2. Velocity Sensing.....	79
3. Acceleration Sensing.....	81
4. Summary Of Case 2 Results.....	85
IV. Conclusions.....	88
Bibliography.....	93
Appendix A Solution Method Evaluations Using 2-D Airfoil.....	A-1
Appendix B The Doublet-Lattice Method.....	B-1
Appendix C Wind Tunnel Correlations.....	C-1



### List of Figures

Figure		Page
1	Wing Sweep Effects On Critical Airspeeds For Flutter and Divergence Of A Typical Aircraft.....	3
2	Wing Geometry.....	13
3	Geometry For Cantilever Wing Planform And Structural Box....	18
4	Panel Geometry For The Wing Doublet-Lattice Aerodynamics....	26
5	Leading- And Trailing-Edge Flap Geometry.....	32
6	Feedback Loops For The Forward-Swept Wing Compensation.....	35
7	Sensor Locations For The Wing.....	45
8	Velocity Root Locus For Case 1..... No Feedback	49
9	Gain-Parameter Root Locus For Case 1..... Sensor D/Flap D	52
10	Gain-Parameter Root Locus For Case 1..... Sensor A/Flap A	53
11	Gain-Parameter Root Locus For Case 1..... Sensor D/Flap B	54
12	Velocity Root Locus For Case 1..... Sensor D/Flap B	56
13	Velocity Root Locus For Case 1..... Sensor D/Flap B	57
14	Velocity Root Locus For Case 1..... Sensor D/Flap B	58
15	Velocity Root Locus For Case 1..... Sensor D/Flap B	59
16	Velocity Root Locus For Case 1..... Sensor D/Flap B	60
17	Velocity Root Locus For Case 1..... Sensor D/Flap B	62
18	Gain-Parameter Root Locus For Case 1..... Sensor D/Flap A	63

19	Gain-Parameter Root Locus For Case 1.....	64
	Sensor D/Flap A	
20	Velocity Root Locus For Case 1.....	66
	Sensor D/Flap D	
21	Velocity Root Locus For Case 1.....	67
	Sensor D/Flap D	
22	Gain-Parameter Root Locus For Case 1.....	68
	Sensor A/Flap B	
23	Velocity Root Locus For Case 1.....	69
	Sensor A/Flap B	
24	Velocity Root Locus For Case 2.....	72
	No Feedback	
25	Gain-Parameter Root Locus For Case 2.....	74
	Sensor A/Flap B	
26	Velocity Root Locus For Case 2.....	75
	Sensor A/Flap B	
27	Velocity Root Locus For Case 2.....	76
	Sensor A/Flap B	
28	Velocity Root Locus For Case 2.....	77
	Sensor A/Flap B	
29	Gain-Parameter Root Locus For Case 2.....	78
	Sensor D/Flap A	
30	Gain-Parameter Root Locus For Case 2.....	80
	Sensor D/Flap D	
31	Velocity Root Locus For Case 2.....	82
	Sensor D/Flap D	
32	Gain-Parameter Root Locus For Case 2.....	83
	Sensor D/Flap A	
33	Velocity Root Locus For Case 2.....	84
	Sensor D/Flap A	
34	Velocity Root Locus For Case 2.....	86
	Sensor D/Flap A	
B1	Typical Doublet-Lattice Panel.....	B-3
A1	Geometry For The Airfoil.....	A-2
A2	Feedback Loops For The Airfoil Compensation.....	A-21

A3	Velocity Root For Case D.....	A-27
A4	Velocity Root For Case F.....	A-29
A5	Velocity Root For Case D.....	A-31
A6	Velocity Root For Case D.....	A-32
A7	Velocity Root For Case F.....	A-33
A8	Velocity Root For Case F.....	A-34
B1	Typical Doublet-Lattice Panel.....	B-3
C1	Wind Tunnel Model.....	C-2
C2	Velocity Root Locus For Wind Tunnel Model.....	C-6
C3	Velocity Root Locus For Wind Tunnel Model.....	C-7
C4	Velocity Root Locus For Wind Tunnel Model.....	C-8
C5	Velocity Root Locus For Wind Tunnel Model.....	C-9
C6	Sweep Effects On Section Angles-Of-Attack Due To Wing Loading.....	C-11

## List of Tables

Table		Page
I	Generalized Aerodynamic Influence Coefficient Comparisons For The Wing.....	30
A1	Comparisons Of Polynomial Orders For Padé Fit Of Aerodynamic $L_h$ .....	A-13
A2	Padé Polynomial Coefficients Of The Airfoil Before And After Denominator Averaging.....	A-15
A3	Comparisons Of Instability Predictions Using Different Data Arrays For The Padé Fit.....	A-18
A4	Physical Characteristics Of The Airfoil Examples.....	A-26
C1	Wind Tunnel Comparisons: Test Versus Analyses.....	C-4
C2	Wind Tunnel Model's Damping Derivatives.....	C-13

# List of Symbols

<u>Symbol</u>	<u>Definition</u>
$a$	gain subscript for acceleration
$\hat{a}$	vector containing wing states for its first-form
$\bar{\hat{a}}$	transformed $\hat{a}$
$a_i(t)$	time function for mode shape $i$
$\bar{a}_i(s)$	transformed $a_i(t)$
$\tilde{a}_{ij}$	aerodynamic influence coefficient relating the motion from coordinate $j$ to the force of coordinate $i$
$[A]$	matrix of generalized force influence coefficients for the wing performing simple harmonic motion
$[\tilde{A}]$	matrix of $\tilde{a}_{ij}$
$\hat{A}$	vector relating generalized forces on wing due to a flap deflection
$\bar{\hat{A}}$	transformed $\hat{A}$
$\bar{\tilde{A}}_{ij}$	transformed aerodynamic force influence coefficient
$[\hat{A}]$	first-order form matrix containing the influence coefficient matrices from the wing equations of motion
$b$	semichord
$ba$	airfoil shear center location
$bc$	airfoil leading-edge flap hinge-line location
$bd$	airfoil trailing-edge flap hinge-line location
$br_\alpha$	airfoil radius of gyration
$bx_\alpha$	airfoil c.g. location
$\mathcal{C}(k)$	Theodorsen function
$\bar{\mathcal{C}}(s)$	transformed Theodorsen function
$C_{l\alpha}$	airfoil lift-curve slope
$d$	gain subscript for displacement or index
$\hat{d}$	maximum denominator order of $s$ for polynomial approximation of $\bar{e}$

$\bar{d}_j$	radius of rotation at control point $j$ when a flap is deflected
$E_{1j}$	displacement of mode 1 at the $x,y$ location of point $j$
$f$	force function or an index
$F_i$	force on $i$ th panel of doublet-lattice aerodynamics
$F(x,y,t)$ aero	time dependant aerodynamic force on the wing at $x,y$
$F(x,y,t)$ dist	time dependant disturbance force on the wing at $x,y$
$h$	plunge displacement
$\bar{h}$	transformed $h$
$\bar{h}(x)$	vertical displacement of the chordline of the airfoil
$h_i(t)$	time dependant displacement at the $x,y$ location of the $i$ th control point in the doublet-lattice calculations
$\bar{h}_i(s)$	transformed $h_i(t)$
$h(x,y,t)$	time dependant displacement at location $x,y$ in the wing
$\bar{h}(x,y,s)$	transformed $h(x,y,t)$
$H_i^{(2)}$	second kind Hankel functions of $i$ th order
$H_{ij}$	feedback loop transfer function relating movement of flap $i$ due to measurement $j$
$\bar{H}_{ij}$	transformed $H_{ij}$
$i$	index or $(-1)^{1/2}$
$I_\theta$	airfoil pitch inertia about its shear center
$[I]$	identity matrix
$j$	index
$k$	reduced frequency
$k_{ij}$	element $ij$ of wing stiffness matrix
$k(x,y;\xi,\eta)$	stiffness influence on $x,y$ due to a displacement at $\xi,\eta$
$K_h$	airfoil plunge spring stiffness
$K_\theta$	airfoil pitch spring stiffness

$K_i$	modified second-kind Bessel function of $i$ th order or wing feedback gain using sensor type $i$
$K_{ij}$	gain constant relating flap $i$ to measurement $j$
$K_{ijl}$	gain constant relating flap $j$ to the $i$ th derivative of measurements taken at point $l$
$[K]$	wing or airfoil stiffness matrix
$l$	index
$L$	airfoil aerodynamic lift defined by Theodorsen
$\bar{L}$	transformed $L$
$\mathcal{L}$	Laplace transformation
$m$	index
$m_{ij}$	element $ij$ of wing mass matrix
$M_h$	total airfoil mass
$M_{sc}$	airfoil aerodynamic moment at the shear center defined by Theodorsen
$[M]$	wing or airfoil mass matrix
$n$	index
$\hat{n}$	maximum numerator order of $s$ in $\bar{e}$ approximation
$N$	number of natural vibration modes used as modal coordinates
$O(s)$	the highest order of $s$
$P_i$	Padé coefficient of $s^i$ in approximation
$P_{fjl}$	numerator polynomial coefficient for order $f$ of $s$ in the Padé Approximant for aerodynamic force influence coefficient $j,l$
$q$	dynamic pressure
$Q_i$	generalized force $i$ or denominator Padé coefficient of $s^i$ in approximation
$\bar{Q}_i$	transformed $Q_i$
$\tilde{Q}_i$	coefficient of $s^i$ in average denominator of Padé Approximant
$Q_{ij}$	influence on transformed generalized force $i$ due to coordinate $j$

$Q_{fjl}$	denominator polynomial coefficient for order $f$ of $s$ in the Padé Approximant for aerodynamic force influence coefficient $j$
$s$	Laplace frequency variable
$\bar{s}$	nondimensionalized $s$
$S_\theta$	airfoil pitch/plunge inertial coupling
$T$	kinetic energy
$T_1$	geometry constants for Theodorsen aerodynamics
$\bar{T}_1$	geometry constants for Theodorsen aerodynamics
$u_i(x,y)$	$i$ th in-vacuum vibration mode shape
$U$	strain energy or free-stream airspeed
$U_f$	critical freestream velocity for flutter
$U_d$	critical freestream velocity for divergence
$v$	gain subscript for velocity
$w_j$	downwash at control point $j$ due to a flap deflection
$W$	vector containing all control point downwash values created by a flap deflection angle
$x,y$	wing coordinate system or airfoil coordinate system
$z$	wing coordinate (vertical)
$\xi, \eta$	wing coordinate
$\theta$	airfoil pitch angle
$\bar{\theta}$	transformed $\theta$
$\Lambda$	wing leading-edge sweep angle
$\Lambda_k$	"kick" angle of primary bending fibers with respect to
$\mu$	airfoil density ratio
$\tilde{\rho}(x,y)$	wing mass function
$\tilde{\tilde{\rho}}(x)$	airfoil mass function
$\rho$	air density
$\sigma$	real part of $s$



$\phi$	trailing-edge flap angle
$\bar{\phi}$	transformed $\phi$
$\phi_s$	flap angle available with flap when the actuator is given the angle $\phi$ as input
$\bar{\phi}_s$	transformed $\phi_s$
$\alpha$	leading-edge flap angle
$\bar{\alpha}$	transformed $\alpha$
$\tilde{r}$	Wagner's Indicial Function
$\omega_h$	airfoil natural vibration frequency in plunge
$\omega_\theta$	airfoil natural vibration frequency in pitch
$\omega$	frequency of oscillation and imaginary part of $s$

## Abstract

In this dissertation, active control is used to suppress flutter and divergence found in forward-swept advanced-composite wings. The stability analyses are performed using linearized equations of motion in the Laplace domain. These analyses are made possible by using Padé Approximants to provide aerodynamic forces for damped wing and control surface motions. An improved method of obtaining the polynomials of the Padé Approximants is introduced. This method provides generalized aerodynamic forces in the Laplace domain that are both accurate and easy to interpret. The method's accuracy is indicated using correlations with wind tunnel experiments of forward-swept wings. The improvement involves the use of one second-order polynomial as a single common denominator for all generalized aerodynamic forces. Two cantilever forward-swept wings are analyzed as examples for active control application with leading- and/or trailing-edge flaps as control devices. One test wing is most critical in divergence, while the other wing is most critical in flutter. The flaps are actuated using simple feedback signals from acceleration, velocity, and displacement sensors. Using root locus plots of the characteristic roots from the transformed equation of motion, the stability of each combination of flap, sensor, and gain is determined. Stability is improved by an increase of 25% in the critical airspeed for the divergence-critical wing example using a leading-edge flap and elastic displacement sensing. Similarly, stability is improved by an increase of 30% in the critical airspeed for the flutter-critical wing example using a trailing-edge flap and elastic acceleration sensing. However these stability improvements are limited by the emergence of secondary aeroelastic instabilities (which become most critical) when the original primary instabilities are suppressed by active control. However practical wing designs usually exhibit these secondary instabilities at such high airspeeds that active control improvements to aeroelastic stability should be much larger when applied to actual flying hardware.

## I. INTRODUCTION

The purpose of this investigation is to apply active feedback control to the aeroelastic instabilities of divergence and flutter found in forward-swept wings. First, an improved formulation for the calculation of aerodynamic loads is developed in the Laplace domain. This aerodynamic formulation will then allow use of the linear-analysis methods of classical control theory that are posed in the Laplace domain. Using these methods, active feedback compensation is devised for the control of both divergence and flutter instabilities. These classical control design methods provide simple control laws that increase to acceptable values the critical airspeed at which flutter and divergence occur. These control laws provide the link between the aerodynamic forcing devices of flap control surfaces and the motion-measurement devices of wing-mounted sensors. Several configurations of flaps and sensors are investigated, and the classical method for linear controls allows for the independent investigation of the effects of each sensor and flap configuration. Examples will be shown of effects on flutter and divergence of both stabilizing and destabilizing control laws. In these examples, the trade-off can be demonstrated that sometimes occurs in improving one instability at the expense of another.

### Background

Wing sweep has been used as a method for delaying the effects of compressibility in high-speed wings since World War II. The magnitude of the velocity of the airflow perpendicular to the leading-edge of a wing can be used as a measure of the compressibility effects that develop on that wing. As this velocity component approaches the speed of sound, large increases in drag occur initiated by the severe adverse-pressure gradients that develop on the wing's upper surface. As a wing is swept, its leading edge is no longer perpendicular to the direction of the freestream airflow. It is rather, at an angle defined by  $\Lambda$ , the sweep angle of the wing. Therefore, only a component of the total-velocity vector is perpendicular to the wing's leading-edge. By increasing  $\Lambda$ , the total-velocity vector

can be increased, while, at the same time, holding the component perpendicular to the leading-edge at an acceptable level (Ref. 1). Therefore, the airplane can travel faster while the detrimental compressibility effects of the wing are reduced. Either positive sweep (wing tip positioned downstream from the wing root) or negative sweep (wing tip upstream of the wing root) has the same theoretical potential for reducing the losses due to compressibility of an infinite wing. However, both forward- and aft-swept wings exhibit aeroelastic instabilities. Figure 1 (Ref. 2) shows how forward-sweep results in a more severe drop (than an equivalent aft-sweep) in the airspeed at which aeroelastic divergence occurs. In aft-sweep designs, Figure 1 also suggests that flutter generally has a lower critical airspeed than divergence. It has historically been much more structurally efficient to eliminate the flutter problems of metal wings having aft-sweep than the divergence problems of metal wings having forward-sweep. Thus, aft-sweep rather than forward-sweep has been the prevalent design approach for improving compressibility characteristics of high-speed wings.

There have been some isolated uses of forward sweep in the past, and brief history of the use of forward sweep is found in Reference 3. The earliest example of modern aircraft employing an all-metal design that used forward sweep is the Junkers 287 German bomber of World War II. A later example is found in the HFB 320 business jet of the mid-1960's. Both of these aircraft used a forward sweep of less than  $15^{\circ}$  to move the wing's "carry through" structure in the aircraft's fuselage aft of the payload area. In these designs, structural packaging (rather than compressibility problems) was the prime reason for using the forward sweep. The bomber never completed its early flight tests because the Allied armies overran its testing area, and the business jet was built only in limited quantities. But no difficulties are reported for either aircraft as a result of the forward sweep. The forward sweep of both types of aircraft is not enough, however, to significantly improve high-subsonic compressibility problems of modern high-performance aircraft. When the negative sweep angles of  $30^{\circ}$  or more (needed to delay compressibility for

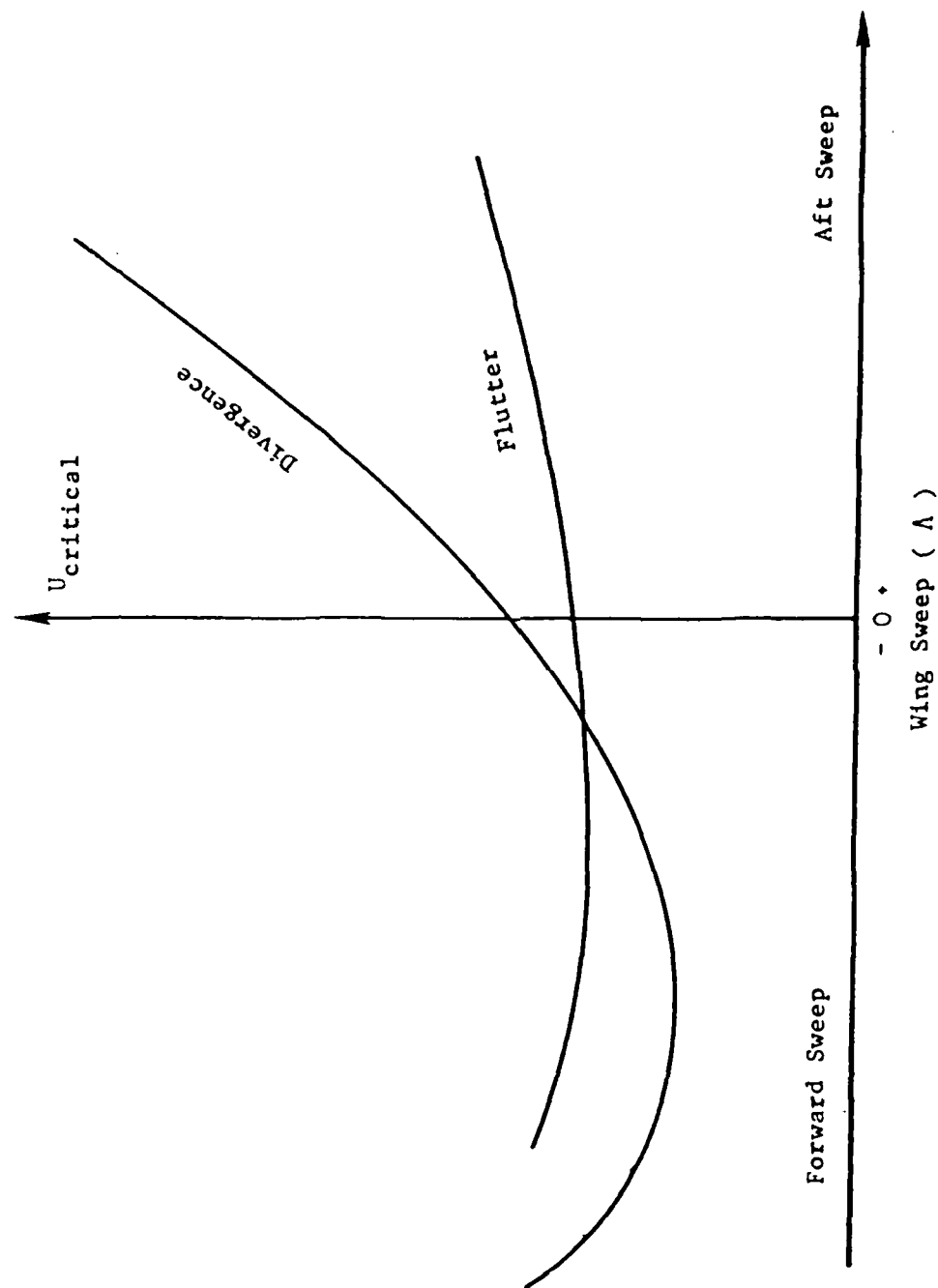


Figure 1 Wing Sweep Effects on Critical Airspeeds For Flutter and Divergence Instabilities of a Typical Aircraft

high-subsonic aircraft) are used, the wing's structural weight becomes excessive. But now that aeroelastic tailoring of composite materials in the wing's structure can solve the divergence problem, the possible aerodynamic benefits of this sweep configuration are being quantified.

#### Aeroelastic Divergence and Flutter

The primary wing stability problems examined here are the aeroelastic instabilities of flutter and divergence. Brief explanations of these are in order. These wing instabilities result from combinations of flow conditions and wing properties (both elastic and inertial) that allow wing deformations to increase quickly until there is structural failure. While rigid body motion of the wing can, in some cases, contribute to these instabilities, this investigation will examine only the more fundamental forms of flutter and divergence that contain no rigid-body motion. Flutter and divergence conditions are normally defined in terms of the freestream airspeed of the wing experiencing them. While several airspeeds may be found that have neutral aeroelastic stability, the lowest freestream airspeed at which neutral stability is maintained determines the critical airspeeds for divergence or flutter. Reference 2 gives definitions for divergence and flutter. They are summarized here as they apply to cantilever wings.

Aeroelastic divergence occurs when a lifting surface attains a freestream airspeed, where any small flow disturbance produces immediate and progressive increases in the elastic deflection of the wing, until structural failure occurs. Flutter is an oscillatory aeroelastic instability that involves the interaction of the elastic deflections of the wing, the associated changes in the wing airloads, and the mass properties of the wing. Flutter occurs when a lifting surface reaches an airspeed where any small flow disturbance causes immediate oscillatory elastic deflections that grow until structural failure occurs.

The deformation patterns of flutter and divergence explain why,

traditionally, aft-swept wings (prone to flutter instabilities) have been preferred to forward-swept wings (prone to divergence instabilities). Flutter instabilities, as previously mentioned, involve the inertial characteristics of the wing (defined by its mass distribution) in addition to the wing stiffness and aerodynamics. As airspeed increases, flow conditions develop allowing energy to be extracted from the airstream. This condition occurs because of the phase relationship between oscillatory wing motion (strongly influenced by the wing's mass distribution) and the accompanying aerodynamic loads. Classically, small changes in the mass distribution and stiffness in metal wings can be used to increase the critical airspeed for flutter until this airspeed is outside the aircraft's operating envelope. Divergence instabilities in metal wings, however, must be eliminated by adding usually prohibitive amounts of structural material. This large amount of material is necessary to make the wing's structure stiff enough to minimize the wing's deflections under all airload conditions. This stiffening for divergence requires much more structural weight than the increases in mass required for the elimination of flutter (Ref. 4). When forward-sweep, rather than aft-sweep, is employed in metal wings, the result is a heavier aircraft. Thus, high-speed aircraft have historically incorporated aft-swept wings.

#### Aeroelastically Tailored Composite Materials

With the advent of advanced filamentary composite materials, such as graphite/epoxy and boron/epoxy, new approaches for the elimination of flutter and divergence are available. The design technique of aeroelastic tailoring exploits the anisotropic material characteristics of composite materials to solve aeroelastic problems in aircraft wings. Proper orientations of the reinforcing fibers create beneficial couplings in the deformation patterns of tailored composite wings. These deformation patterns postpone the onset of divergence and flutter to safe airspeeds (Ref. 5). Typical of these patterns is a twist introduced into the wing as it bends. Using aeroelastic tailoring, Krone (Ref. 6) has shown that it is possible to design high-performance forward-swept wings using a wing structure that is as light as that of aft-swept wings. With the

opportunity now available to build forward-swept wings of reasonable weight, several aircraft manufacturers have re-examined forward-sweep. They have shown that (Ref. 7) significant improvements in wing aerodynamics and aircraft flight control appear to be possible using forward-sweep rather than aft sweep when applied to high-performance fighter aircraft. These improvements are due, in part, to the characteristic of inward spanwise flow near the wing tip in forward sweep. The use of forward sweep allows the wing-tip region to produce lift more effectively, promotes root-stall rather than tip-stall, provides higher sweep for the shock formations on the upper wing surface, and results in better cross-sectional area distributions when applying area-rule techniques to minimize wave drag (Ref. 3). The government is now funding the construction of a demonstration aircraft (the X-29) with forward-swept wings to investigate the extent of these benefits, and aeroelastic tailoring of its advanced composite wing structure provides adequate critical airspeeds for divergence and flutter. This research examines an alternate method for providing aeroelastic stability for forward-swept wings.

#### Active Feedback Control

In the investigation documented here, active feedback control is used to increase the critical airspeeds for divergence and flutter found in a forward-swept wing similar to that found on the X-29. If active controls are used to stabilize aeroelastic divergence and flutter, then the use of highly coupled composite wing construction can be avoided. Active control would then allow conventional metal construction or more traditional near-isotropic composite construction of forward-swept wings. The active control system considered here incorporates movable leading- and/or trailing-edge flaps to provide the stabilizing aerodynamic forces for the aeroelastic instabilities. The feedback loops used to direct the flap movements consist of elastic-motion sensors connected to flap actuators through linear-gain amplifiers. These loops transmit signals (corresponding to the sensed motion) to the flap actuators. The gain amplifiers adjust the signals to proper levels for maximum aeroelastic stability of the wing. A conventional and methodical approach is used to



determine the most useful feedback loops and best gain values for the improvement of aeroelastic stability.

### Approach

In this research, the classical "gain-parameter root locus" method is used for determining the required feedback and control to suppress divergence and flutter. The application of this method to aeroelastic divergence was first used by this author and reported in Reference 8. Each individual sensor and aerodynamic flap is examined in individual linked control paths. In this way, the controls engineer can examine the impact of each control law on the elastic stability of the wing. The results of these studies will suggest general conclusions about active-control applications to forward-swept wing problems. While optimal-control techniques are not used in this general investigation, they can increase the effectiveness of active-control systems on specific aircraft. Wykes has used these optimal-control techniques in designing control systems for forward-swept wing flutter caused by elastic wing-bending and rigid-body coupling (Ref. 9). Chipman has also used these control techniques to devise a system to suppress forward-swept wing aeroelastic divergence on an X-29A configuration (Ref. 10).

### History

The study of the effects that active control has on aeroelastic instabilities is not new. It began with the first applications of hydraulically boosted control surfaces in the early 1950's. With the advent of high subsonic flight, the pilot's effort to move control surfaces was too great, so boost devices were introduced to reduce his effort. Early investigations of the effects on aeroelasticity were aimed at avoiding flutter that could inadvertently be induced with these new boosted control systems (Ref. 11). The investigations progressed in the 1960's from merely avoiding the aggravation of aeroelastic instabilities to later using the control surfaces to provide stabilizing forcing functions for rigid-body as well as elastic instabilities (Ref. 12). A pilot made the first flight demonstration of feedback control for flutter using a Boeing

B-52D flight-test vehicle (Ref. 13). Here, a low-frequency wing-flutter mode was successfully stabilized by actuating trailing-edge flaps according to wing elastic motion. Subsequently, higher frequency and more complicated instabilities were examined. The latest applications of active controls in the aeroelasticity of conventional wings are adaptive-control algorithms that suppress flutter in external stores (Ref. 14 and Ref. 15). All of these applications of active control to aeroelastic instabilities were made to straight- or aft-swept wings exhibiting flutter rather than divergence aeroelastic instabilities. Active aeroelastic control was first applied in forward-swept wing configurations to solve a flutter instability involving rigid-body pitch and elastic wing-bending (Ref. 9 and Ref. 10). Early flight demonstration designs of forward-swept wings showed a strong sensitivity to this rigid-body pitch and elastic-wing bending flutter. This effort is focused on active control applications to aeroelastic flutter and divergence without rigid-body motion for forward-swept wings. This research is done by using a cantilever boundary condition for the wing structure. Thus, rigid-body motion (such as rigid-body pitch) is not allowed in the analyses, and classical wing divergence can be observed in the wing's response to disturbances.

#### Overview

The presentation of this research is organized in the following manner. The study of feedback control for forward-swept wings is much easier if the development of their equations of motion in the Laplace domain results in a form compatible with standard active control techniques. Thus, the development of the equations of motion, and in particular the development of suitable aerodynamic forces in polynomial form, is presented first to show the wing equations in proper form for the stability analyses. Using these equations, the wing responses are then examined for disturbances where a series of feedback sensor, gain, and control-surface configurations are included in the stability equations. Successful feedback-control configurations for forward-swept wing flutter and divergence are found and then examined in more detail. Finally, some conclusions are drawn from the results of the case examples. In an

appendix that follows the main text, some of the development details and stability results are included from preliminary calculations using a two-dimensional airfoil. Also included as appendices are details of the doublet-lattice method and some wind tunnel correlations made using the Padé approximations to doublet-lattice aerodynamics. The specific items contained in each chapter are organized in the following manner.

The development of the equations of motion in the Laplace domain is described in Chapter II. Details are included of the transformed mass and stiffness representations, along with the coordinate system used in the analytic model of the wing. Using insight developed from two-dimensional wing examples found in Reference 16 (and outlined in Appendix A), a new formulation for the wing aerodynamic forces is presented in Chapter II. This formulation presents a new method for employing Padé Approximant polynomials in calculating wing forces due to damped motion. These polynomials are also used in calculating the stabilizing forces created by movements of the leading- and trailing-edge control surfaces. The feedback control laws and the sensor measurements they require are also described in Chapter II. The sensor locations and the several combinations of measurements they provide offer 96 possible simple feedback control combinations for stabilizing flutter and divergence. These combinations are then applied to specific wing examples in Chapter III.

In order to demonstrate the usefulness of the several feedback control combinations described in Chapter II, two example cases for forward-swept wings are examined in Chapter III. These example cases use a cantilever forward-swept wing geometry similar to that used to perform the early forward-swept wing fighter studies (Ref. 7). These early forward-swept wing geometries were developed to perform missions similar to those of the light-weight fighter of Reference 17. The active-controls applications found in this investigation represent active-control applications for modern fighter-category aircraft. These forward-swept wing examples have either flutter or divergence as their most critical aeroelastic instabilities. The evaluation and selection of useful feedback control

laws for these examples are presented graphically using plots on the complex plane. These are plots of the loci of the characteristic roots calculated from the wing equations of motion. These loci are defined by the movement of the roots that results when a selected parameter (amplifier gain or freestream airspeed) is varied. With these plots the stability of the wing can be inferred and most advantageous gain values selected for improved stability.

In Chapter IV some conclusions are drawn from the case studies of Chapter III. Not only are specific wing stability improvements discussed, but also some changes in wing design philosophy are suggested. When active control methods are used for stability augmentation, some of the restrictions can be removed on the wing structural designer. The specific wing stability improvements shown here illustrate possible approaches for wing stability augmentation. The actual amount of stability improvement greatly depends on the specific wing designs examined. The considerable improvements demonstrated here suggest however that active control can contribute considerably to wing aeroelastic stability.

## CHAPTER II - WING ANALYSIS

The equations of motion to be used for the wing aeroelastic stability calculations are described in this chapter. The formulation used for the aerodynamic forces is discussed in some detail since it differs from methods used in the past. Using the formulation of these aerodynamic forces, the stability equations for the unaugmented wing are then calculated. Forces due to movement of the wing's leading- and trailing-edge control surfaces are also calculated. These control-surface forces are then used to stabilize the wing by requiring the control surfaces to move according to control laws that use as inputs measured wing motion. These control laws can be formulated to prescribe the control-surface motion as functions of the wing degrees-of-freedom. This linkage between control-surface forces and the degrees-of-freedom provide the means to incorporate the stabilizing control-surface forces in the unaugmented wing equations of motion. The resulting augmented wing equations of motion can then be used for examination of the best gain values in the control laws for improved wing stability.

The equations of motion used here for the aeroelastic-stability calculations are developed in a similar way to the equations used for other stability calculations, such as buckling. That is, a wing at equilibrium in the flow is assumed. The wing is then subjected to small disturbances, and the stability of this equilibrium position is determined by the changing wing position in relation to this equilibrium with the passage of time. By observing the wing response about the immediate vicinity of the equilibrium position, the stability of the wing can be determined using linearized equations for the structure and resulting aerodynamic forces. These equations are developed in the following sections.

### Equations of Motion

In developing the wing equations of motion, the equilibrium wing position can be any steady-state lift condition for the aircraft. The

position most commonly used, and the one used in this investigation, is the zero-lift condition. It can be shown that the linearized equations about this equilibrium condition will properly predict the critical velocity for aeroelastic instabilities (Ref. 2). Accordingly, the wing will be treated aerodynamically as a flat plate without twist or camber. The wing is at zero angle-of-attack before the disturbance is applied, and the wing's deformation response relative to the zero condition will determine stability. Deformations that eventually die away to zero and remain zero with the passage of time indicate a stable configuration. If the deformations eventually grow without bound as time passes, an unstable configuration is indicated. And the critical-flow conditions (where the deformations neither grow nor subside with time) indicate neutral-stability conditions.

The wing examined here is a cantilever forward-swept wing (Figure 2) that has its root rib rigidly attached to an immovable foundation. This cantilever attachment eliminates any rigid-body aircraft motion from the wing's stability analysis. The wing, in its undeformed state, has a neutral plane (or plane of symmetry) in the x,y plane, with the x axis at the centerline. The y axis is perpendicular to the x axis. The wing deformation is calculated from the movement of this neutral plane and represented by the function h, defined in terms of the spatial x, y locations and time t. The transverse displacement h is approximated by a finite sum:

$$h(x,y,t) = \sum_{i=1}^N u_i(x,y)a_i(t) \quad (1)$$

The displacement functions  $u_i(x,y)$  are the first N natural vibration mode shapes (out-of-plane) of the wing, and the time functions  $a_i(t)$  are the modal amplitudes that prescribe the contributions in deformations of each mode with time. The equations of motion are developed from Lagrange's equation.

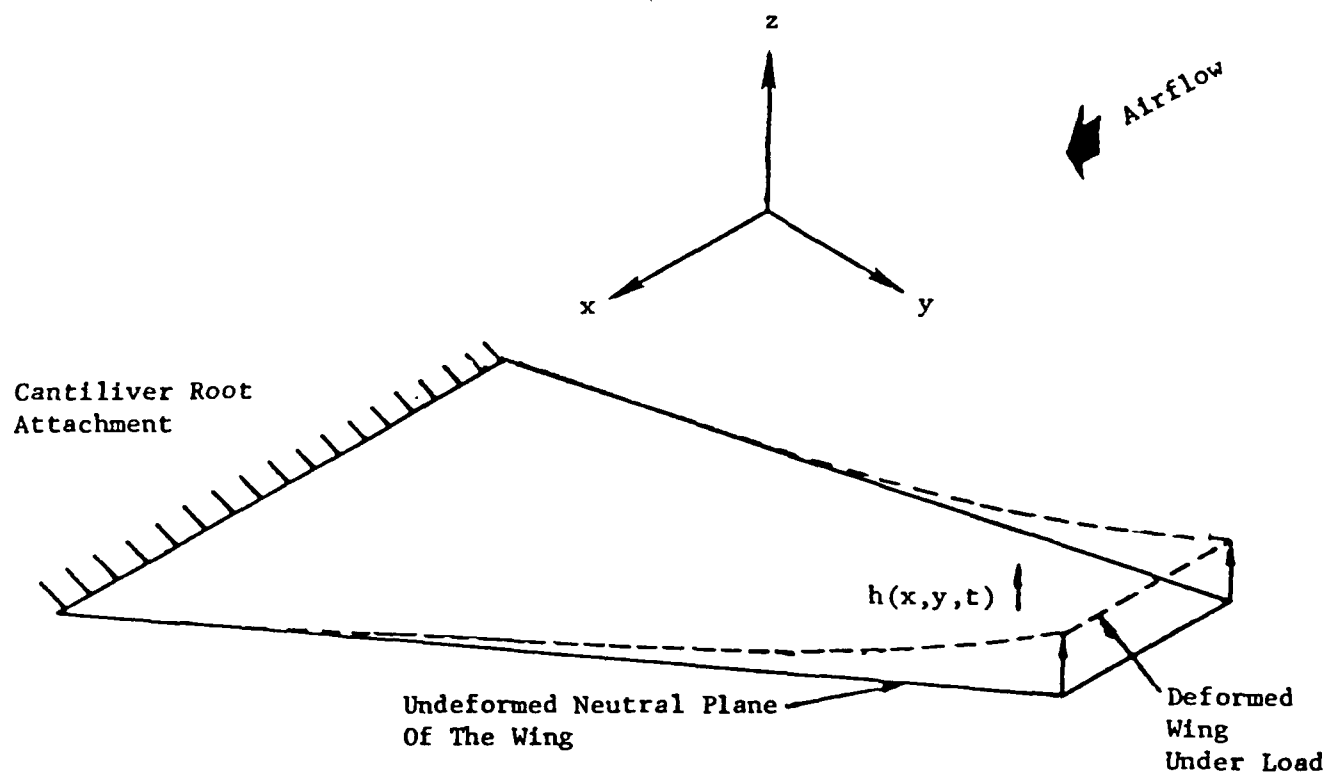


Figure 2 Wing Geometry

$$\frac{d}{dt} \left( \frac{\partial T}{\partial \dot{a}_i} \right) + \frac{\partial U}{\partial a_i} = Q_i \text{ total} \quad (2)$$

In this equation,  $T$  is the wing's kinetic energy,  $U$  is the elastic strain energy, and  $Q_i$  is the total generalized force.

The kinetic energy can be obtained by summing all of the kinetic energy in each element of the wing's mass using the vertical velocity  $h$ .

$$\begin{aligned} T &= 1/2 \iint_{\text{wing area}} [\dot{h}(x,y,t)]^2 \tilde{\rho}(x,y) dx dy \\ &= 1/2 \iint_{\text{wing area}} \left[ \sum_{i=1}^N u_i(x,y) \dot{a}_i(t) \right] \left[ \sum_{j=1}^N u_j(x,y) \dot{a}_j(t) \right] \tilde{\rho}(x,y) dx dy \quad (3) \end{aligned}$$

The wing's mass distribution as a function of  $x$  and  $y$  is the function  $\tilde{\rho}$ . By interchanging the orders of integration and summation, equation 3 can be simplified.

$$T = 1/2 \sum_{i=1}^N \sum_{j=1}^N m_{ij} \dot{a}_i(t) \dot{a}_j(t) \quad (4)$$

The constants  $m_{ij}$  represent the inertial coupling terms between the generalized coordinates  $u_i$  and  $u_j$ .

$$m_{ij} = \iint_{\text{wing area}} [u_i(x,y) u_j(x,y) \tilde{\rho}(x,y)] dx dy \quad (5)$$



The matrix of elements  $m_{ij}$  is symmetrical, allowing  $i$  and  $j$  to be interchanged.

The potential energy term,  $U$ , is developed from the internal elastic forces created in the wing, resulting from the deformation of its elastic structure, as described in Reference 2.

$$U = 1/2 \iint_{\text{wing area}} h(x,y,t) \iint_{\text{wing area}} [k(x,y;\xi,\eta)] [h(\xi,\eta,t)] d\xi d\eta dx dy \quad (6)$$

The stiffness function,  $k(x,y;\xi,\eta)$ , defines the force required at  $x,y$  to maintain a unit displacement in the wing at location  $\xi,\eta$  of the wing. By using the form of  $h$  in equation 1, the area integration over the wing can be included as constants in the energy summation.

$$U = 1/2 \sum_{i=1}^N \sum_{j=1}^N k_{ij} a_i(t) a_j(t) \quad (7)$$

The area integrations define the constants  $k_{ij}$  which relate the structural stiffness influences between the generalized coordinates  $u_i$  and  $u_j$ :

$$k_{ij} = \iint_{\text{wing area}} u_i(x,y) \iint_{\text{wing area}} [k(x,y;\xi,\eta)] u_j(\xi,\eta) d\xi d\eta dx dy \quad (8)$$

The generalized forces,  $Q_i$ , are calculated using the natural-mode generalized coordinates of equation 1. They include both the aerodynamic forces  $F_{\text{aero}}$  (resulting from the wing shape) and the force that initially disturbs the wing from its equilibrium,  $F_{\text{dist}}$ :

$$\begin{aligned}
Q_{i \text{ total}} &= \iint [F_{\text{aero}}(x,y,t) + F_{\text{dist}}(x,y,t)] u_i(x,y) dx dy \\
&= Q_{i \text{ aero}} + Q_{i \text{ dist}}
\end{aligned} \tag{9}$$

When all of the energy terms are combined into equation 2, the resulting set of N equations of motion is obtained in terms of the vibration-mode generalized coordinates:

$$\sum_{j=1}^N m_{ij} \ddot{a}_j(t) + \sum_{j=1}^N k_{ij} a_j(t) = Q_{i \text{ total}} \quad i = 1 \dots N \tag{10}$$

The number of modes used (and therefore the value of N) in the equations of motion is determined by the least number of coordinates required to accurately predict  $U_d$  and  $U_f$ . For the wing studies, the first four vacuum vibration modes are sufficient. The equations can be written in more compact form, using matrix notation.

$$[M] \{a(t)\} + [K] \{a(t)\} = \{Q\} \tag{11}$$

These equations can now be solved to determine if any of the resulting coordinates  $a_i(t)$  will increase in magnitude with time and define an aeroelastic instability.

#### Structural Representation

The calculations of the normal-mode shapes  $u_i$  and the area

integrations of the influence functions, such as  $k(x,y; \xi, \eta)$ , for the equations of motion are made using a Rayleigh-Ritz formulation, (Ref. 2) similar to that used for plates. This Rayleigh-Ritz approach lends itself to continuous polynomial descriptions of the stiffness and inertia for the wing structure, and polynomials for thickness distributions are the easy way to represent multi-layered composite structure. The Rayleigh-Ritz formulation is, therefore, especially useful for the kind of wing used in this research. The wing structure is made of advanced filamentary composite material aeroelastically tailored to provide selected flutter and divergence airspeeds. The tailoring of the composite material results in spanwise and chordwise variations in the thickness of the layers of composite material. These variations are so prescribed to get a wing structure that deforms in desired patterns under specific load conditions. These material distributions in the wing-box covers can be represented best as polynomial functions of  $x$  and  $y$ . This plate formulation, employing these polynomials, is highlighted below.

A description of the wing structure is useful in understanding the Rayleigh-Ritz plate analysis. To help with this description, a planform view of the cantilever wing is given in Figure 3. Both the aerodynamic planform and primary load-carrying structure (structural box) of the wing are depicted. The cantilever condition for the structural box is shown at its root rib. The wing planform has a leading-edge sweep of  $-31.1^\circ$ . The semi-span is 265 inches, with the aircraft's centerline root chord of 136 inches and a tip chord (parallel to the freestream direction) of 58 inches. The wing's thickness-to-chord ratio is 5%.

The structural box is that portion of the wing's volume that contains all of the primary structure for the wing. So those portions outside this box are normally considered as secondary structure. The deformations in the secondary structure are calculated by extrapolating (into the planform

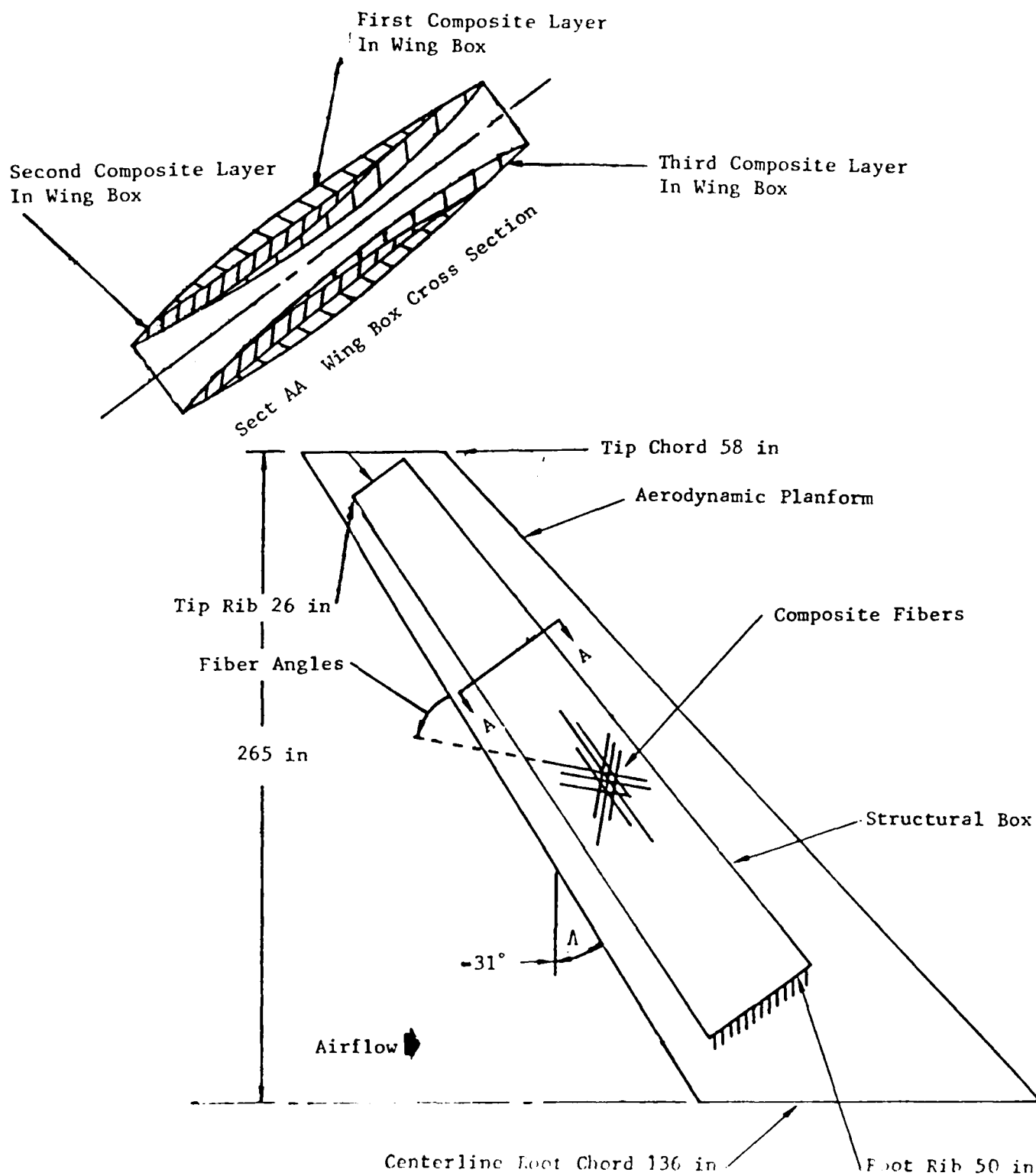


Figure 5 Geometry for Cantilever Wing Planform And Structural Box

region of the secondary structure) the deflections and rotations occurring at the perimeter of the primary structure.

The structural box is modeled analytically as a layered plate and shown in cross-section with the section-cut of Figure 3. Each layer is described using a thickness polynomial in the  $x$  and  $y$  over the planform. Each layer contains a thickness distribution of advanced composite material corresponding to a particular fiber direction. The wing plane of symmetry is defined at 0 on the  $z$  axis (the mid-plane of the plate), so all of the structure in these layers above the plane has a mirror image below this plane. There are three material layers on each side of this neutral plane, and these three layers above and below the plane collectively represent respectively the wing-box upper and lower covers.

The composite material used in each layer is a unidirectional graphite fiber embedded in an epoxy matrix. The unidirectional properties used for this investigation are typical of graphite/epoxy systems used in aircraft and represent current design values. The material density is  $.054 \text{ lbs/in}^3$ . The Young's Modulus for the fiber direction is  $21 \times 10^6 \text{ lbs/in}^2$ ; and for all the directions transverse to the fibers the modulus is  $1.2 \times 10^6 \text{ lbs/in}^2$ . Poisson's Ratio is  $.21$  with a shear modulus of  $.65 \times 10^6 \text{ lbs/in}^2$ . Since there are three layers for each side of the wing box, there will be, at most, three different fiber directions for the wing box. These directions are prescribed by the angle the fibers make with the leading-edge sweep line of the wing box as shown in Figure 3. The thickness distribution of each layer with a given fiber angle is allowed to vary both spanwise and chordwise according to sixth-order polynomials. These thickness distributions are required to fit inside the external geometry of the wing box. In the actual wing box, the structural-box covers are stabilized by a layer of substructure such as spars, ribs, or full-depth honeycomb material. In this plate representation of the wing box, the substructure is another layer of material filling the volume between the upper and lower covers. It has infinite shear strength and a density of aluminum honeycomb. This substructure layer is representative of a high-modulus full-depth honeycomb core. The wing box is enclosed by a leading-edge

spar, trailing-edge spar, root rib, and tip rib. These structural members are included in both the elastic and inertial calculations for the plate analysis. The geometry of the plate thus comprises seven layers of material arrayed symmetrically about the  $x,y$  plane. The total plate thickness is prescribed by a third-order polynomial in  $x$  and  $y$ . In summary, this plate volume has the three composite layers clustered at the upper and lower surfaces. The volume in between the upper and lower clusters is treated as the seventh layer of substructure.

The above plate geometry (resulting from modeling, analytically, thin fighter-wing structural boxes as plates) lends itself to thin-plate theory. Therefore, the neutral surface is assumed coincident with  $x, y$  plane before loads are applied to the wing. After the loads are applied, no in-plane stress or "membrane" stretching of the plate is allowed at the neutral surface. The plate analysis uses further simplifying assumptions to make the calculations easier. The first assumption requires that lines in the wing box normal to the neutral plane remain normal to that plane in the deformed state of the wing box when loaded. This assumption is also known as the Kirchhoff hypothesis and implies a second assumption, that of small displacements throughout the structural box.

The plate analysis used here calculates the influence-function integration of equation 8 using a Rayleigh-Ritz approach for a thin square plate of unit length on each side. Thus, the trapezoidal wing box planform must be converted to a unit square planform. A set of mapping functions converts the general trapezoidal geometry of the wing box to the unit square. Then a sixteen-term Taylor series can be used in the integration of equation 8 to approximate the elastic relationships of the square plate. The assumed displacement functions used for the Rayleigh-Ritz calculations are made up of sixth-order Legendre polynomials prescribed in both the spanwise and chordwise directions of the unit square. Using these Legendre polynomials to describe the mode shapes, the mass contributions of the equations of motion can be calculated from equation 5. All that remains then is the development of the generalized forces. The development of suitable expressions of  $Q_1$  are discussed in detail in a following section.

To determine the aeroelastic stability of the cantilever wing, the generalized equations of motion in matrix equation 11 are used to calculate the wing's motion after the occurrence of a small disturbance. An unstable condition exists when the generalized coordinates  $a_i$  of equation 11 get larger as time lapses. The way the functions  $a_i$  change with time is calculated here using a Laplace transformation from the time domain. For items transformed with the Laplace transformation, the notation is the bar over the variable.

$$\begin{aligned}
 \mathcal{L}[h(x,y,t)] &= \mathcal{L}\left[\sum_{i=1}^N u_i(x,y)a_i(t)\right] \\
 &= \int_0^{\infty} e^{-st} \left[\sum_{i=1}^N u_i(x,y)a_i(t)\right] dt \\
 &= \sum_{i=1}^N u_i(x,y)\bar{a}_i(s) \\
 &= \bar{h}(x,y,s)
 \end{aligned} \tag{12}$$

The motion of any x,y locations of the wing in time can now be calculated using the Laplace variable s. Transforming matrix equation 11 into the Laplace domain produces algebraic equations in s rather than differential equations in time.

$$s^2[M]\{\bar{a}\} + [K]\{\bar{a}\} = \{\bar{Q}\}_{\text{total}} \tag{13}$$

When the generalized forces are transformed into the Laplace domain, the resulting algebraic equations of motion can be used in a stability analysis. Positive, neutral, or negative aeroelastic stability of the wing is then determined if the inverse transform of  $\bar{a}_i(s)$  becomes smaller, remains constant, or grows with time respectively. The calculation of these transformed aerodynamic forces requires a method for predicting the loads due to damped motion rather than just oscillatory motion. This requirement has historically offered considerable difficulty, but it is now

possible to meet this requirement using the following development of the generalized forces in the Laplace domain.

### Aerodynamic Forces

In this section the method for calculating the aerodynamic forces of the wing is described. The formulation employed here uses Padé Approximants as polynomials to represent the wing forces. The Padé Approximants provide a means of calculating in the Laplace domain the aerodynamic forces from damped wing motion. A desirable feature of these Padé Approximants is that they can be calculated using presently available methods for pure sinusoidal motion such as the doublet-lattice method of Reference 18. The doublet-lattice method is desirable because it can be used for general lifting surface geometries and allows the representation of control surfaces on these lifting surfaces. The way the Padé Approximants are calculated and used have been modified here to improve their utility in wing aeroelastic stability analyses. This improvement is outlined in the following descriptions.

The use of Padé Approximants here results from some preliminary evaluations of approximating functions such as those used by Vepa (Ref. 19) and direct calculations such as those suggested by Edwards (Ref. 20). The evaluations were made using a simple two dimensional airfoil and are summarized in Appendix A. The method used here is similar to those used by active-control analysts to obtain transfer functions in the Laplace domain for unknown "black box" devices. That is, known functions are input into the "black box" and the resulting responses from the "black box" are recorded. Using these measured responses a transfer function can be calculated that approximates the "black box." For aeroelastic calculations, the "black box" is the sinusoidal aerodynamic prediction methods, such as doublet-lattice. These provide the necessary force responses to the known input functions which are the sinusoidal wing motions. The Padé Approximants are the transfer functions of  $s$  that provide wing forces due to damped wing motion.

The Padé Approximants are ratios of polynomials in the Laplace variable  $s$  that have constant coefficients. They are called Padé because



of their similarity to the Padé method of approximating measured data with series (Ref. 21). Schwanz has summarized and documented several forms of approximating functions in Reference 22. The functions used here are chosen based on their accuracy of aerodynamic force approximations and their compatibility with the wing equations of motion that are written in the Laplace domain. The form is shown in equation 14 and is similar to that suggested by Vepa.

$$\bar{A}_{jl} = \left[ \sum_{f=0}^n (P_{fjl}) s^f \right] / \left[ 1. + \sum_{f=1}^d (Q_{fjl}) s^f \right] \quad (14)$$

The force corresponding to degree-of-freedom  $j$  and created by degree-of-freedom  $l$  is represented by a polynomial of order  $n$  divided by a polynomial of order  $d$ . These polynomials of the Laplace variable  $s$  have the constant coefficients  $P_{fjl}$  and  $Q_{fjl}$ . These coefficients are defined by a two-stage fitting process using the least-squares method. The orders  $n$  of the numerator and  $d$  of the denominator are 3 and 2 respectively. These orders were chosen as a result of preliminary evaluations made of Padé Approximants using a two-dimensional airfoil. These airfoil studies are highlighted in Appendix A.

In order to determine the polynomial coefficients in equation 14, wing aerodynamic forces are first calculated for pure sinusoidal wing motion. These sinusoidal forces are calculated for several frequencies of wing motion. Twenty values of frequency are used here to provide a frequency range wide enough for calculating Padé Approximants that are capable of predicting both flutter and divergence. The coefficients of the polynomials in equation 14 are then adjusted to provide the best approximation in the least-squares sense of the forces at which the frequencies were calculated. Each of these frequencies of wing motion is specified in the non-dimensional form of equation 15 and is referred to as a reduced frequency  $k$ .

$$k = \omega b/U \quad (15)$$

In defining this reduced frequency,  $\omega$  is the actual sinusoidal frequency,  $U$  is the freestream airspeed of the wing, and  $b$  is a wing reference length. The value of  $b$  is usually half the mean aerodynamic chord or half the wing root chord. The root semi-chord is used here. The forces calculated as a function of frequency  $k$  can be related to equivalent forces in the Laplace domain as a function of  $s$  by observing the constituents of  $s$ . The value of  $s$  can define a root from the equations of motion in the Laplace domain.

$$s = \sigma + i\omega \quad (16)$$

The real part of  $s$ , noted here as  $\sigma$ , defines the sense of damping, and the imaginary part, noted here as  $\omega$ , is the frequency. By non-dimensionalizing  $s$  in the same way as was done with  $\omega$  in the reduced frequency of equation 15, the relationship between  $k$  and  $s$  can be seen.

$$\begin{aligned} \bar{s} &= sb/U \\ &= \sigma b/U + ik \end{aligned} \quad (17)$$

Note that in the special case of zero damping  $\bar{s}$  is defined only by  $k$  as its imaginary part. Thus, aerodynamic forces calculated for the twenty reduced frequencies using the doublet-lattice method are valid for pure undamped sinusoidal motion. Therefore, they can be used for the Padé fitting process by providing twenty sets of forces for non-dimensional and purely imaginary values of  $s$ . The polynomials of  $s$  are then calculated to approximate these twenty sets of forces using a least-squares fitting algorithm.

The detailed steps of the aerodynamic calculations used here begin with the sinusoidal airloads. The source of the forces for subsonic compressible airspeeds used here is the doublet-lattice method of Reference 18. This is a method that uses arrays of doublet singularities in

potential flow and is discussed in more detail in Appendix B. These singularities create the same downwash at selected locations in the potential flow field that would correspond to downwash caused by the oscillating wing. As described in Appendix B, this method provides a way of calculating the unsteady aerodynamic forces by generating linear aerodynamic influence coefficients  $\tilde{a}_{ij}$ . The wing planform is divided into small regions or panels and the  $\tilde{a}_{ij}$  constants relate the effect each panel region has on all the other panels. The coefficients define the force contribution on the  $i$ th panel due to wing motion at the control point of the  $j$ th panel. Therefore, forces on the wing are represented by concentrations of forces in each panel using the superposition of the influence of all panels, as represented by matrix equation 18.

$$\begin{Bmatrix} F_1(t) \\ F_2(t) \\ \vdots \\ F_m(t) \end{Bmatrix} = \begin{bmatrix} a_{11} & a_{12} & \cdots & a_{1m} \\ a_{21} & a_{22} & \cdots & a_{2m} \\ \vdots & \vdots & \ddots & \vdots \\ a_{m1} & \cdots & \cdots & a_{mm} \end{bmatrix} \begin{Bmatrix} h_1(t) \\ h_2(t) \\ \vdots \\ h_m(t) \end{Bmatrix} \quad (18)$$

Therefore, as the panels are arrayed over the entire wing planform, the overall forces on the wing are represented. The doublet-lattice idealization of the forward-swept cantilevered wing for this effort is shown in Figure 4. These 96 panels provide the array of forces created on itself as the wing performs sinusoidal motion in the presence of streamwise airflow. These sinusoidal forces are then put in generalized form to be compatible with the wing equations of motion. This is done using the wing natural vibration modes.

Recall that the coordinates for the cantilever wing are the wing's natural-vibration mode shapes. Therefore, a coordinate transformation is needed to make the doublet-lattice aerodynamic-influence coefficients compatible with the wing's modal-coordinate system. This transformation uses a matrix of constants  $E_{lj}$  prescribing the values of each mode shape  $l$  at the  $x, y$  coordinates of control point  $j$ .

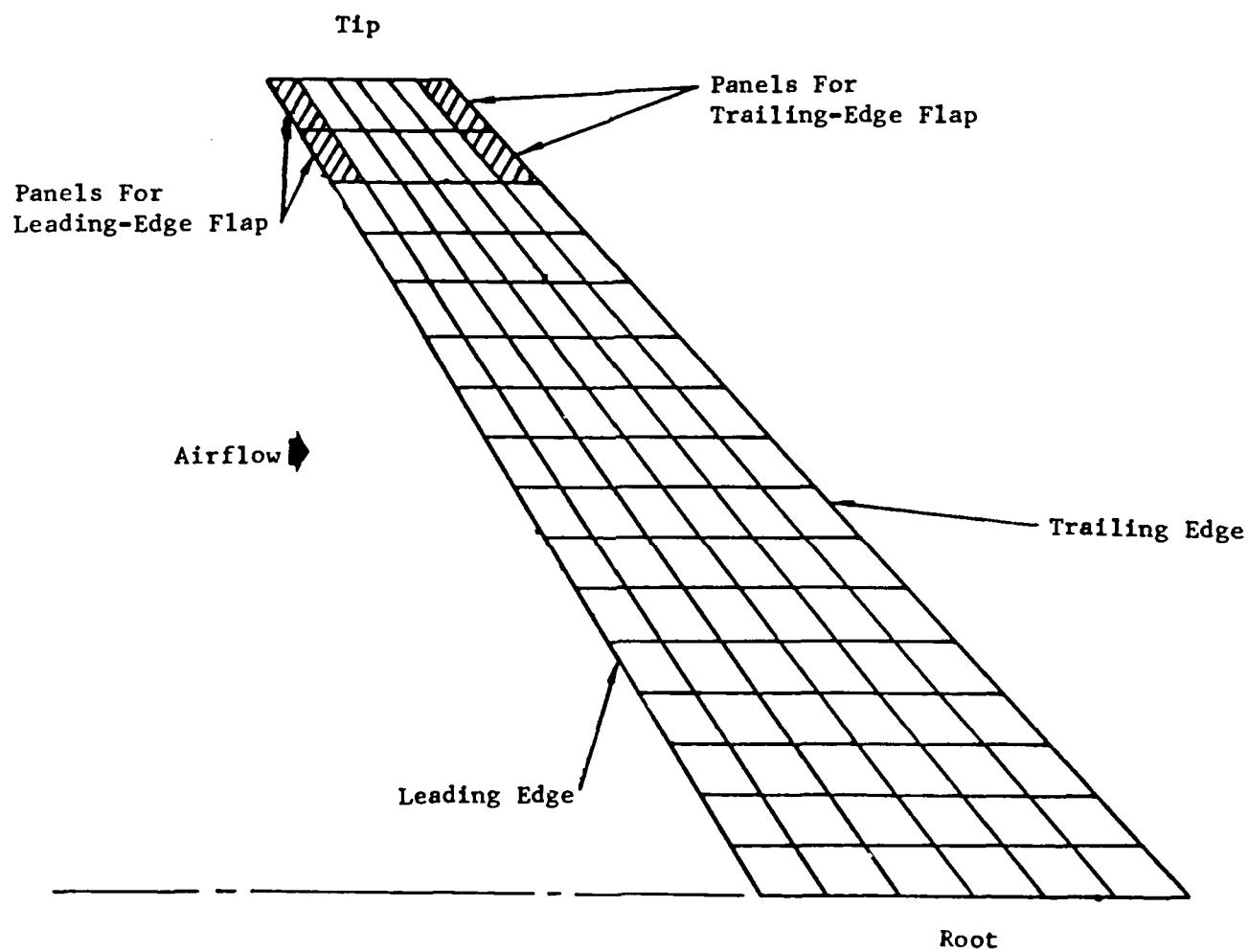


Figure 4 Panel Geometry For The Wing  
Doublet-Lattice Aerodynamics

$$E_{1j} = u_1(x_j, y_j) \quad (19)$$

A similar transformation is needed to generalize the forces occurring at the panels' force points. This makes the forces compatible with the modal degrees-of-freedom. This generalization is made using a modal transformation matrix  $E$  evaluated at the quarter chord locations of the panels. For simple harmonic motion and  $N$  modes, the resulting generalized forces are now functions of the coordinates  $a_1(t)$ .

$$\left\{ Q(t) \right\} = \underset{1/4 \text{ chord}}{[E]^t} \underset{3/4 \text{ chord}}{[\tilde{A}][E]} \left\{ a(t) \right\} \quad (20)$$

Remember that the  $a_1(t)$  terms are the time-dependent coordinates for the modal degrees-of-freedom. They must describe simple harmonic motion so that the doublet-lattice influence coefficients are applicable. Equation 20 is simplified to represent the aerodynamic forces for the equations of motion.

$$\left\{ Q(t) \right\} = [A] \left\{ a(t) \right\} \quad (21)$$

The complex constants for  $A$  are calculated for a chosen value of reduced frequency  $k$  and Mach number using the doublet-lattice computer program.

The doublet-lattice method just described can be applied to lifting surfaces of general shape. This suggests that it should be applicable to the forward-swept wing geometry used here, and its capability to represent forward sweep is confirmed by wind-tunnel correlations in Appendix C. The previous developments can provide only sinusoidal forces for a chosen  $k$  using the doublet-lattice method. The Padé Approximant method is used to extend the results to provide damped-motion wing aerodynamic forces.

The calculations of the polynomial coefficients for the Padé Approximants are done after the sinusoidal forces are generalized into the

modal degrees-of-freedom. The generalized forces are smooth functions over the wing planform and provide proper descriptions of the wing's motion with only a small number of degrees-of-freedom. By using this reduced number of degrees-of-freedom, the least-squares fitting process is kept to a minimum. The first step in the two-step fitting process is the calculation of a unique polynomial (equation 14) that represents the variation with  $s$  (as defined by  $k$ ) of each generalized force coefficient. This variation spans the range of  $k$  represented in the 20 values of  $k$  from the doublet-lattice calculations. Since the stability analyses here must find divergence (a zero frequency instability) as well as flutter (a non-zero frequency instability) the range of  $k$  needed for the Padé fitting begins at zero and increases until it encompasses the expected flutter frequency. At this point there are  $N \times N$  denominator polynomials in the Padé Approximants. This large number of denominators greatly complicates the stability analyses in the Laplace domain and is not necessary.

As a second step in creating the Padé Approximants, the coefficients of the denominator polynomials from the first least-squares fit are averaged together to produce coefficients for a single polynomial. This polynomial then serves as the common denominator for a new calculation of the Padé Approximants. Each influence coefficient of the generalized aerodynamic forces is approximated again for a second time by functions of the form of equation 14. This second time the least-squares fitting of the 20 sets of aerodynamic forces is made with the denominator of each Padé Approximant held constant to the common denominator. The results provide generalized aerodynamic influence coefficients with unique numerators but with a common denominator polynomial. The resulting matrix of polynomials can be organized into an  $\bar{A}$  matrix as shown in equation 22 for ease of manipulation.

$$[\bar{A}] = \frac{1.}{\tilde{Q}_2 s^2 + \tilde{Q}_1 s + 1.} \begin{bmatrix} (P_{311}s^3 \dots P_{011}) \dots (P_{31N}s^3 \dots P_{01N}) \\ \vdots \\ (P_{3N1}s^3 \dots P_{0N1}) \dots (P_{3NN}s^3 \dots P_{0NN}) \end{bmatrix} \quad (22)$$

$$= (1./(\tilde{Q}_2 s^2 + \tilde{Q}_1 s + 1.)) \left[ |P_3|s^3 + |P_2|s^2 + \dots + |P_0| \right]$$

The generalized forces are now available for damped motion as described by the transformed coordinates  $a_1$

$$\{\bar{Q}\} = [\bar{A}] \{\bar{a}\} \quad (23)$$

The quality of Padé Approximant representations of the generalized forces can be measured by comparing generalized force terms calculated by the approximations and those calculated directly using the doublet-lattice method. In Table 1, this comparison is made for two generalized force terms,  $\bar{A}_{11}$  and  $\bar{A}_{22}$ , at a series of reduced frequencies. This level of agreement is acceptable and found in all the generalized force terms. Not only do the Padé Approximants agree well with other prediction methods for sinusoidal motion, the wing equations of motion using the Padé Approximants predict stability characteristics that agree well with those found by experiments. In Appendix C, correlations are made with wind-tunnel model experiments. Not only do these equations properly predict aeroelastic flutter and divergence, but these equations also provide insight into the explosiveness of a particular instability. These model correlations suggest that the methods used here can be used with some confidence. Before improvements in stability using active feedback control can be investigated however, control surface effects must be added to provide the stabilizing forces.

#### Control Surface Aerodynamic Forces

In the previous section, the formulations for the aerodynamic forces caused by general motions of the wing are described using Padé Approximants. Added to these forces are those created by the deployment of leading- and/or trailing-edge flaps. These control-surface forces will be used to stabilize flutter and divergence, and the calculation of these control-surface forces is described next. These control-surface aerodynamic forces are calculated in similar ways to those forces resulting from general lifting-surface motion. The exact relationship between the flap deflections and the lifting-surface motions will be defined in a later section by the control laws of the feedback circuits.

Table 1 Generalized Aerodynamic Influence Coefficient Comparisons For The Wing

k	$\bar{A}_{11}$				$\bar{A}_{22}$			
	Doublet-Lattice real	Doublet-Lattice imag.	Pade' Fit real	Pade' Fit imag.	Doublet-Lattice real	Doublet-Lattice imag.	Pade' Fit real	Pade' Fit imag.
.00001	.0178	0	.0174	0	.007	0	.007	0
.1	.0166	-.0107	.0174	-.009	.00749	-.00434	.00731	-.00479
.3	.0150	-.0272	.0176	-.0267	.0101	-.0142	.00924	-.144
.5	.0170	-.0432	.0182	-.0436	.0141	-.0246	.0132	-.0245
.7	.0207	-.0592	.0198	-.0597	.0195	-.0356	.0193	-.0349
1.	.0303	-.0898	.0257	-.0826	.0309	-.0528	.0326	-.0528
2.	.0779	-.186	.0790	-.177	.0939	-.128	.0941	-.149
3.	.137	-.305	.136	-.320	.161	-.246	.136	-.286

(Based on Modal coordinates from Wing Case 1)



Control surfaces for the forward-swept cantilever-wing configurations are located on the trailing- and leading-edges of the wing tip as shown in Figure 5. The deflection angles of  $\phi$  and  $\psi$  for the trailing- and leading-edge flaps respectively measure positively about the hinge axis for the aircraft's starboard side wing as shown in the section cut of Figure 5. The control-surface influences on the wing's airloads are calculated using the same set of aerodynamic influence coefficients from equation 18 as were used for the wing motion. The control-surface motions prescribe downwash velocity requirements similar to those defined by the general motion of the wing. Forces on the wing due to control-surface deflections can then be calculated by combining the downwash due to their deflection and the wing influence coefficients  $\tilde{a}_{ij}$ . This wing downwash due to the control surfaces is calculated as follows. At a control point  $j$  in the planform, the downwash velocity,  $w_j$ , is calculated from the flow that is deflected by the flap when it is rotated. This vertical velocity component of the flow is created by the combination of deflection of the freestream flow with the flap and the rotation of the control point about the flap's hinge line.

$$\begin{aligned} w_j &= U \tan \phi + \dot{\phi} \tilde{d}_j \\ &\approx U \phi + \dot{\phi} \tilde{d}_j \end{aligned} \quad (24)$$

A similar expression is used for the leading-edge flap, and the term  $\tilde{d}_j$  is the radius from the flap's hinge line to the control point  $j$ . Since the aerodynamic influence coefficients from the doublet-lattice computer program are defined only for simple harmonic motion, the expression is written in terms of the reduced frequency of sinusoidal flap motion.

$$\begin{aligned} w_j &= U \phi + i U \dot{\phi} \tilde{d}_j k / b \\ &= U (1. + i \tilde{d}_j k / b) \phi \end{aligned} \quad (25)$$

This downwash is determined for all doublet-lattice panels contained in the planform regions of the flaps. In the flap region, the panels for the cantilever wing examples are shown in Figure 4. The forces due to the flaps can be calculated in a similar manner as that for general wing motion.

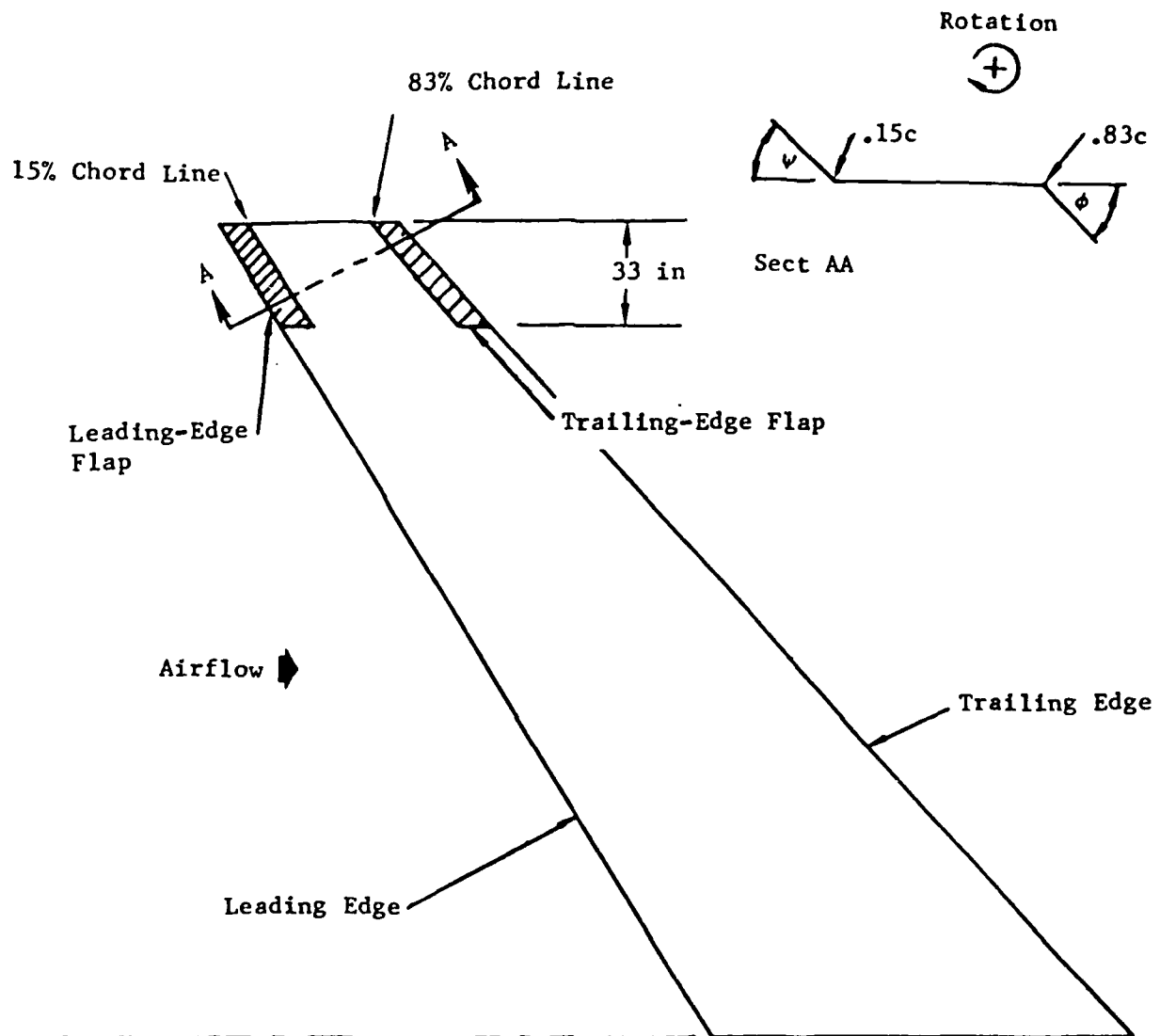


Figure 5 Leading- And Trailing-Edge Flap Geometry For The Wing

$$\begin{aligned}
\left\{ F(t) \right\}_{\text{flap}} &= [\tilde{A}] \begin{Bmatrix} 0 \\ 0 \\ w_j(t) \\ 0 \end{Bmatrix} \\
&= [\tilde{A}] \left\{ W \right\} \phi
\end{aligned} \tag{26}$$

The vector expression  $W$  contains the downwash specifications (equation 25) for each control point in matrix form. The deflection angle has been factored out to make equation 26 easier to combine with the feedback loops. To be compatible with the equations of motion, the flap forces are generalized into the modal coordinate system using the  $E$  matrix evaluated at the quarter chord points of the panels.

$$\begin{aligned}
\left\{ Q(t) \right\}_{\text{flap}} &= [E]_{1/4 \text{ chord}}^t [\tilde{A}] \left\{ W \right\} \phi \\
&= \left\{ \hat{A} \right\} \phi
\end{aligned} \tag{27}$$

Equation 27 provides generalized forces over the entire wing caused only by flap oscillations at a reduced frequency  $k$ . Padé Approximants for these generalized forces are then calculated using the sinusoidal forces from equation 27 at each of the  $k$  values. These Padé Approximants are created by the least-squares fitting described earlier. However, the fitting for the control surface forces uses as a fixed denominator the one used for approximations in equation 22. The resulting matrix equation for the flap forces has a common-denominator polynomial in the Padé Approximants that permits them to be easily combined with other aerodynamic forces in the cantilever-wing equation of motion.

$$\begin{aligned}
\begin{Bmatrix} \bar{Q}_1 \\ \vdots \\ \bar{Q}_N \end{Bmatrix} &= \frac{1.}{\bar{Q}_2 s^2 + \bar{Q}_1 s + 1.} \begin{Bmatrix} P_{31} s^3 + \dots + P_{01} \phi \\ \vdots \\ P_{3N} s^3 + \dots + P_{0N} \phi \end{Bmatrix}_{\text{flap}} \bar{\phi} \\
&= \left\{ \bar{\hat{A}} \right\} \bar{\phi}
\end{aligned} \tag{28}$$

A similar development provides generalized forces caused by the leading-edge flap.

In the next section, the control laws are defined, relating the flap angles to the measured motion of the wing. By properly selecting these laws, the control surface forces just developed can be used to stabilize both flutter and divergence of forward-swept cantilever wings.

### Feedback Control Laws

In this dissertation, active control is applied to increase the speed at which the aeroelastic instabilities occur. The stabilizing forces of the active-control system are created by the aerodynamic-control surfaces as they are activated according to measured wing motion. Feedback loops contain the links (or control laws) between the flaps and the measured elastic displacement, velocity, and/or acceleration used to activate the flaps. The control laws can be written as equations containing constants that represent simple gain amplifiers, where these amplifiers define linear relationships between wing motion and flap deflection. When these constants (or gain values) are properly chosen, the feedback loops containing them are capable of stabilizing the aeroelastic responses of the wing.

Figure 6 contains the block diagram for the wing feedback control system. Equations relating the wing motion and forces acting on it have been previously developed which include forces due to control-surface motion. These force and motion relationships are contained in the transfer functions of the wing or "plant" block. The wing block has input variables as control surface deflections  $\delta$  and  $\dot{\delta}$  and output variables as measured wing motion at two spatial locations  $h_1$  and  $h_2$ . The relationships between the wing output and the actuator inputs are depicted in Figure 6 as the  $\bar{H}_{ij}$  blocks for the control laws. The signal paths containing the  $\bar{H}_{ij}$  blocks represent the feedback network for the wing aeroelastic stability compensation. The exact types of motion sensed at the two wing locations are prescribed in the transfer functions  $\bar{H}_{ij}$ . As measurement signals, the feedback loops use the wings vertical (out-of-plane) motion. The particular dynamics of a given type of sensor device measuring this motion

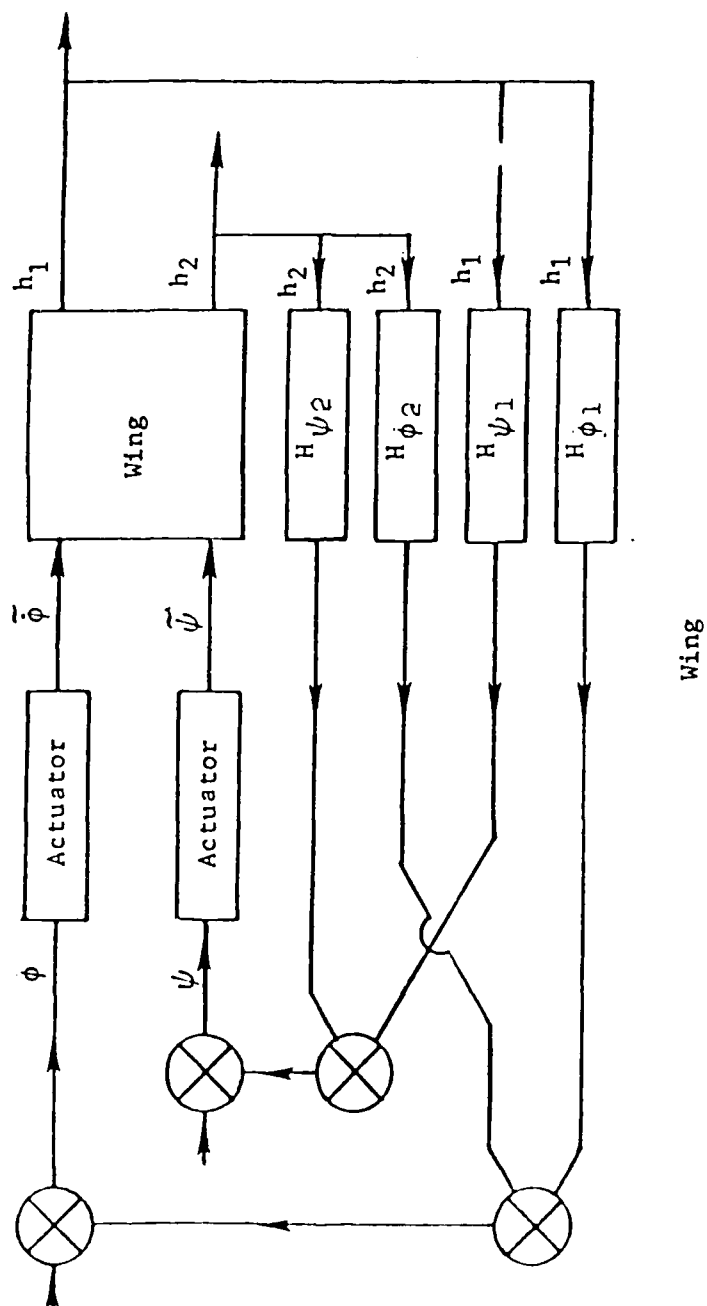


Figure 6 Feedback Loops For The Forward Swept Wing Compensation

are not included in the mathematical modeling of the feedback loop. However, devices exist that could be used to provide the necessary measurements, including strain gauges, rate gyros, accelerometers, and optical sensors. Nevertheless, only elastic motion of the cantilever wing is measured. For applications of these control laws to actual flying hardware, care is required to cancel out rigid-body motion or control-surface inputs supplied by the pilot. The cancelling of these unwanted measurements can be done using signals from rigid-body motion sensors located near the aircraft's center-of-gravity, or various low-frequency filters can be included in the feedback loops.

The measured elastic motions of the wing can be represented mathematically at the sensor locations using equation 1, when it is evaluated at the  $x, y$  locations for the sensors. In the matrix notation of the transformed complex plane, the measured motion can be written in terms of the natural modes and transformed coordinates.

$$\begin{Bmatrix} \bar{h}(x_1, y_1) \\ \bar{h}(x_2, y_2) \end{Bmatrix} = \begin{bmatrix} u_1(x_1, y_1) & \cdots & u_N(x_1, y_1) \\ u_1(x_2, y_2) & \cdots & u_N(x_2, y_2) \end{bmatrix} \begin{Bmatrix} \bar{a}_1 \\ \vdots \\ \bar{a}_N \end{Bmatrix} \quad (29)$$

$$= \begin{bmatrix} E_1 \\ E_2 \end{bmatrix} \begin{Bmatrix} \bar{a} \end{Bmatrix}$$

At these locations the velocities and accelerations are just the derivatives of  $\bar{h}(x_1, y_1)$  and  $\bar{h}(x_2, y_2)$ . In the transformed plane, these motions are a function of  $s$ .

$$\mathcal{L} \begin{Bmatrix} \dot{\bar{h}}_1 \\ \dot{\bar{h}}_2 \end{Bmatrix} = \begin{bmatrix} E_1 \\ E_2 \end{bmatrix} s \begin{Bmatrix} \bar{a} \end{Bmatrix} \quad (30)$$

$$\mathcal{L} \begin{Bmatrix} \ddot{h}_1 \\ \ddot{h}_2 \end{Bmatrix} = \begin{bmatrix} E_1 \\ E_2 \end{bmatrix} s^2 \begin{Bmatrix} \bar{a} \end{Bmatrix} \quad (31)$$

The transfer functions  $\bar{H}_{ij}$  using these wing-motion measurements are polynomials of the variable  $s$ . The real coefficients  $K_{ijl}$  of the polynomials represent linear amplifiers. Their sign determines the sign sense of the signal going to the flap actuators. Together they define the actuator signal derived from measured elastic displacements, velocities, and accelerations. Since the coefficients of  $s$  are constants, they are equivalent to simple gain amplifiers that scale the measured displacements, velocities, and accelerations. These measurements correspond to the powers of  $s$ . An example of these functions,  $\bar{H}_{\phi 1}$ , is given in equation 32.

$$\begin{aligned} \bar{\phi} &= \bar{H}_{\phi 1} \bar{h}_1 \\ &= (K_{d\phi 1} + sK_{v\phi 1} + s^2 K_{a\phi 1}) \bar{h}_1 \end{aligned} \quad (32)$$

The notation uses for the gain values  $d$ ,  $v$ , and  $a$  as subscripts for gains associated with displacements, velocities, and accelerations measured at the sensor locations. This notation facilitates references to specific gain values in the presentation of results. Thus, the actuator input signal for the trailing-edge flap,  $\phi$ , contains contributions from the displacement  $\bar{h}_1$ , velocity  $s\bar{h}_1$ , and acceleration  $s^2\bar{h}_1$ , measured at sensor location 1. These measurements are relatively weighted by the gain constants  $K_{d\phi 1}$ ,  $K_{v\phi 1}$ , and  $K_{a\phi 1}$ . Combining these transfer functions with the sensor measurements provides the stabilizing flap angles  $\bar{\phi}$  and  $\bar{\psi}$  in the modal coordinate system.

$$\begin{Bmatrix} \bar{\phi} \\ \bar{\psi} \end{Bmatrix} = \begin{bmatrix} \bar{H}_{\phi 1} & \bar{H}_{\phi 2} \\ \bar{H}_{\psi 1} & \bar{H}_{\psi 2} \end{bmatrix} \begin{bmatrix} E_1 \\ E_2 \end{bmatrix} \begin{Bmatrix} \bar{a} \end{Bmatrix} \quad (33)$$

There is also an actuator block for the feedback loops of Figure 6. The transfer function of this block defines the actual movement of the flap ( $\phi$  for the trailing-edge flap) using the signal input to the flap actuator ( $\bar{\phi}$

for the trailing-edge flap). The transfer function used is given in equation 34 and represents that used for the F-16 flutter-suppression studies of Reference 23.

$$\frac{\ddot{\phi}}{\dot{\phi}} = \frac{20.}{s + 20.} \quad (34)$$

Note that the corner frequency for this actuator is 20 rad/sec and represents reasonable capabilities in state-of-the-art electro-hydraulic actuators. In addition to the flap angles resulting from equation 33, this transfer function of the flap actuator must be included in the feedback loops.

Applied to the cantilever wing, the stabilizing forces of the feedback-control system can be calculated using the flap angles of equation 33 and the forces that result from them (in equation 28). The actuator-transfer function must be included in the loops to represent correctly the actual time-dependent deflection angle of the control surfaces.

$$\left\{ \ddot{Q} \right\}_{\text{flaps}} = \frac{20.}{s+20.} \left[ \begin{matrix} \left\{ \ddot{\hat{A}} \right\} \\ \left\{ \ddot{\hat{w}} \right\} \end{matrix} \right] \left[ \begin{matrix} \bar{H}_{\phi 1} & \bar{H}_{\phi 2} \\ \bar{H}_{w 1} & \bar{H}_{w 2} \end{matrix} \right] \left[ \begin{matrix} E_1 \\ E_2 \end{matrix} \right] \left\{ \ddot{a} \right\} \quad (35)$$

The stabilizing forces are then written as influence-coefficient matrices of complex constants that are then post-multiplied by the wing's modal displacement vector and its time derivatives. Now the stabilizing forces, including the feedback loops, are compatible with the wing equations of motion. When the gains in the  $\bar{H}_{ij}$  compensation block are properly adjusted, the wing is more aeroelastically stable. To determine the aeroelastic stability, the next section describes the solution method used on the resulting cantilever wing's equations of motion.

#### Stability Solution Method

The aeroelastic stability of the cantilever wing is determined from the transformed equations of motion just described by subjecting the wing to an impulse disturbance. With this type of disturbance, the system's



stability can be described, using only the roots of the characteristic equation obtained from the equations of motion (Ref. 24). These roots specify the poles of the system's response in the complex plane and can be found by identifying values that make the determinant of the characteristic equation go to zero.

The stability of the lifting surface is indicated by the real parts of these roots of the characteristic equation. As long as all of the roots have negative real parts, stability is implied. Neutral stability is acquired when any of their real parts go to zero. Negative stability (or instability) occurs when any of the real parts of the roots of the characteristic equation become positive. Changing parameters in the equations of motion and thus the characteristic equation (such as an increase in airspeed or an amplifier gain) causes changes in the roots. By progressively changing one of these parameters, loci of the roots in the complex plane can be developed corresponding to those parameter changes. The root loci can then be used to calculate the parameter values that will provide roots with the most desirable characteristics for wing stability. Usually the optimum parameter values will result in roots with maximum negative real parts. Later, in presenting results, the loci of these roots (caused by parameter changes) in the complex plane are used to illustrate the effects of parameter changes on the wing stability.

A direct method to calculate the characteristic roots can be used when the Padé Approximants provide the aerodynamic-force formulation. The Padé Approximants allow the equations of motion to be written as a collection of constant-coefficient matrices multiplied by the displacement vector and its derivatives. When put in first-order form, the calculation of the roots becomes a standard eigenvalue problem involving complex-constant matrices.

When the homogenous cantilever wing equations of motion are organized in first-order form, the degrees-of-freedom and their derivatives are combined in a new vector  $\hat{a}$ . This vector contains states defined by the degrees-of-freedom and their derivatives, up to the fourth time derivative. This fourth derivative is dictated by the third-order denominator

polynomials in  $s$  found in the generalized forces. These polynomials are created from the denominators of the Padé Approximants and that of the actuator. When these are multiplied by the accelerations of the inertia terms, a fifth derivative in time is created.

$$\begin{pmatrix} \dot{a} \\ a \\ \ddot{a} \\ \dddot{a} \\ \ddot{\ddot{a}} \end{pmatrix} = [\hat{A}] \begin{pmatrix} a \\ \dot{a} \\ \ddot{a} \\ \ddot{\ddot{a}} \\ \ddot{\ddot{\ddot{a}}} \end{pmatrix} \quad (36)$$

$$\{\hat{\ddot{a}}\} = [\hat{A}] \{\hat{a}\}$$

The  $\hat{A}$  matrix contains only complex constants that include the terms of mass, stiffness, feedback compensation, and aerodynamic force found in their influence coefficient matrices. In the transformed plane, equation 36 exhibits the form for eigenvalue problems.

$$s \{\hat{\ddot{a}}\} = [\hat{A}] \{\hat{a}\}$$

$$\left[ [\hat{A}] - s[I] \right] \{\hat{\ddot{a}}\} = 0 \quad (37)$$

The characteristic determinant for equation 37 becomes equation 38.

$$\left| [\hat{A}] - s[I] \right| = 0 \quad (38)$$

The roots  $s$  of this determinant (which are the eigenvalues of equation 38) describe the stability of the cantilever wing.

The eigenvalue problem of equation 38 can be solved using existing computer programs (Ref. 25) written for problems involving nonsymmetric complex matrices. The mathematical bases for the computer routine used in this research are outlined in Reference 26. The  $\hat{A}$  matrix is first put in Hessenberg form (equation 39) using a sequence of matrix reflection operations called Householder's method.

$$\begin{array}{c} \hat{\hat{A}} \\ [\hat{A}] \\ \text{Hessenburg} \end{array} = \begin{bmatrix} \hat{\hat{A}}_{11} & \hat{\hat{A}}_{12} & \cdots & & & \hat{\hat{A}}_1 & 5N \\ \hat{\hat{A}}_{12} & \hat{\hat{A}}_{22} & \cdots & & & \hat{\hat{A}}_2 & 5N \\ 0 & \hat{\hat{A}}_{32} & \hat{\hat{A}}_{33} & \cdots & & \hat{\hat{A}}_3 & 5N \\ 0 & 0 & \hat{\hat{A}}_{43} & \hat{\hat{A}}_{44} & \cdots & \hat{\hat{A}}_4 & 5N \\ \vdots & \vdots & & & & \vdots & \\ \vdots & \vdots & & & & \vdots & \\ \vdots & \vdots & & & & \vdots & \\ 0 & 0 & \cdots & \hat{\hat{A}}_{5N-1} & 5N-1 & \hat{\hat{A}}_{5N} & 5N \end{bmatrix} \quad (39)$$

A series of similarity transformations in the QR-algorithm puts  $\hat{\hat{A}}$  in an upper triangular form with the eigenvalues on the diagonal.

While freestream velocity and all the feedback gains must be fixed to define completely  $\hat{\hat{A}}$ , the interval over which any of these parameters is varied (to develop loci of the roots with that parameter change) is completely arbitrary. Starting at zero velocity or zero feedback gain is not required, and all the eigenvalues are calculated each time to avoid overlooking a particular branch of the root loci. This is especially useful for any fine tuning of feedback gains. To develop the loci of characteristic roots caused by variations in a particular parameter (such as flow velocity), a series of values of that parameter is chosen. The number of parameter values and the intervals between them required to construct root loci are dictated only by the parameter range of interest and the ease in following the changes in eigenvalues. The recalculation of  $\hat{\hat{A}}$  as that parameter is changed is simple and fast. The expensive and time consuming aerodynamic force calculations using the doublet-lattice procedure must be made only once and do not have to be repeated.

With the control surface forces and the feedback loops that drive them included in the wing equations of motion, the study of improved aeroelastic stability of forward sweep can begin. The following study focuses on two wing examples that illustrate possible applications of active control for forward sweep aeroelastic instabilities. In this next chapter the two wing

examples are examined with 96 possible feedback loops. Several show promise of improvement in wing stability. Two of these feedback loops are examined in detail.

### III - WING ACTIVE CONTROL STUDIES

In this chapter, the application of active controls to forward-sweep is illustrated with two forward-swept wing examples. The goal is to improve their flutter and divergence characteristics. A gain-parameter root-locus for each combination of control surface, sensor, and gain sign is calculated. These loci are used to determine the best feedback loops for the improvement of flutter and divergence. Several plots of these root loci are included to illustrate the effects of particular gain changes. Associated velocity root loci are also presented to show the improvements or losses in stability for selected feedback loops. The results show that even with the small flaps used here, active control can improve aeroelastic stability.

The cantilever wings used as examples are derived from a single forward-swept configuration. This wing configuration is representative of the first generation of forward-swept wing designs in the high g fighter category. The basic geometry is derived from example designs in Reference 6. This geometry was chosen to make the application studies of this research representative in weight and basic geometry of actual flight hardware. The two wing examples use the same external geometry as shown in Figure 3. These wings are designed for an 18000 pound aircraft performing an 8g symmetric pullup at .9 Mach number at sea level altitude. The flow condition used in the doublet-lattice analysis for the Padé Approximants is .9 Mach number at sea level. However a match-point analysis is not performed for the critical airspeeds calculated in the following examples. This match-point analysis would correct the critical velocities to the proper Mach number and altitude. The match-point analysis would be included in the detailed calculations made when these control laws are applied to actual hardware.

The active control system uses one or both outboard flaps shown in Figure 3. The hinge lines are at the 15% and 83% chord lines. The 15%

chord line is the leading-edge spar location for the wing's structural box. This location is necessary for attachment of the actuators and hinges. The aft hinge line is half way between the structural box's trailing-edge and the planform trailing-edge. This hinge line was chosen so that the trailing-edge flap would be approximately the same size as the leading-edge flap. The control surfaces are used in several combinations, prescribed in four different configurations. Configuration A uses only the trailing-edge flap. Configuration B use only the leading-edge flap. Configuration C provides equal deflection of both the leading-edge flap and the trailing-edge flap. Configuration D provides for a positive deflection for the trailing-edge flap and an equal but negative deflection for the leading-edge flap. Using these last two control surface configurations, the desirability can be examined of a control force that resembles either an aerodynamic torque (Configuration C) or an aerodynamic plunge force (Configuration D).

The wing-motion sensors are located on the periphery of the structural box at its mid-plane in depth. One location is the junction of the tip rib and leading-edge spar for the wing box. The other location is on the trailing-edge spar directly downstream from the first location. Figure 7 shows these locations on the wing planform. Like the control surfaces, the sensors are used in four configurations. The sensor of Configuration A produces signals only from the trailing-edge location. Sensor B produces signals only from the leading-edge location. Sensor C adds the signals from the leading-edge and trailing-edge locations. Sensor D subtracts the signal of the leading-edge location from that of the trailing-edge location. The first two configurations yield sensor signals from locations near the control surfaces. The latter two configurations yield signals that represent primarily plunge motion (Sensor C) or pitch motion (Sensor D) at the span station of the sensors. However, configurations C and D are not intended to selectively recover a particular vibration mode from the wing response, as has been done in some active-control investigations (Ref. 27). In fact, a major concern that suggests these latter two sensor configurations is avoidance of single-sensor locations at node lines of the

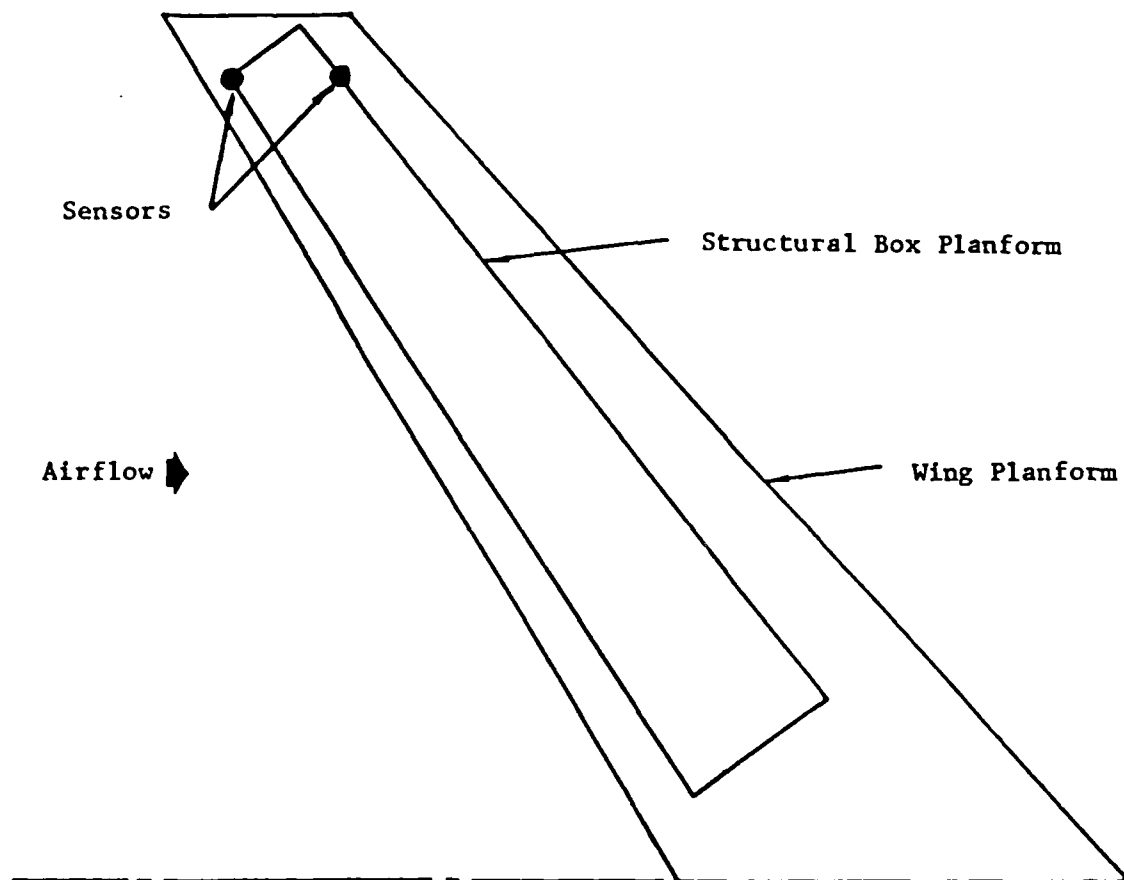


Figure 7 Sensor Locations For The Wing

low-frequency modes. Sensors C and D better ensure the observability of all modes.

Three kinds of sensors can be used with any of the location configurations. These sensors would be displacement, velocity, or acceleration-measuring instruments. The kind chosen for each feedback loop dictates the control law used. The measurement signals provided by the sensors are scaled by linear amplifiers (gain constants) and directly input to the flap actuators. No other signal processing is done, such as differentiation or integration of the sensor signal.

The different combinations of configurations in sensor location and flap are examined with a gain-parameter root locus, using each kind of sensor. The root loci are calculated using both negative and positive feedback. For a given wing box design then, 32 possible combinations (4 sensor configurations, 4 flap configurations, and 2 signs for gain values) of feedback circuits are examined. These gain-parameter root loci are calculated at a fixed speed that corresponds to the most critical instability. Using the gain-parameter root loci, gain values are chosen for wing stability improvements based on improvement in the characteristic root locations. The gain values showing promise are checked using velocity root loci with these feedback gains in the feedback loops. Each of the 32 gain-parameter root loci is used with the displacement, velocity, and acceleration sensors to provide a total of 96 possible feedback loops for a given wing example case.

Two different wing structural-box designs, designated Case 1 and Case 2, are used for the wing feedback-control examples. The structures in these wings are devised to produce different relative airspeeds for the aeroelastic instabilities. The Case 1 example uses a wing box aeroelastically tailored to have its divergence airspeed  $U_d$  at a lower value than for flutter  $U_f$ . The Case 2 design has the relationship of  $U_d$  and  $U_f$  reversed. But the two cases are identical in external contours, flap locations, sensor locations, and non-structural mass distributions.



Using aeroelastic tailoring of the thickness and fiber directions in the composite upper and lower wing-box covers, the flutter and divergence airspeeds were brought within 400 ft/sec of one another. Effort was made in both cases to have flutter and divergence airspeeds relatively close together. This similarity of airspeeds permits monitoring of the positive or negative effects on a secondary aeroelastic instability while attempting the control of the most critical aeroelastic instability. While flutter and divergence usually have widely separate critical airspeeds, the close proximity in aeroelastic instabilities of these examples can occur in actual aircraft designs when using automated design techniques that employ optimization algorithms. These automated techniques closely balance various design requirements while minimizing structural weight. This balance often specifies both  $U_d$  and  $U_f$  as being just outside the aircraft operating envelope.

The results for the stability study are presented in graphical form using root loci plots. These loci trace the movement of the characteristic roots in the complex plane. As a selected parameter is changed, such as an amplifier gain or freestream airspeed, the characteristic roots of the wing equations of motion also change. The loci of these roots provide a graphical way of interpreting the effects a parameter change can have on wing stability. The figures in this chapter show only the upper left-hand portion of the complex plane. Only the upper portion must be shown because the complex conjugate property of the characteristic roots make the upper and lower portions symmetric about the real axis. Only the left half-plane is shown because the subcritical root values are of prime importance. Thus, only the negative (sub-critical) values of the real parts of the characteristic roots need be plotted. The root loci plots present either velocity or gain parameter changes.

The velocity root loci describe the root movements as the freestream airspeed of the wing increases. All other wing parameters are held constant. When a wing root displays a left-to-right crossing of the imaginary axis, the damping of that root has changed from positive to negative. The airspeed corresponding to this change is the critical

velocity for stability. Similar loci can be shown for changes in a gain value rather than freestream velocity. These plots can be useful in determining gain values that indicate large damping values. Gain settings that provide large negative real parts for all of the roots usually increase wing stability.

Feedback control design using the root locus methods is an older "classical" technique. More modern methods that automate the search for optimum gain settings could be used. However, one of the goals of this research is to develop some basic understanding of the effects that particular active control laws can have. This can be observed better with the individual parameter gain root locus methods rather than modern optimal control methods. Therefore, the following case studies use only the classical root locus approach.

#### Case 1 Study

This wing design has  $U_d$  lower than  $U_f$ . Figure 8 is the velocity root locus for Case 1 with no active control present. The origin of each locus is the zero velocity condition and is found on the imaginary axis. The imaginary parts of these origin points correspond to the natural frequencies of the vacuum vibration modes for Case 1. The first four roots show the vacuum vibration frequencies for mode 1 at 5.21 rad/sec, mode 2 at 23.22 rad/sec, mode 3 at 27.67 rad/sec, and mode 4 at 58.32 rad/sec. The shapes of the loci for these modes fall into the expected classical categories for high aspect-ratio wing structures. Mode 1 can be described as a first-bending mode shape. Mode 2 is a second-bending mode. Mode 3 is the first-torsion mode. Mode 4 is the third-bending mode.

As the velocity is increased from 0 to 2200 ft/sec, the critical divergence and flutter airspeeds are identified. The mode 1 root defines the divergence velocity as this root crosses the imaginary axis. This crossing occurs at a freestream airspeed of 1161 ft/sec. Roots at the divergence velocity are noted in all the root loci by the solid round symbol. In both wing examples, the first-bending mode corresponds to the

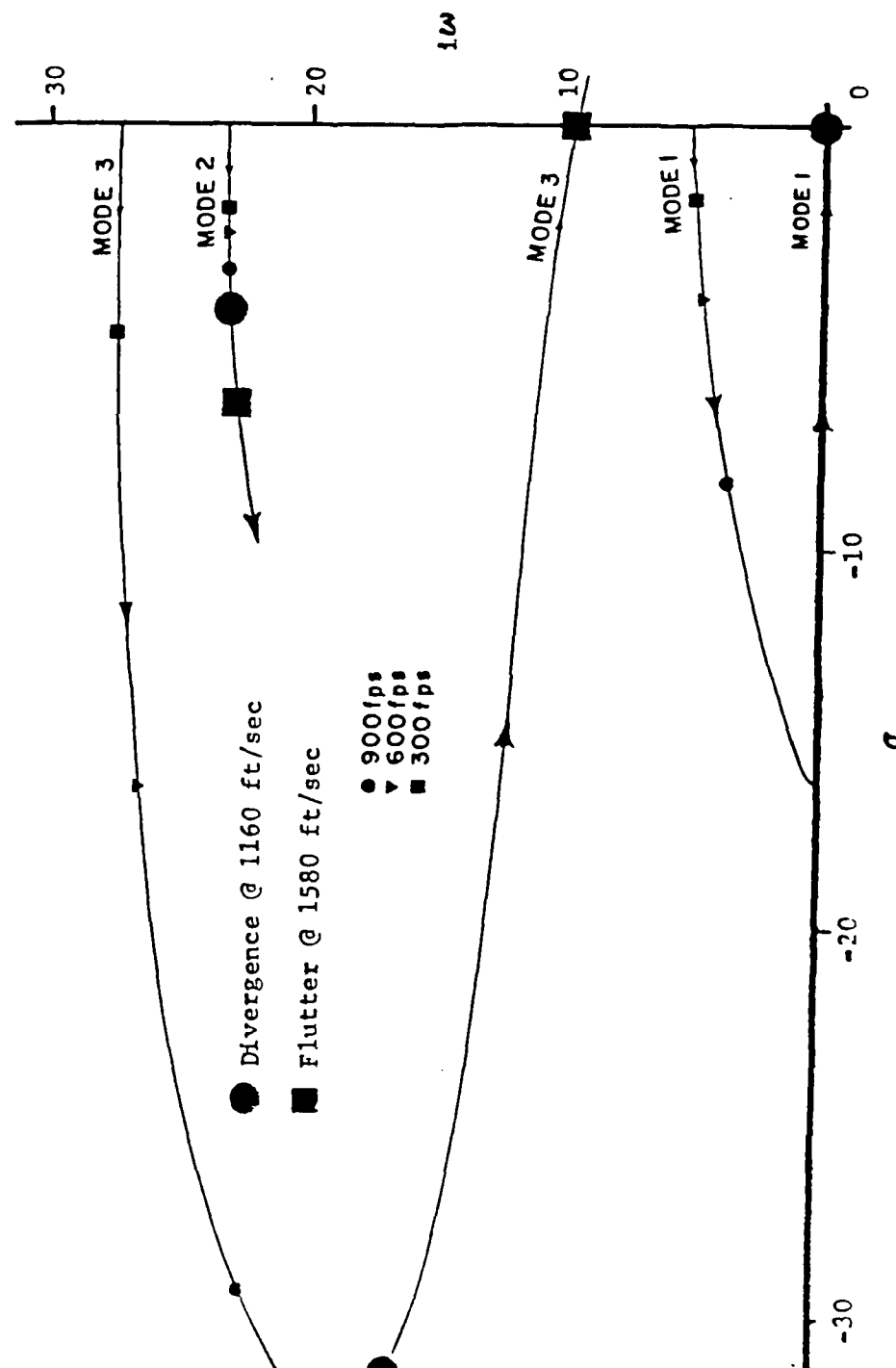


Figure 8 Velocity Root Locus For Case 1  
No Feedback

lowest-frequency vibration mode, and the eigenvector (or wing deformation shape) of the divergence condition closely resembles the first bending mode.

The most critical flutter airspeed is defined when the mode 3 locus crosses the imaginary axis at a freestream airspeed of 1560 ft/sec. Roots at the freestream velocity of flutter are noted on all loci with the solid square symbol. As in all other examples, the critical flutter airspeed is defined when the root corresponding to the lowest-frequency torsional mode crosses the imaginary axis.

The higher frequency modes continuously gain damping as velocity is increased, with no tendency to return to the imaginary axis and define other aeroelastic instabilities. For all stability calculations (unless specifically noted otherwise), the basis for the calculations is the first four vibration modes. For Case 1, the locus of mode 4 always gained damping with airspeed and produced nothing more than a progressively higher damped response. For this reason, this mode is not plotted. The following results show the effects that the addition of active control has on Case 1, and are organized according to the kind of sensor used in the feedback loops.

#### Displacement Sensing

Active control, using displacement sensing, is the first type of compensation presented, and is examined for all 32 combinations of sensor, flap, and gain signs. Several gain root loci are presented to illustrate the effect of this kind of feedback.

All of the gain root loci (for positive feedback using elastic-displacement sensing) show significant degradation in the stability of the divergence critical root. In this study, positive displacement feedback cannot be used to improve the divergence airspeed for the combinations of signal sense in displacement measurements and flap deflection angles. Even very small values of positive-displacement sensing cause the divergence critical mode 1 root to go unstable.

Negative-displacement sensing is successful in improving the critical divergence airspeed. The gain-parameter root locus plots for this feedback exhibit three general patterns. The root-loci patterns are characterized by interaction between the divergence critical roots of the first mode and the root from the control surface actuator.

With the addition of the feedback loop to Case 1, a set of four characteristic roots appears, in addition to those of the structure and aerodynamics. These four roots are all located at the  $20 \text{ sec}^{-1}$  position (in an overlaid fashion) on the real axis of the complex plane and are due to the denominator of the actuator. As the gain parameter is changed from zero to large negative values, one of these four control roots moves in a positive direction. At the same time, the critical divergence root moves in a negative real direction. This increase in the damping of the critical divergence root delays the onset of divergence to a higher airspeed. The movement of the other roots in the root locus defines the different patterns discussed below.

In Figure 9, the first pattern (of three patterns) in the root loci is seen, resulting from gain changes with displacement sensing. The critical divergence root and control root coalesce to form a complex conjugate pair. This complex pair defines a flutter instability, and involves the root that had defined a divergence instability before application of active control. In this complex pair, the higher modes show little movement with increased gain. The second pattern is illustrated in Figure 10 and differs from the first in that mode 2 quickly goes unstable in flutter. The third pattern has the conjugate roots from mode 1 and the control surface remaining stable. Figure 11 shows an example of this pattern. Here increased negative gain forces mode 3 to move towards instability. This third root-locus pattern corresponds to the best improvement in divergence with active control. It is accomplished using wing-displacement sensing.

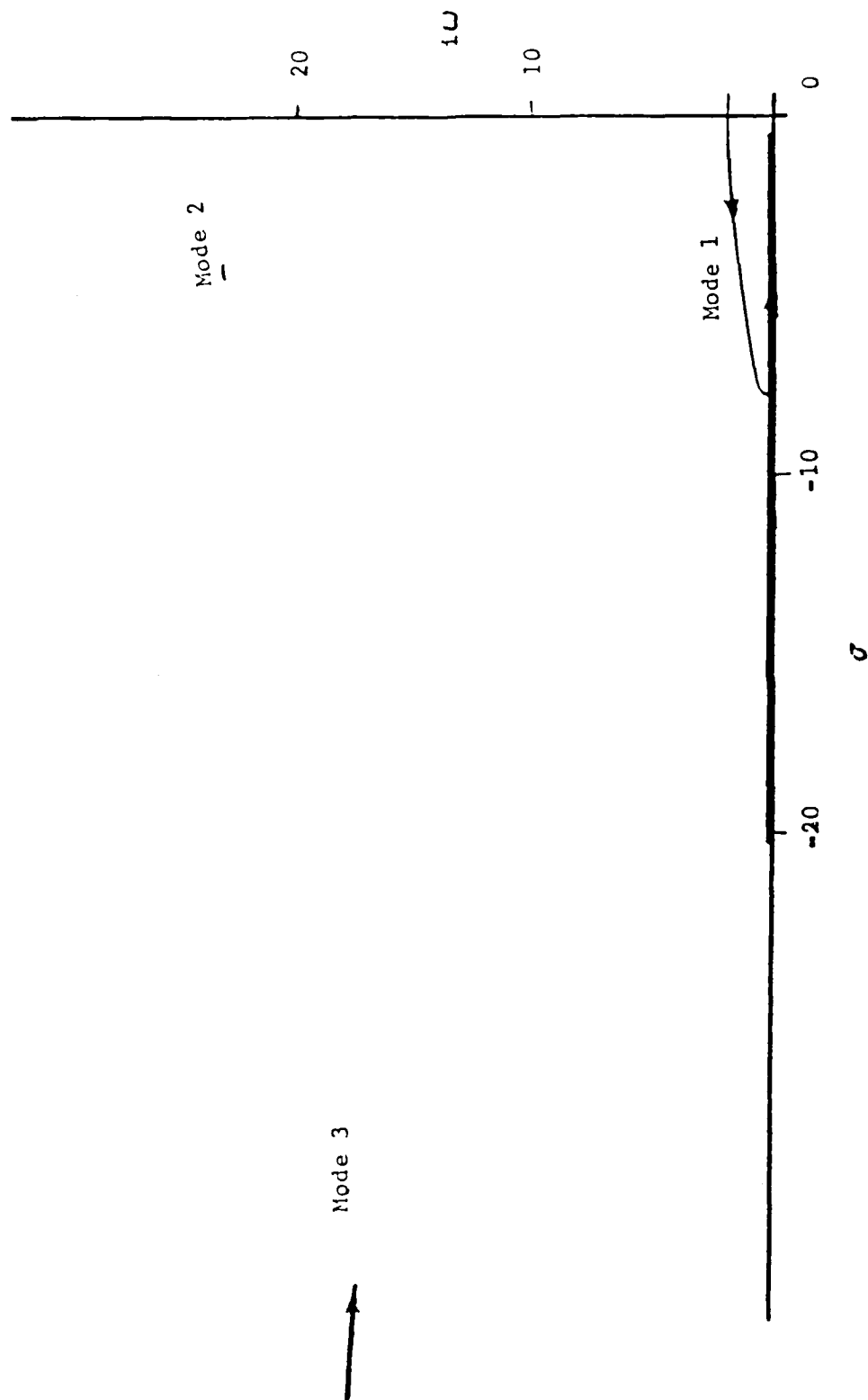


Figure 9 Gain-Parameter Root Locus For Case 1  
Sensor D/Flap D Negative Feedback  
Displacement Sensing

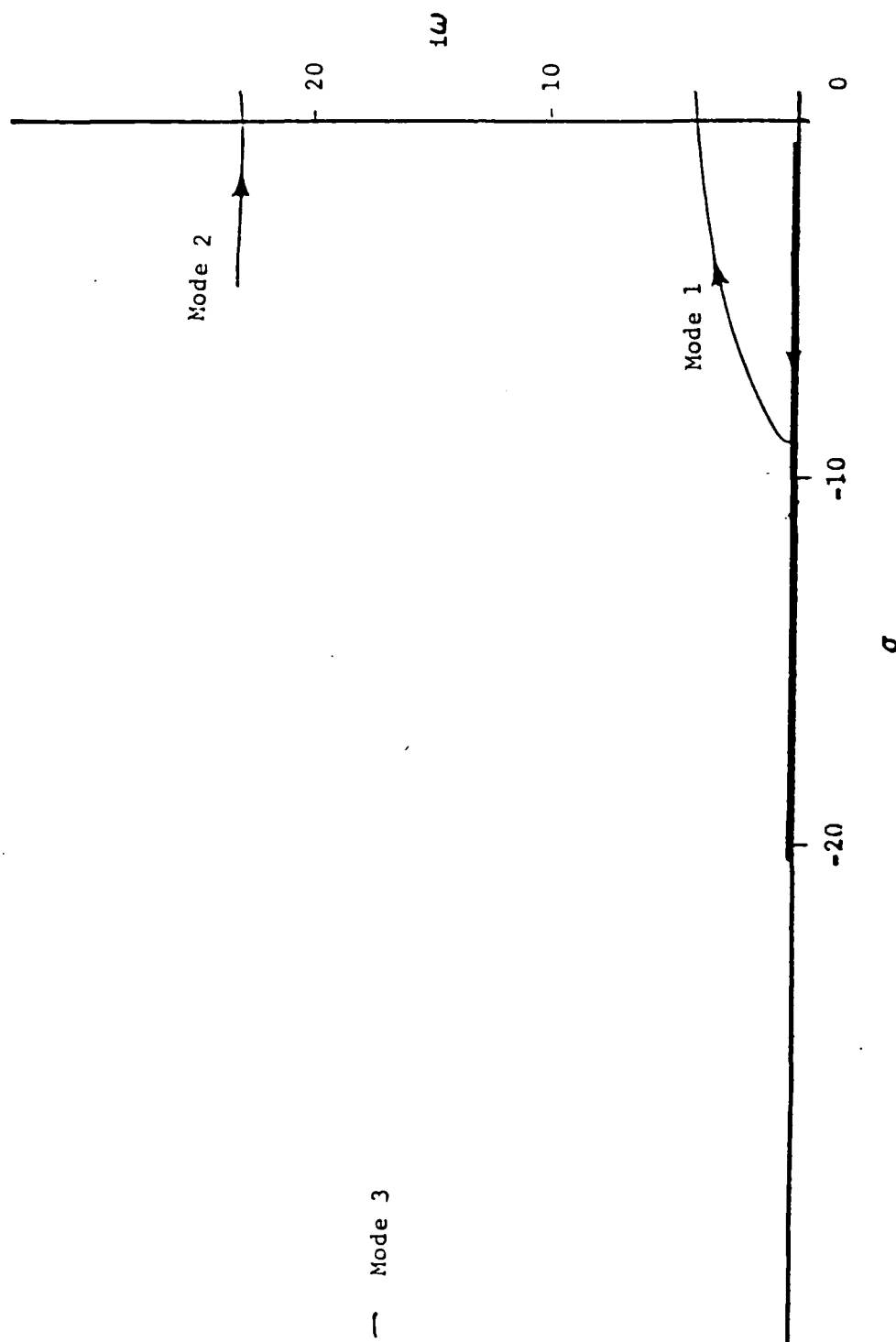


Figure 10 Gain-Parameter Root Locus For Case 1  
Sensor A/Flap A Negative Feedback  
Displacement Sensing

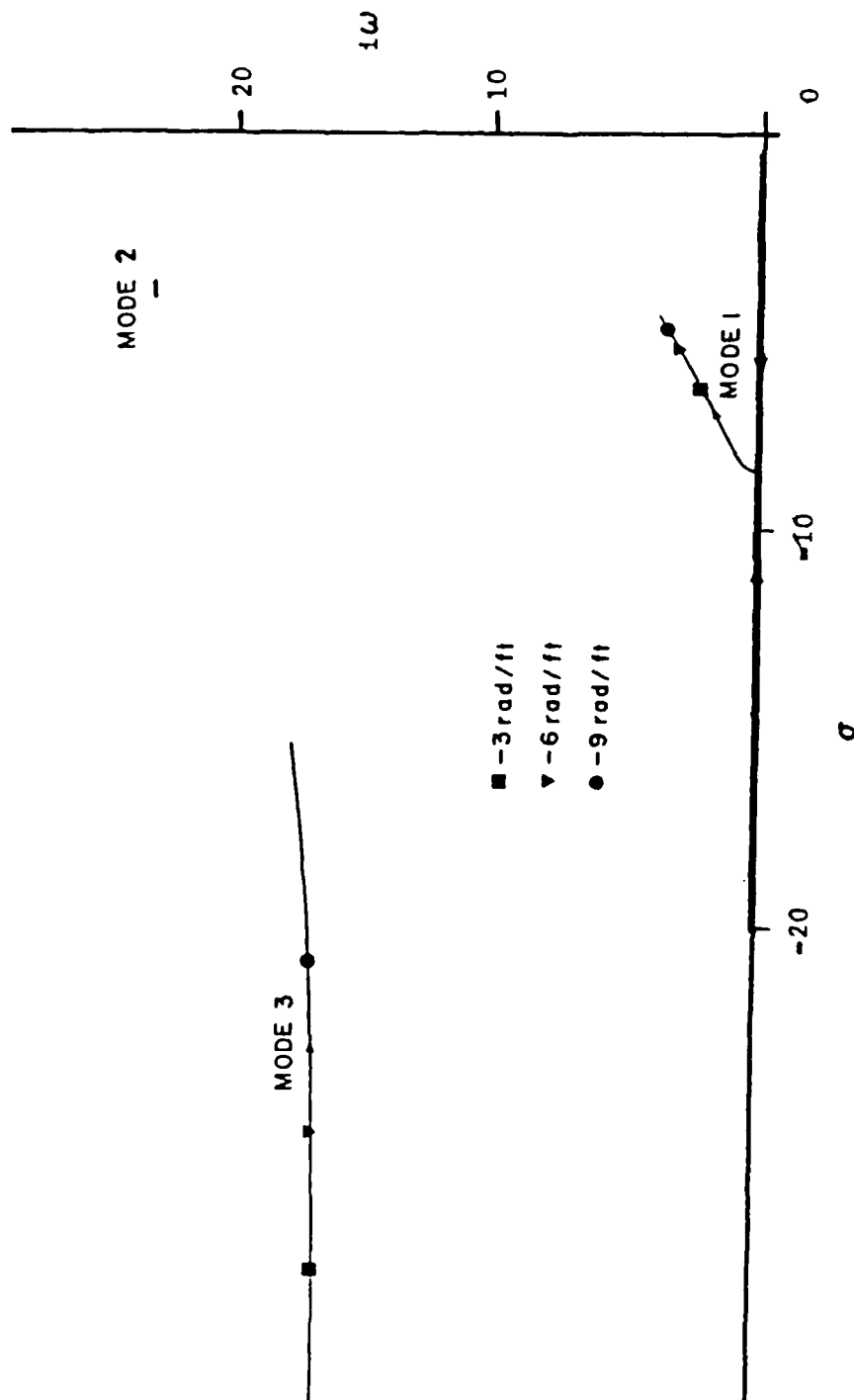


Figure 11 Gain-Parameter Root Locus For Case 1  
Sensor D/Flap B Negative Feedback  
Displacement Sensing



Figures 12 through 16 show a series of velocity root loci using the Sensor D/Flap B configuration. The loci are calculated using a different gain level for each figure. The root locations calculated at three of these gain values are noted on the gain-parameter root locus of Figure 11. Velocity root loci for these different gain levels are shown in Figures 12-14. With the Sensor D/Flap B combination, a gain of  $-3$  rad/ft produces the velocity root locus of Figure 12. In Figure 12, the velocity at divergence increases to 1345 ft/sec while the velocity at flutter drops to 1480 ft/sec. At this gain level mode 1 moves to the real axis before crossing the imaginary axis. When the gain is increased to  $-6$  rad/ft, as in Figure 13, the critical velocities are equal (1448 ft/sec) for the crossings of mode 3 (for flutter) and mode 1 (for divergence). As the gain is further increased to  $-9$  rad/ft, the break-in point for the roots of mode 1 move to the positive side of the real axis. Therefore, as shown in Figure 14, mode 1 now prescribes a secondary flutter instability rather than divergence. But the most critical flutter instability is still defined by mode 3. However, it now crosses at an even lower velocity of 1389 ft/sec.

When displacement sensing is used in Case 1, the  $-6$  rad/sec gain value provides the best improvement in velocity of the most critical aeroelastic instability. Raising the divergence velocity is accomplished, however, at the expense of lowering the most critical flutter velocity. This trade in critical velocities suggests that large increases in divergence speed for Case 1 might be possible if the flutter velocity had been much higher. Fortunately, high flutter velocities are typical in the forward-sweep designs using conventional materials, as suggested by Figure 1.

The velocity root loci in Figures 15 and 16 show the results of further increases in gain. When the negative gain is further increased, the flutter speed continues to drop. When the gain reaches  $-15.5$  rad/ft, mode 1 does not go unstable at all, but mode 3 indicates a still lower critical velocity for flutter at 1316 ft/sec.

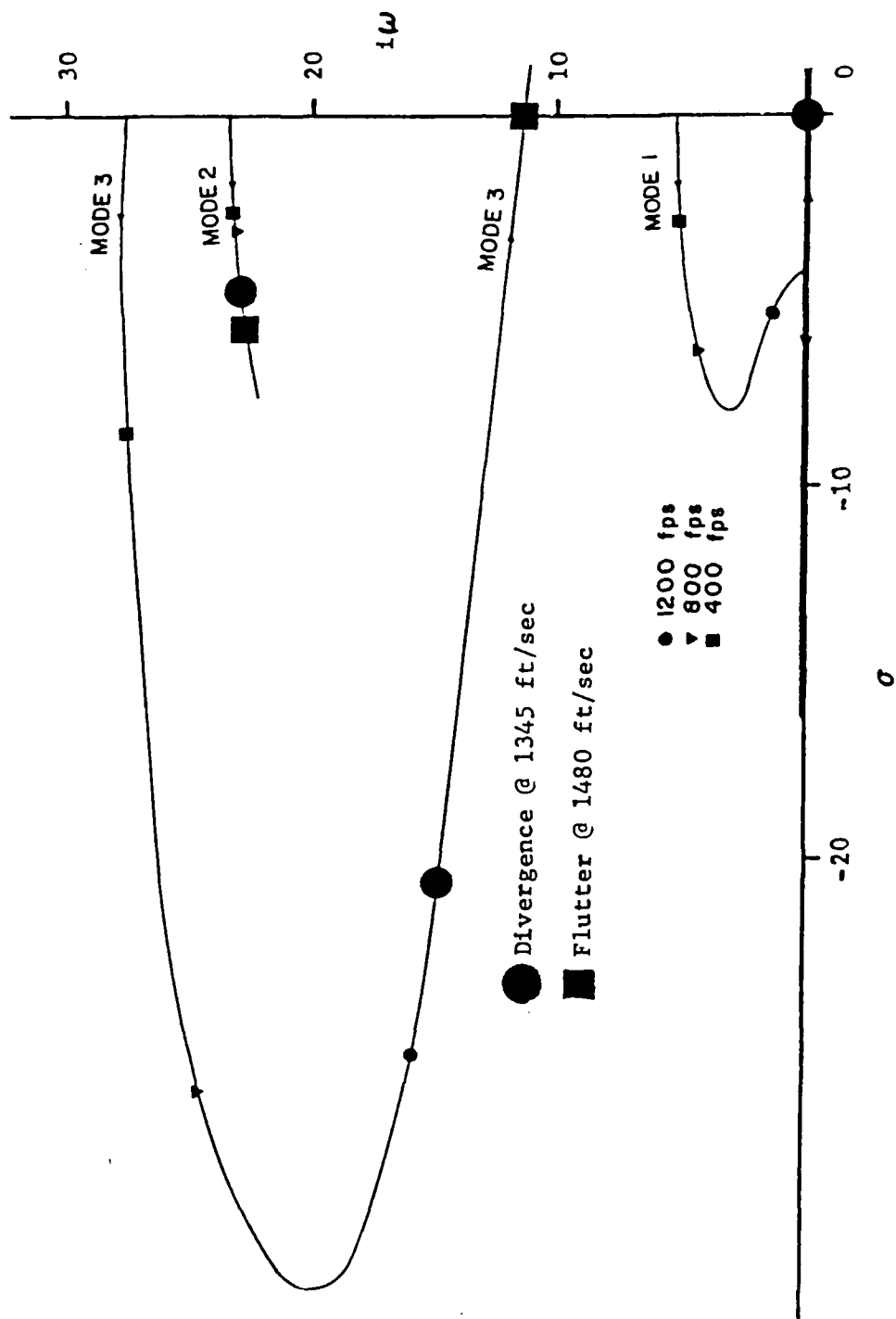


Figure 12 Velocity Root Locus For Case 1  
Sensor D/Flap B  $K_d = -3$  rad/ft

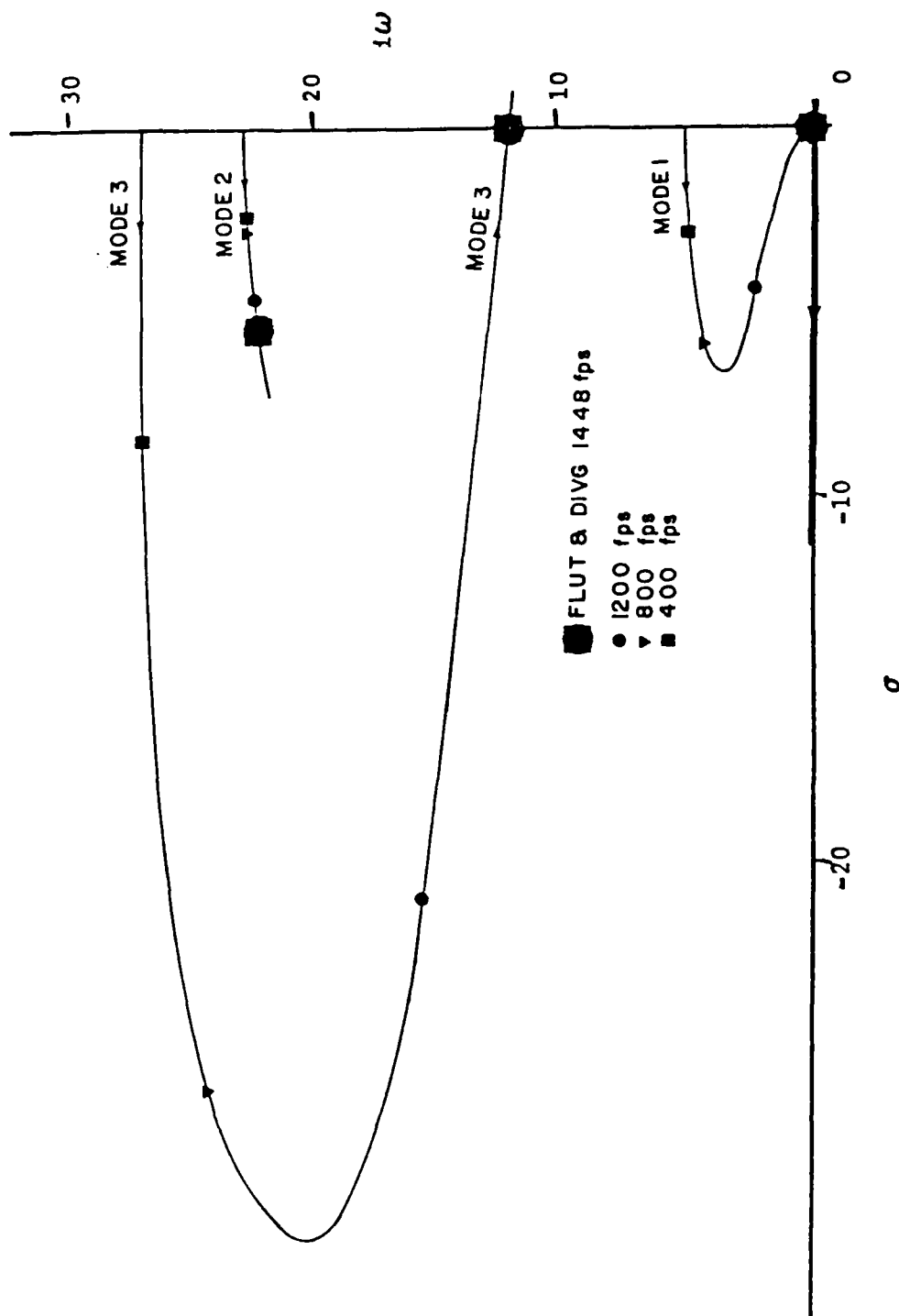


Figure 13 Velocity Root Locus For Case 1  
Sensor D/Flap B  $K_d = -6 \text{ rad/ft}$

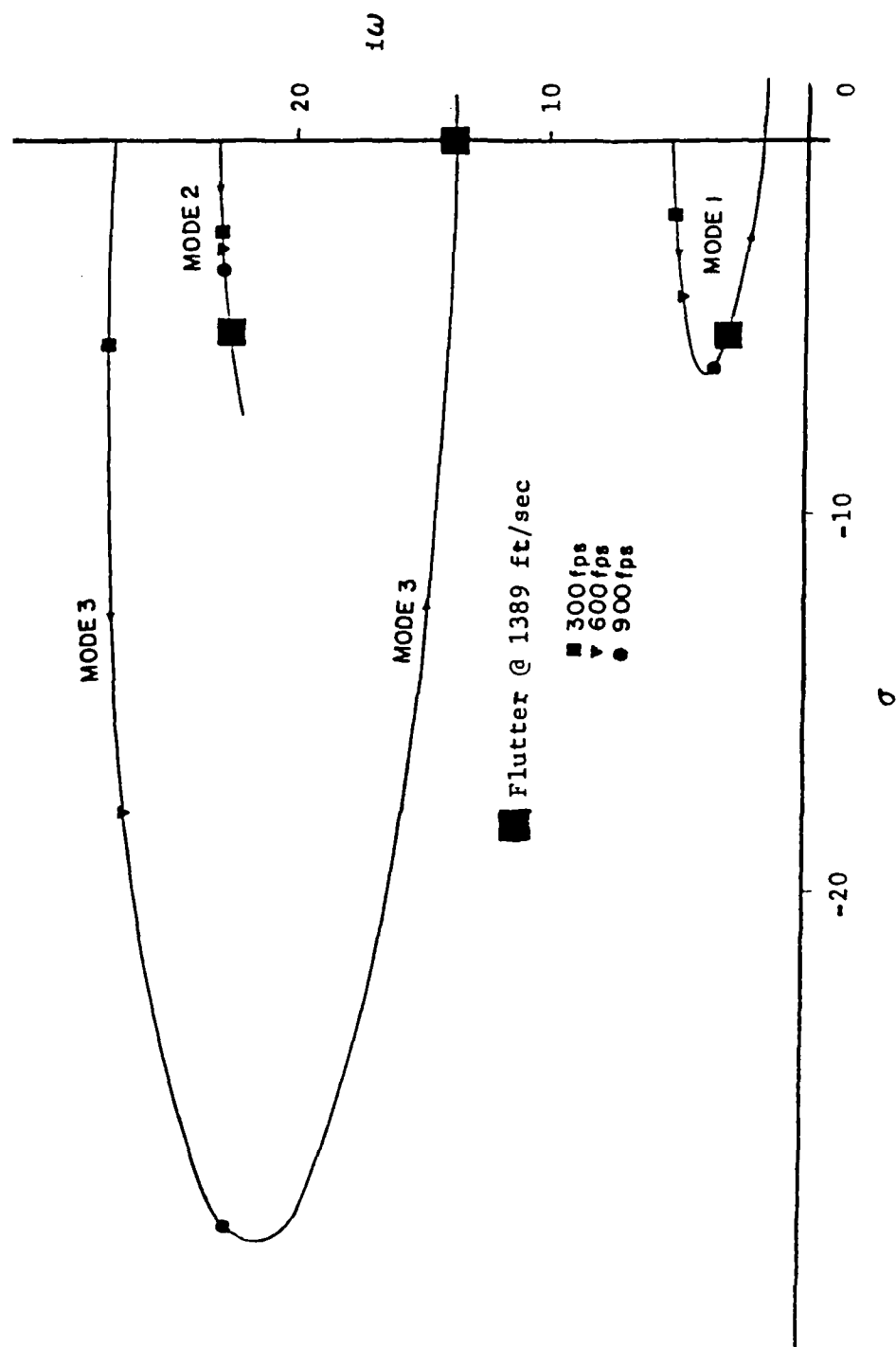


Figure 14 Velocity Root Locus For Case 1  
Sensor D/Flap B  $K_d = -9 \text{ rad/ft}$

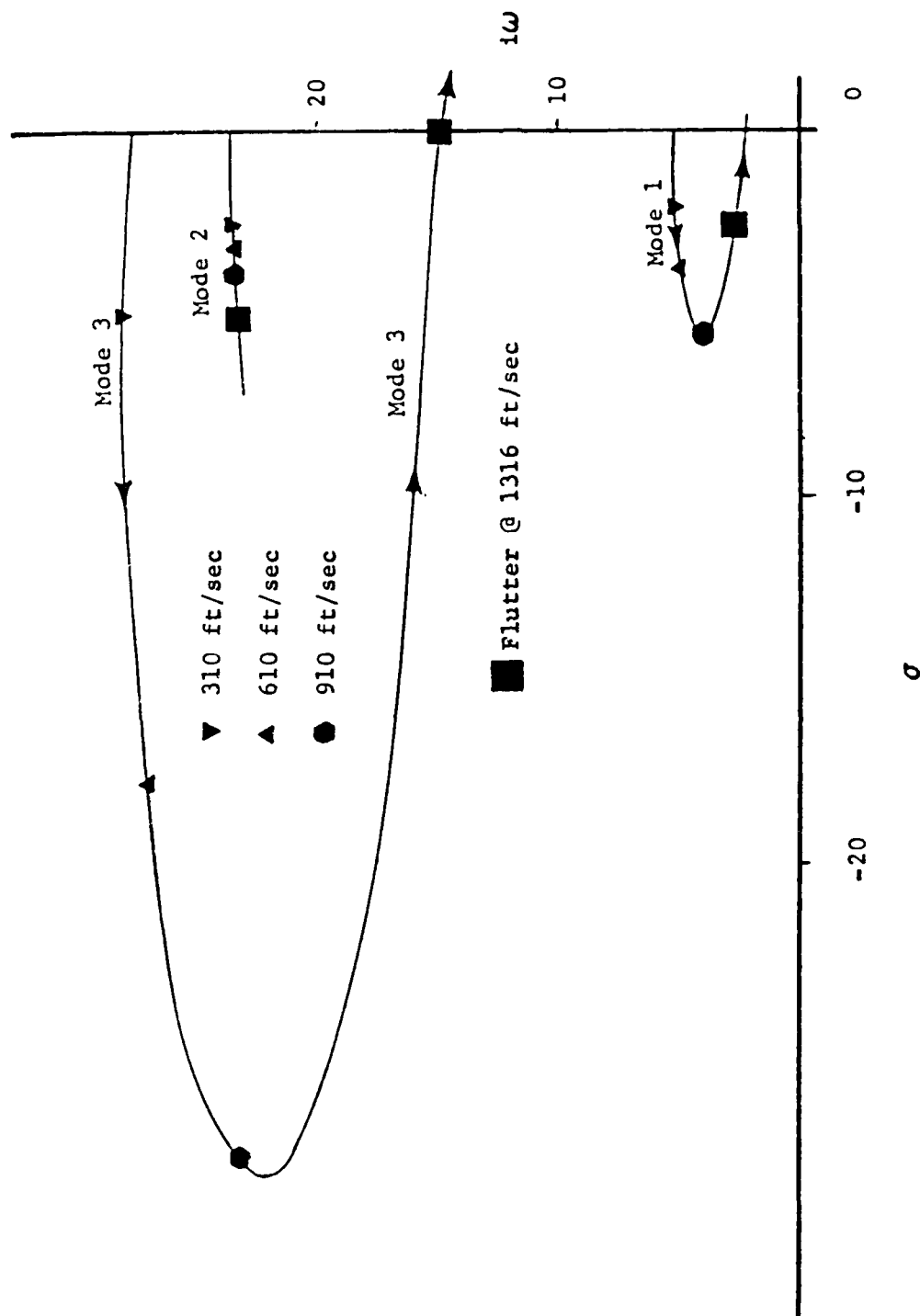


Figure 15 Velocity Root Locus For Case 1  
Sensor D/Flap B  $K_d = -12 \text{ rad/ft}$

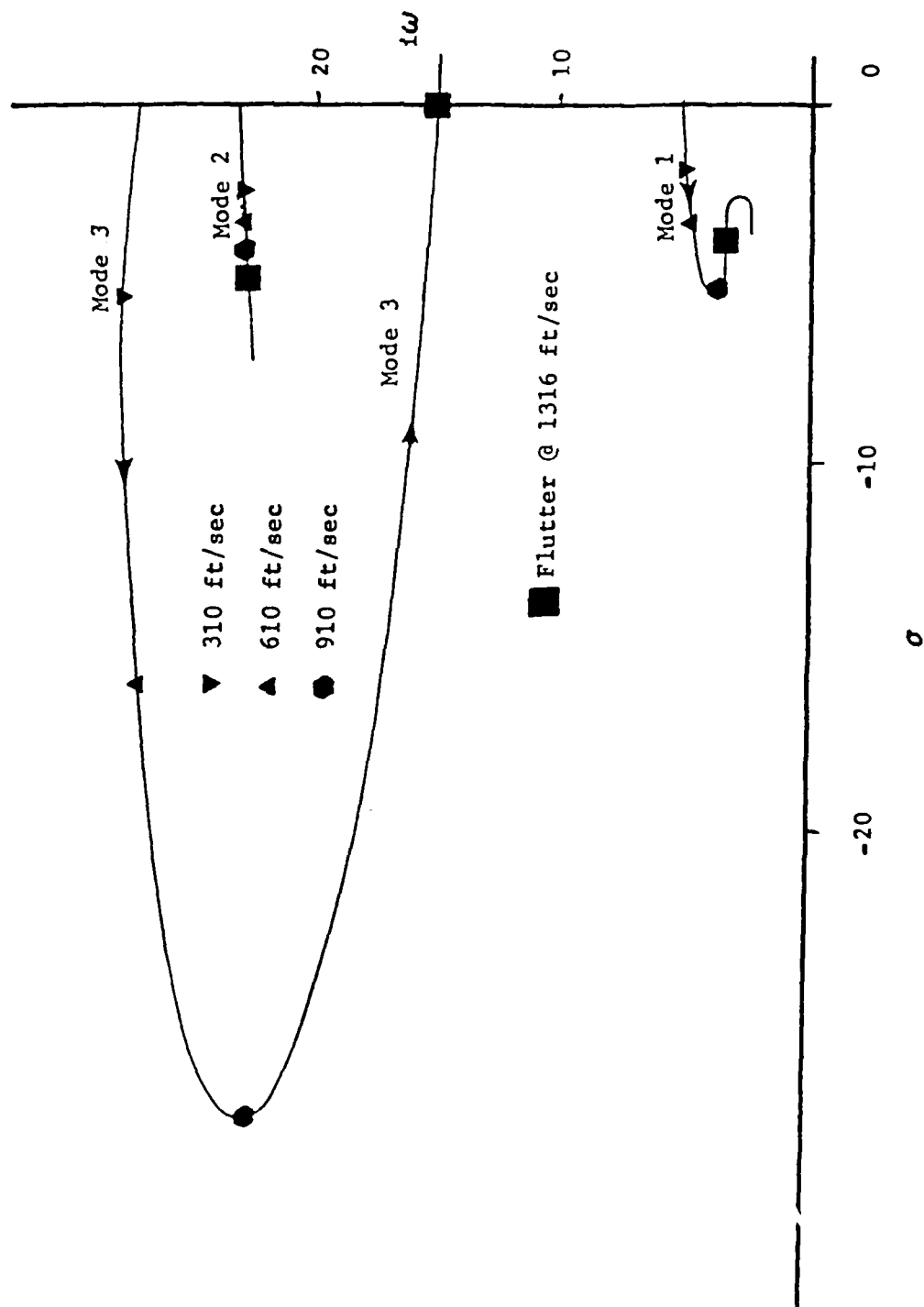


Figure 16 Velocity Root Locus For Case 1  
Sensor D/Flap B  $K_d = -15.5 \text{ rad/ft}$

The previous root loci plots used a basis of four modes. To check the sensitivity of all the analyses to the number of modes used as a basis, both in describing the essential responses of the wing and in the Padé fitting process, a new stability calculation is made. This time 10 modes are used rather than 4. The gain  $K_d$  is again set at -6 rad/sec in the Sensor D/Flap B configuration. Using 10 modes as the basis, the flutter and divergence speed are calculated to be 1432 ft/sec, a change of only 1%. Figure 17 shows this root locus. Since the 10 mode velocity root locus did not significantly deviate from the 4 mode velocity root locus, the four-mode analyses used for the gain-parameter root loci are considered to be valid, and the sensitivity of the calculations to the basis size is small, at least for Case 1.

#### Velocity Sensing

The second kind of sensor investigated measures vertical velocities rather than displacements. The same feedback loops, types of gain, flap configurations, and sensor configurations are used with the velocity sensors as are used with the displacement sensors. A similar set of gain-parameter root loci is calculated in search of the best velocity-sensing feedback loops.

Depending on the sign of the gain amplifier, two basic root-loci patterns emerge for velocity sensing in Case 1. These patterns are illustrated in Figures 18 and 19. Using positive feedback, Figure 18 shows the divergence critical root of mode 1 combining with the control (or actuator) root. For even small values of positive gain, this combination becomes unstable. Some loss of stability in mode 2 is also noted. Figure 19 indicates that negative feedback causes the control root to combine with the most stable root of the mode 1 pair after they reach the real axis. The other root of the mode 1 pair that is close to the imaginary axis (divergence critical) shows little movement with changes in gain setting.

Neither positive nor negative feedback of the velocity sensors changes the critical divergence speed, no matter what gains are used. However, the

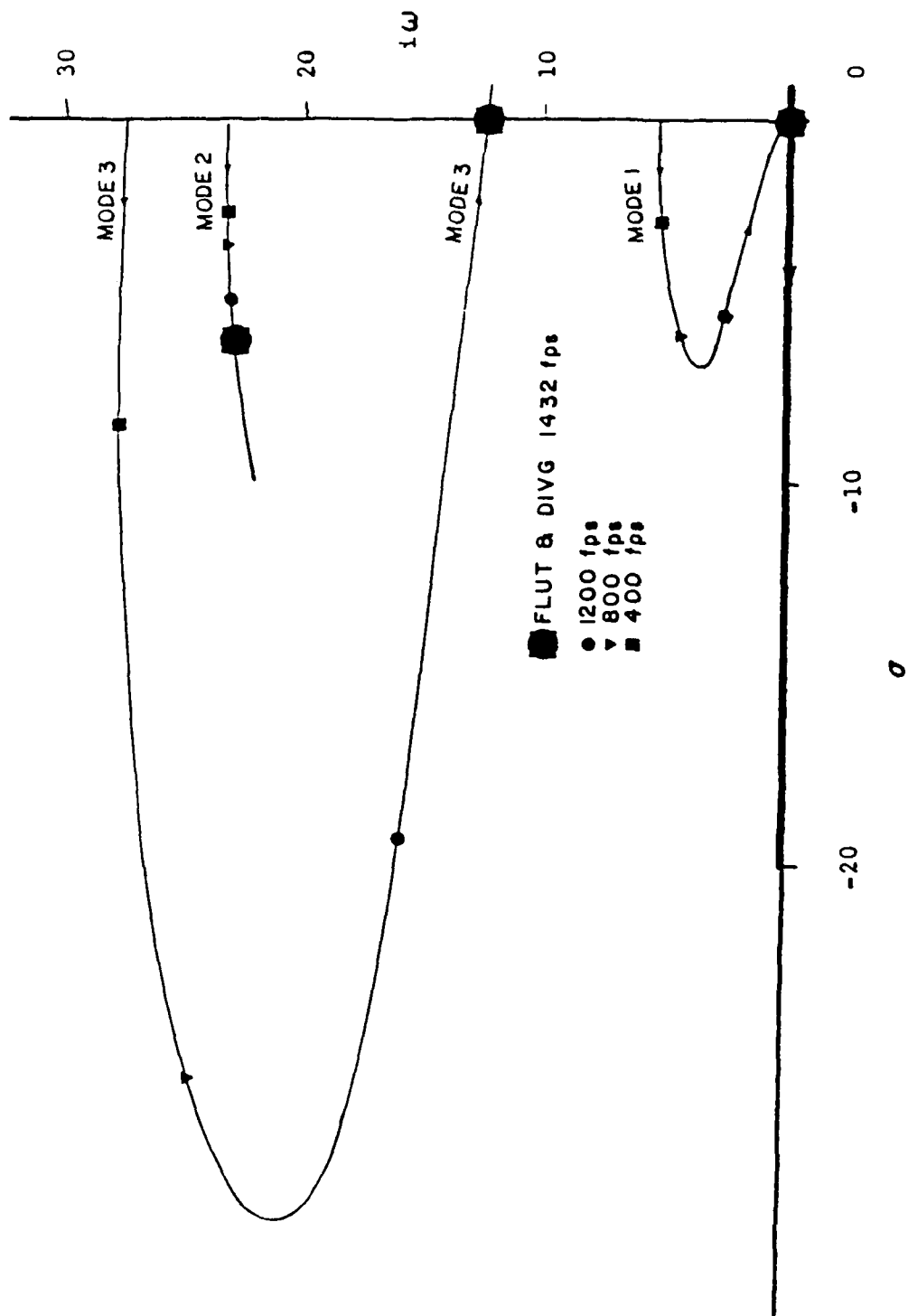


Figure 17 Velocity Root Locus For Case 1  
Sensor D/Flap B  $K_d = -6 \text{ rad/ft}$   
10 Mode Basis



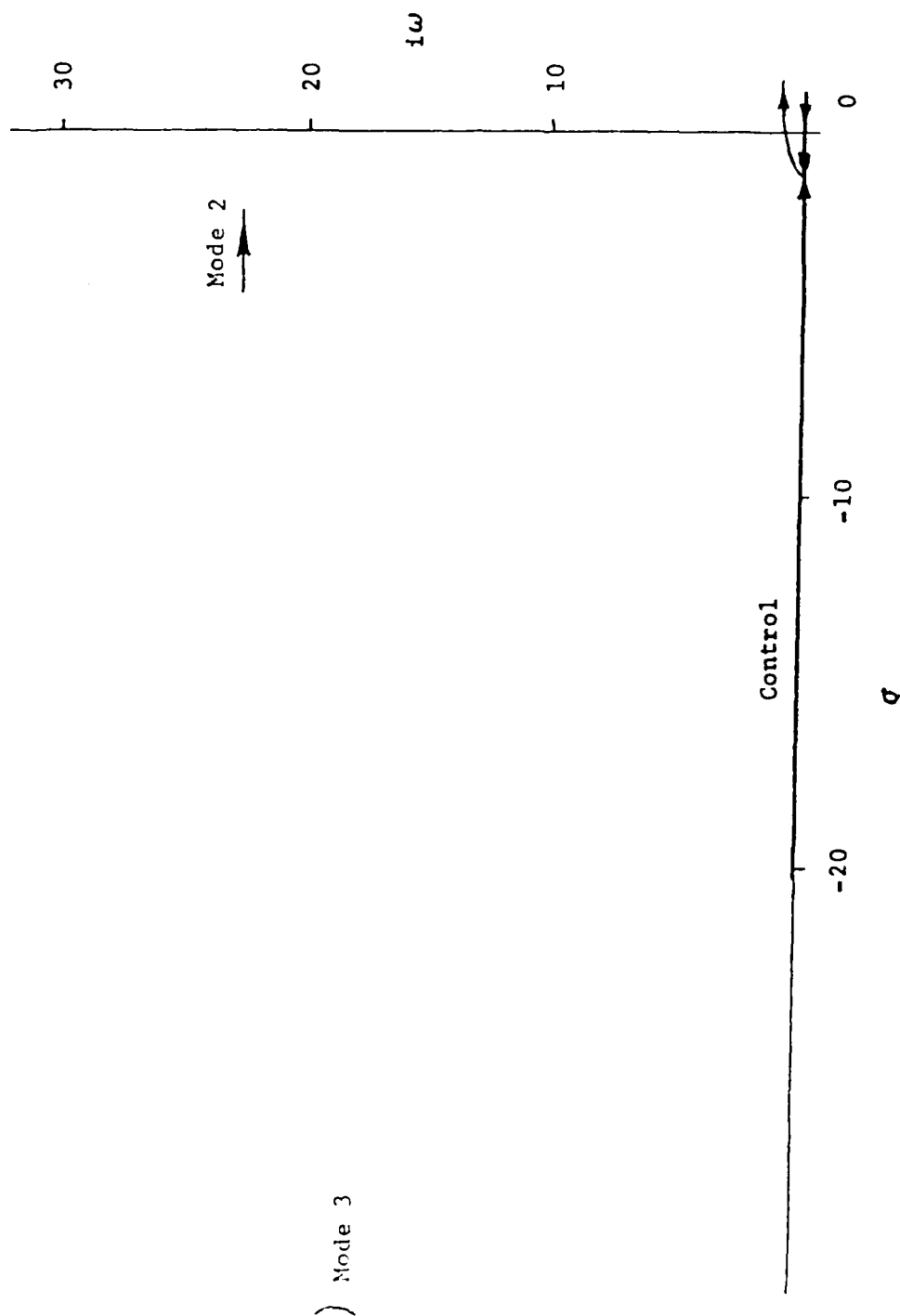


Figure 18 Gain-Parameter Root Locus For Case 1  
Sensor D/Flap A Positive Feedback  
Velocity Sensing

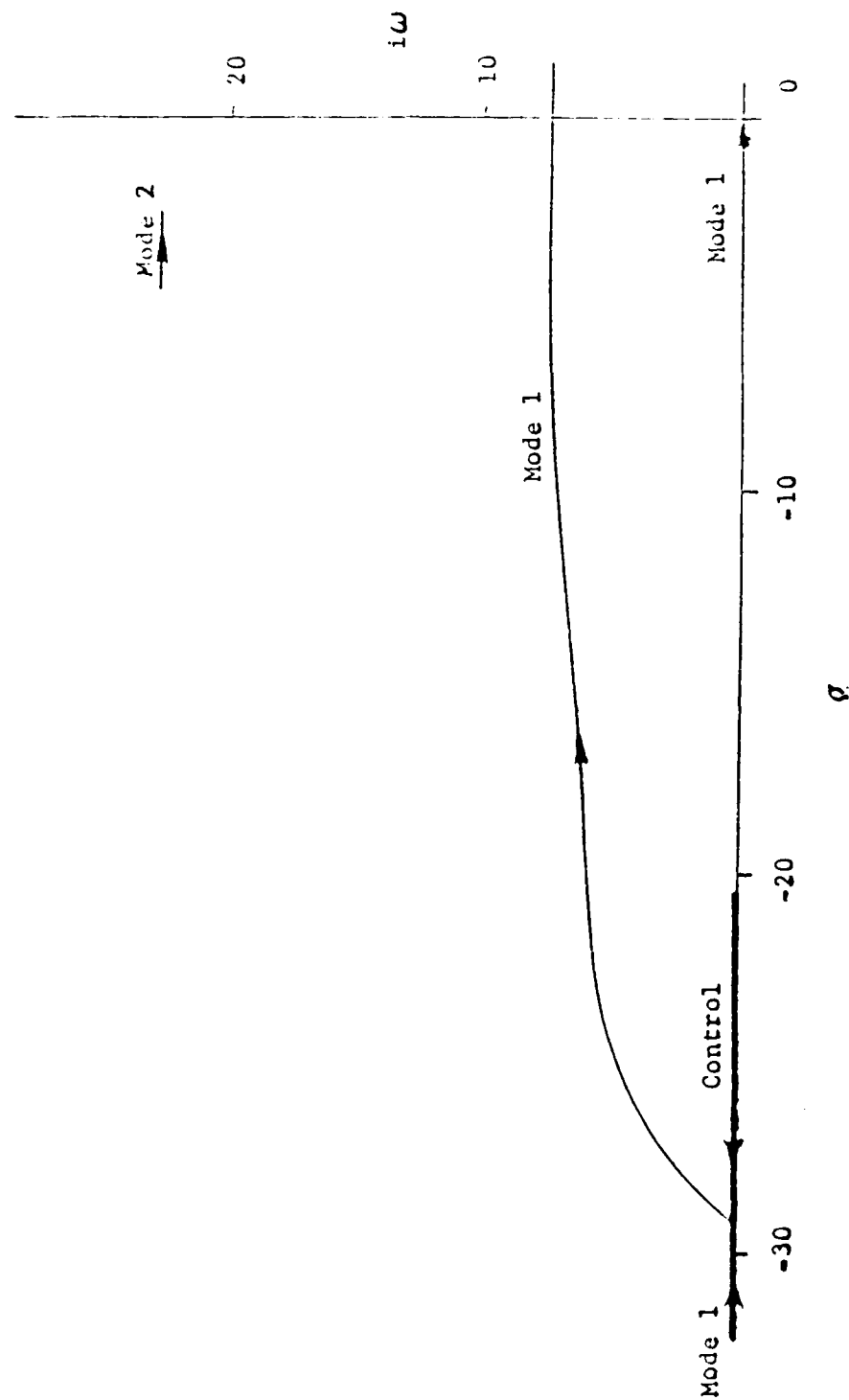


Figure 19 Gain-Parameter Root Locus For Case 1  
Sensor D/Flap A Negative Feedback  
Velocity Sensing

flutter speed can be increased or decreased considerably using velocity feedback. Examples of these changes can be seen in Figures 20 and 21. In Figure 20, a positive gain of .4 rad sec/ft increases the flutter speed to 1660 ft/sec, but divergence is still at 1160 ft/sec. In Figure 21, the gain is increased further to 2.6 rad sec/ft. In this case, mode 1 now defines flutter at only 661 ft/sec. The airspeed, corresponding to a root crossing of the imaginary axis on the real axis, is still 1160 ft/sec. This airspeed is the same speed as  $U_d$  for the uncompensated wing, but the axis crossing is now from negative damping to positive damping.

### Acceleration Sensing

Using the cantilever wing, the third kind of sensor measures accelerations at the sensor locations. The same combinations of flap, gain, and sensor location are used for accelerations as those used for the displacement and velocity calculations. When acceleration sensors are used (as with the velocity sensors), little effect is seen on the critical divergence condition. There is some effect, however, on the critical flutter airspeed.

Using the Sensor A/Flap B configuration, Figures 22 and 23 demonstrate acceleration sensing's lack of effect on divergence. In Figure 22, the parameter-gain root locus of Sensor A/Flap B show the actuator root combining with the most stable of the mode 1 roots. These roots then go unstable as conjugate pairs. When the gain is increased further, this conjugate pair breaks in on the real axis on the positive side. One of the pair then moves back towards the original divergence-critical mode 1 root that has not moved with gain change. In this same plot, the higher modes of the Sensor A/Flap B configuration lose stability. Figure 23 shows the velocity root loci of Sensor A/Flap B when acceleration sensing is used in the feedback loop. Even though the sub-critical response of all the modes has changed and the flutter speed has been significantly lowered, the mode 1 divergence condition still occurs at 1160 ft/sec.

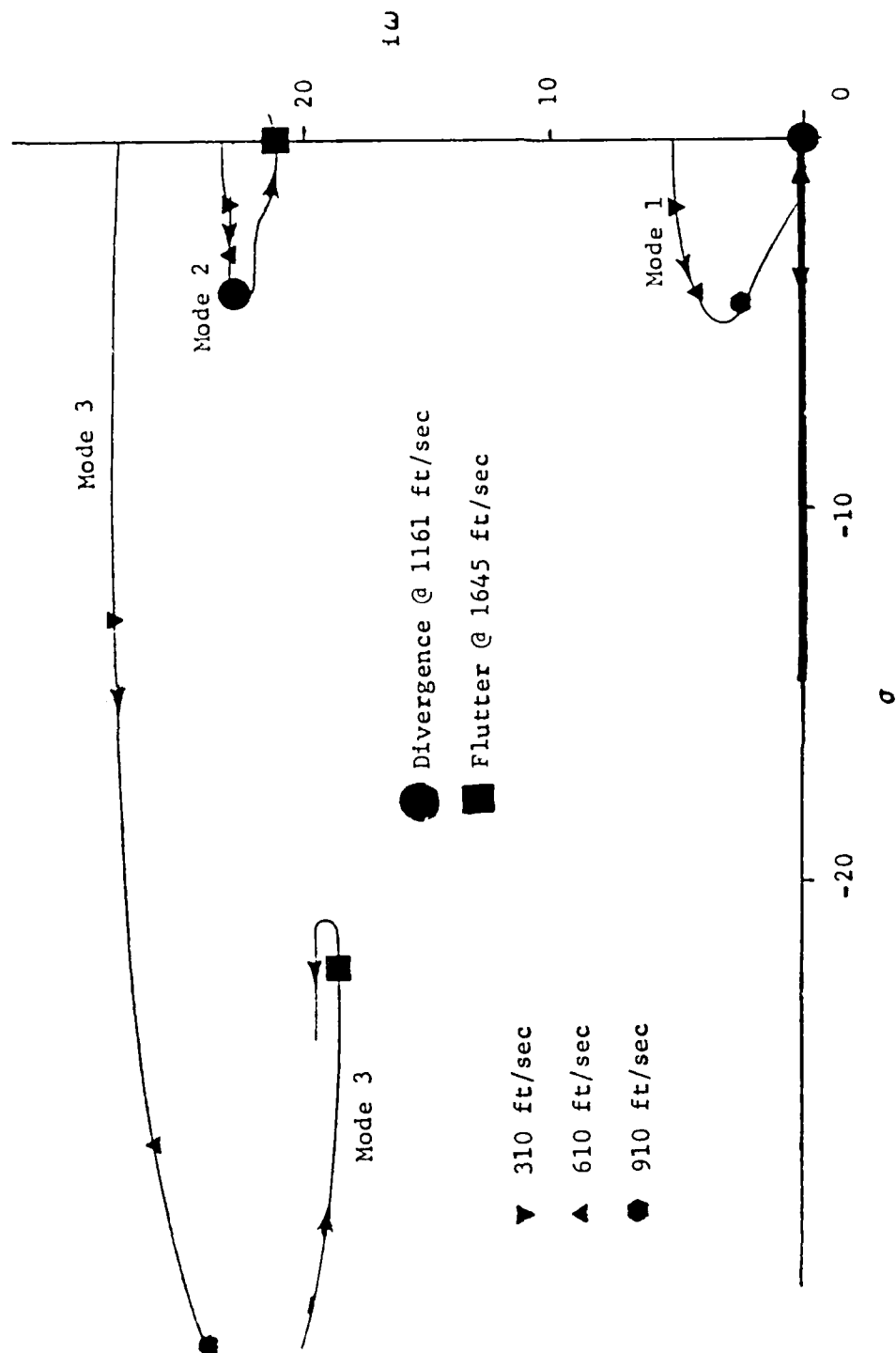


Figure 20 Velocity Root Locus For Case 1  
Sensor D/Flap D  $K_v = .4$  rad sec/ft

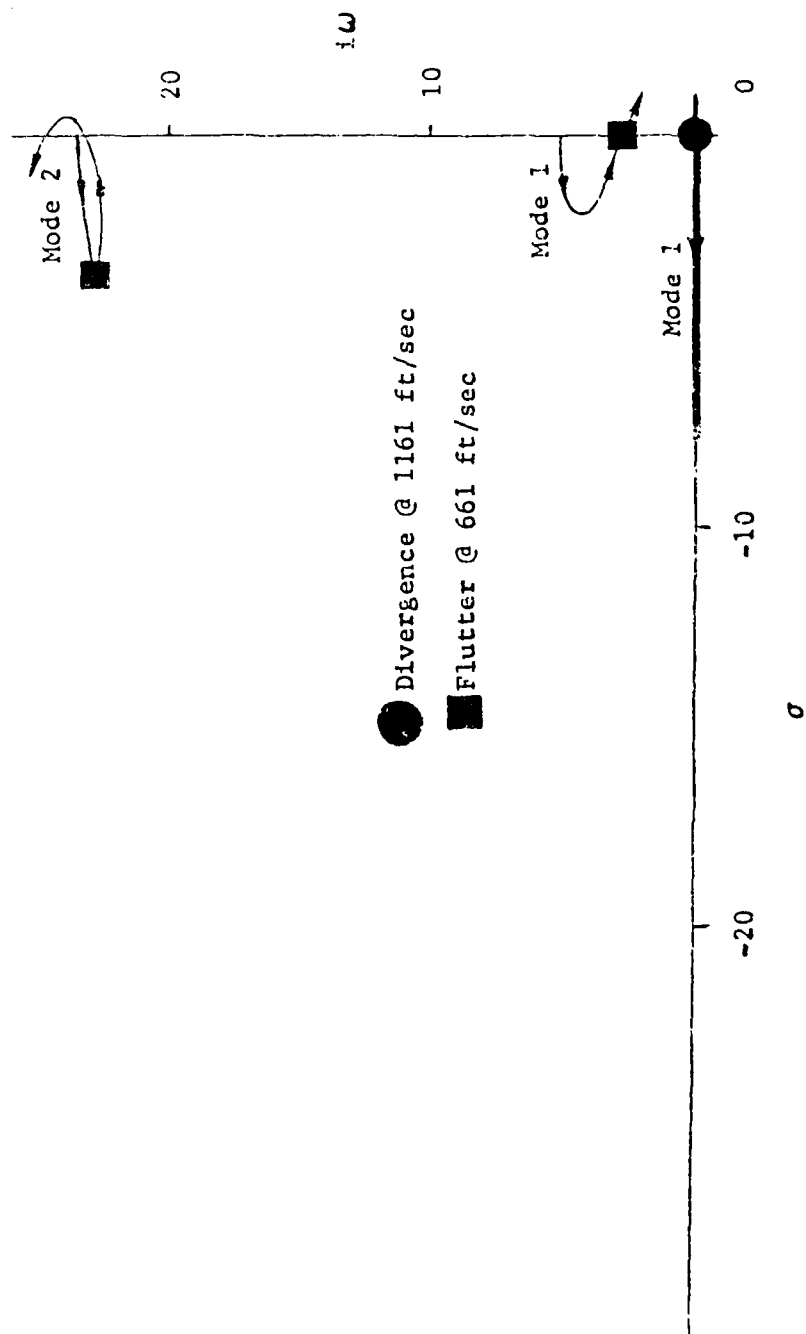


Figure 21 Velocity Root Locus For Case 1  
Sensor D/Flap D  $K_y = 2.6 \text{ rad sec/ft}$

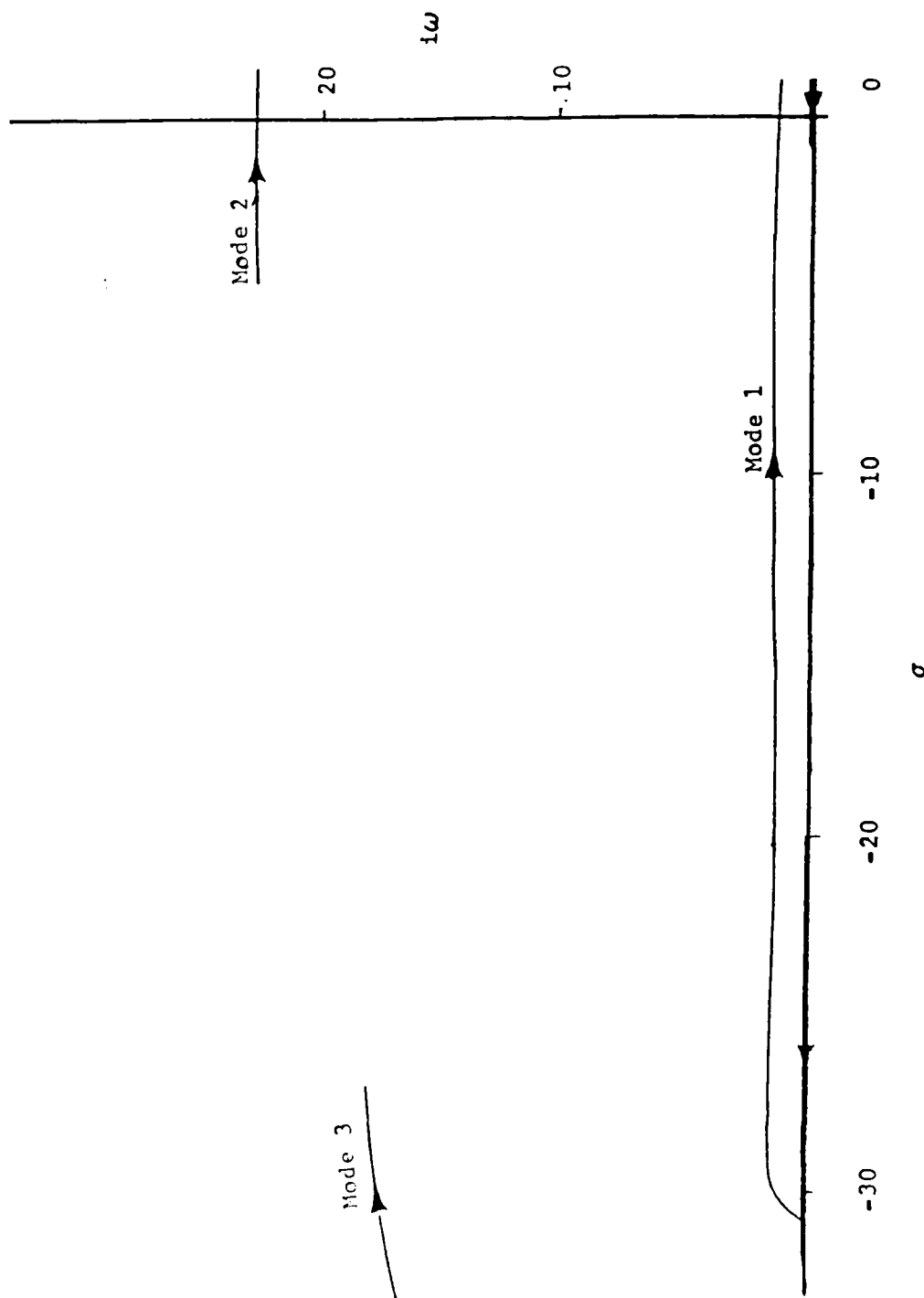


Figure 22 Gain-Parameter Root Locus For Case 1  
Sensor A/Flap B Positive Feedback  
Acceleration Sensing

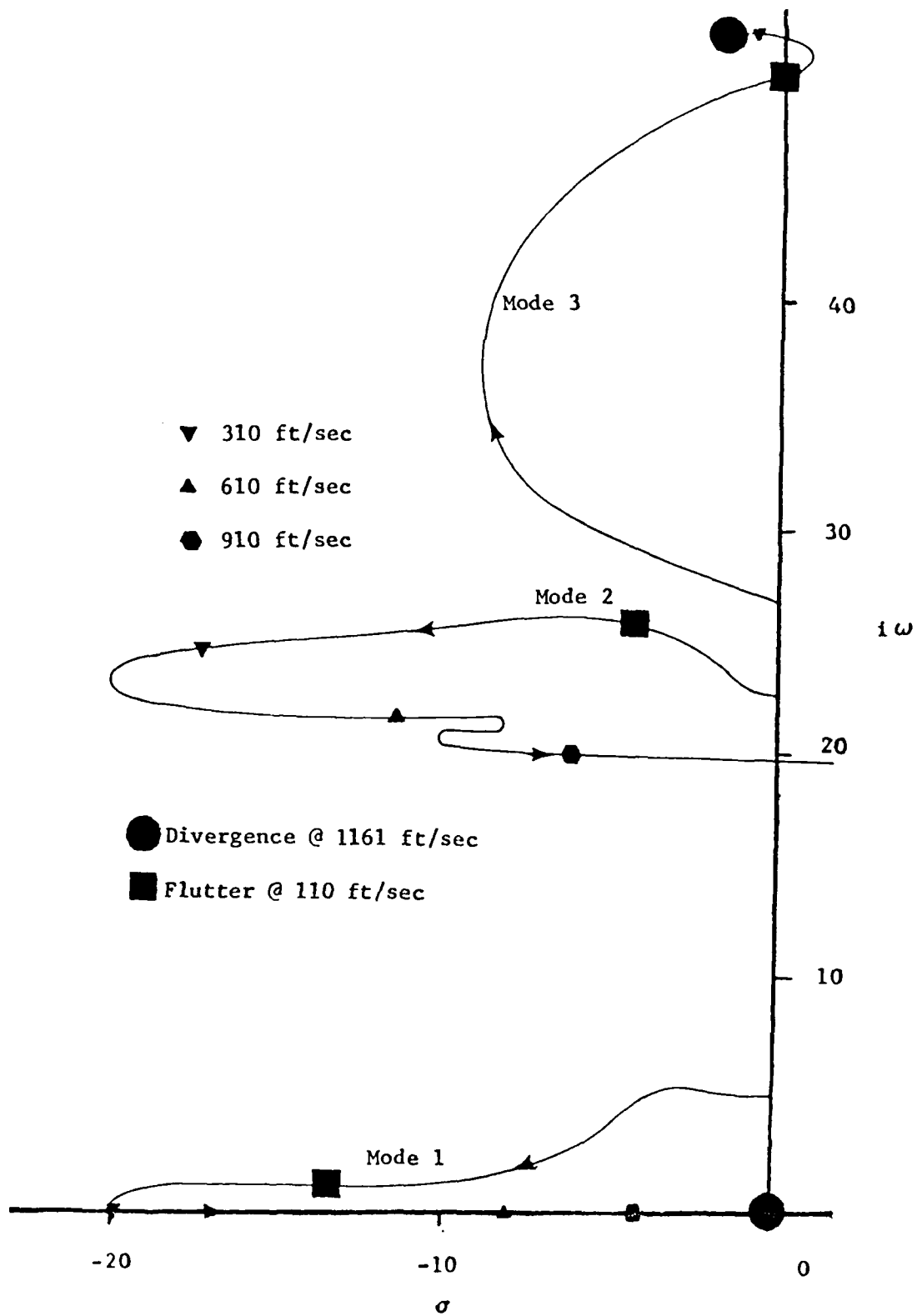


Figure 23 Velocity Root Locus For Case 1  
Sensor A/Flap B  $K_a = .245 \text{ rad sec}^2/\text{ft}$

### Summary of Case 1 Results

The results of the application of feedback control to this divergence-critical wing example are summarized as follows. To increase the airspeed at which aeroelastic divergence occurs, the use of velocity or acceleration sensing is unsuccessful. Only elastic-displacement sensing with negative feedback produces a significant increase in the divergence airspeed. The use of any of the three kinds of sensors changes the loci (and thus the subcritical response) of all roots. The velocity and root participation of the most critical flutter instabilities are also affected. The feedback-control configuration that most improved divergence also significantly lowered the critical flutter velocity.

The most success in suppressing divergence occurs when the roots defining divergence can be modified to increase the critical airspeed for divergence until that airspeed just reaches the value of the most critical secondary aeroelastic instability of flutter. The feedback configuration that improves Case 1 the most is the combination of Flap B and Sensor D. This flap and sensor combination (with negative feedback) suggested that the mechanism most effective in improving divergence is a reduction in the apparent lift-curve slope of the outboard section of the wing. The location and relative signal signs of the sensors for the Sensor D configuration provide feedback signals that emphasize movements corresponding to increases in the section's angle-of-attack. Movement of Flap B tends to change the apparent angle-of-attack of the outboard wing sections. When negative feedback is used, the flap tends to lower the local angle-of-attack as the wing box section increases in angle-of-attack. The control effect on the wing's capability to produce lift can be summarized as a reduction in the apparent lift-curve slope of the outboard portion of the wing. This trend in lift-curve slope also agrees with those found in simple airfoil examples (Ref. 2).

### Case 2 Study

For the example wing in Case 2,  $U_f$  is lower than  $U_d$ . The external geometry for Case 2 is the same as that used in Case 1, but the structural



wing box has been tailored to make  $U_f$  lower than  $U_d$ , providing a contrasting example to that of Case 1. Mode 1 is the first wing-bending mode, with a frequency of 5.09 rad/sec. Mode 2 is the first torsional mode, with a frequency of 19.75 rad/sec. Mode 3 is the second bending mode at 25.32 rad/sec. Mode 4 is the second torsion mode at 47.75 rad/sec. For reference, recall that the first torsion mode of Case 1 is mode 3 (rather than mode 2 for Case 2). Also mode 3 of Case 1 has a higher vacuum vibration frequency than that found in mode 2 of Case 2. These differences in their torsion modes correspond to the lower  $U_f$  found in Case 2 versus Case 1.

At the aeroelastic instabilities for Case 2, the velocities are shown in the velocity root locus of Figure 24. In this root locus, a flutter instability is predicted from the crossing of the imaginary axis by mode 2 at a freestream airspeed of 960 ft/sec. The divergence condition is again predicted by the mode 1 crossing (with no imaginary part) at a velocity of 1281 ft/sec. Note that the mode 1 break-in point is much more negative than that found in Case 1 and occurs to the left of the visible range of the negative real axis shown in Figure 24. Mode 3 also shows some loss of damping when the velocities reach the higher values. The other modes merely gain damping with airspeed.

#### Displacement Sensing

The sixteen combinations of sensor and flap are again used to examine displacement sensing. The airspeed used for gain-parameter root loci is 960 ft/sec, except for some specifically noted examples. Based on the effect in the divergence speed of Case 1, positive gain is not examined for Case 2 when using displacement sensing. Therefore, only negative-feedback examples are discussed for Case 2 when displacement sensing is used.

Negative gain applied to displacement sensing of Case 2 provides three basic shapes for the gain-parameter root loci calculated. In the first form, mode 2 and the control root go unstable. The second form differs from the first in that the mode 1 and mode 2 roots go unstable while the

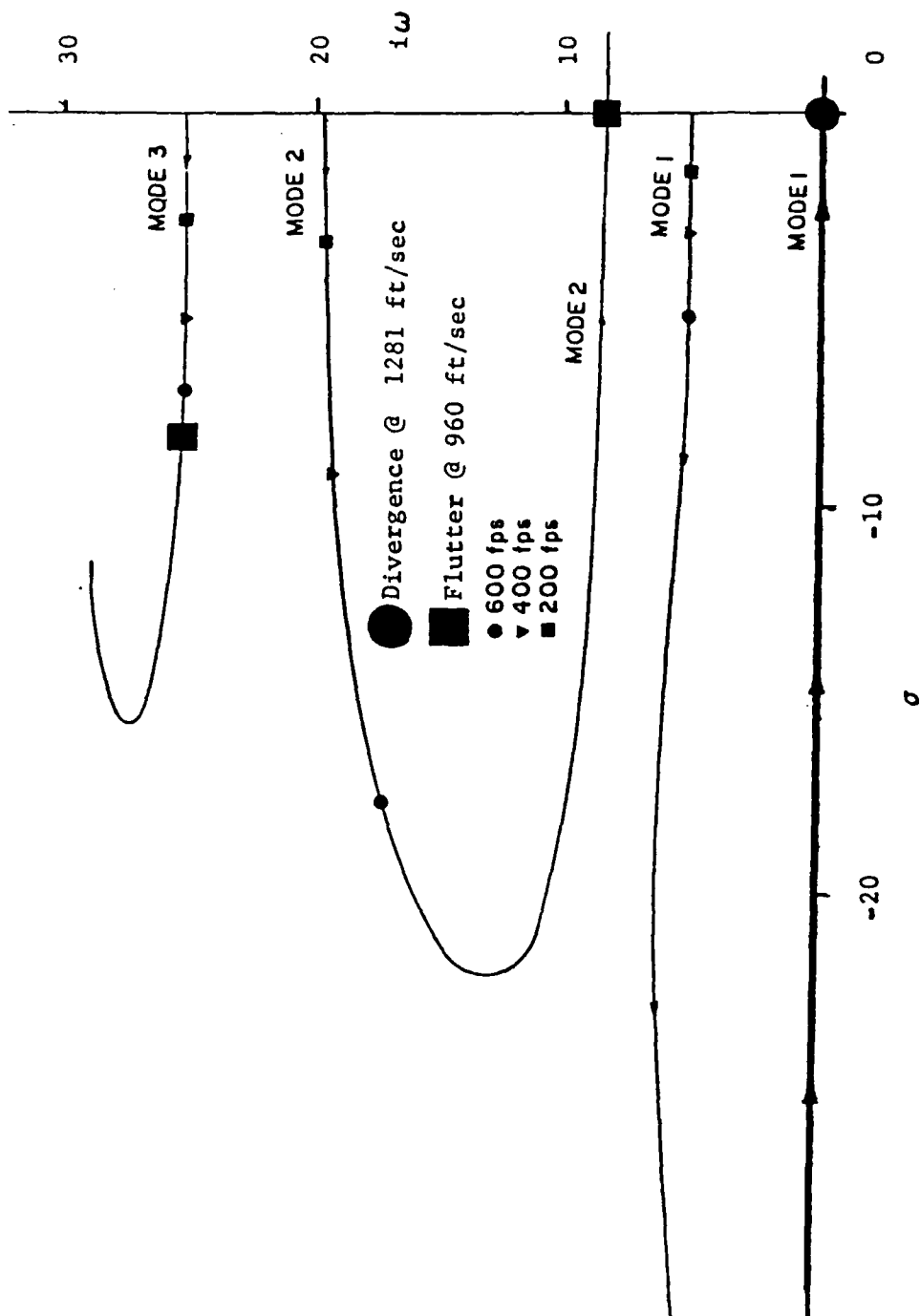


Figure 24 Velocity Root Locus For Case 2  
No Feedback

control root gains stability. In the third form, mode 2 increases in stability while the control root loses stability.

In Figure 25, the second form in gain-parameter root loci is exhibited. The feedback configuration uses the Sensor A/Flap B combination. Velocity root loci are calculated using two significantly different gain values with this flap and sensor configuration. With a small gain value of  $-.05$  rad/ft, the velocity root loci of Figure 26 show only slight improvements in the flutter- and divergence-critical velocities. When the gain is changed to  $-15.55$  rad/ft, a considerable improvement is made in the divergence-critical roots of mode 1. This velocity root loci is plotted in Figure 27. However, flutter now occurs at a much lower velocity,  $610$  ft/sec, and is defined by roots of mode 1 rather than of mode 2. With this feedback loop, the divergence instability is not indicated. In Figure 28, the possibility of a useful intermediate value of gain is examined for the Sensor A/Flap B configuration, a gain of  $-1$  rad/ft. The flutter-critical mode 2 roots remain essentially unchanged, but the divergence condition from the mode 1 roots never materializes. The mode 1 roots remain oscillatory and gain damping.

It should be noted that another approach can be employed when using gain-parameter root loci to define gain values and desirable sensor/flap combinations. The root loci can be calculated at freestream flow velocities higher than the lowest critical velocity. A single example of this approach for the Case 2 wing is shown in Figure 29. The freestream velocity is  $1160$  ft/sec for this gain root loci. Therefore, the roots of mode 2 (which crossed the imaginary axis at  $960$  ft/sec) are well into the negative damping region of the complex plane. These root loci for the Sensor D/Flap A configuration suggest it is capable of moving the mode 2 flutter roots back into the positive-damping region. However, when the velocity root loci are calculated using this control law the control root becomes unstable before these flutter roots become stable. In general, using a flow velocity that is higher than the most critical flow velocity (when calculating a gain-parameter root locus) was not useful. This lack

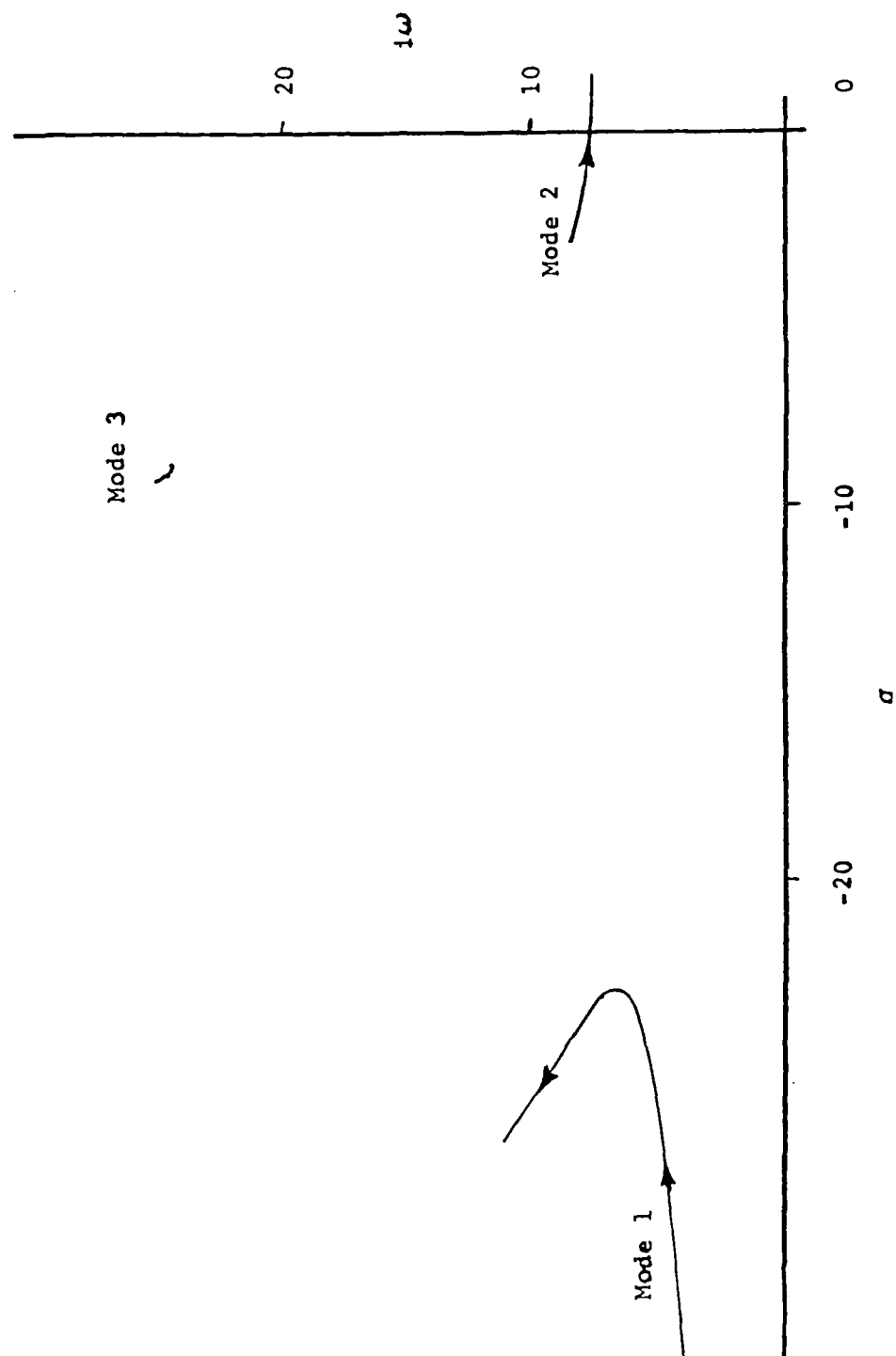


Figure 25 Gain-Parameter Root Locus For Case 2  
Sensor A/Flap B Negative Feedback  
Displacement Sensing

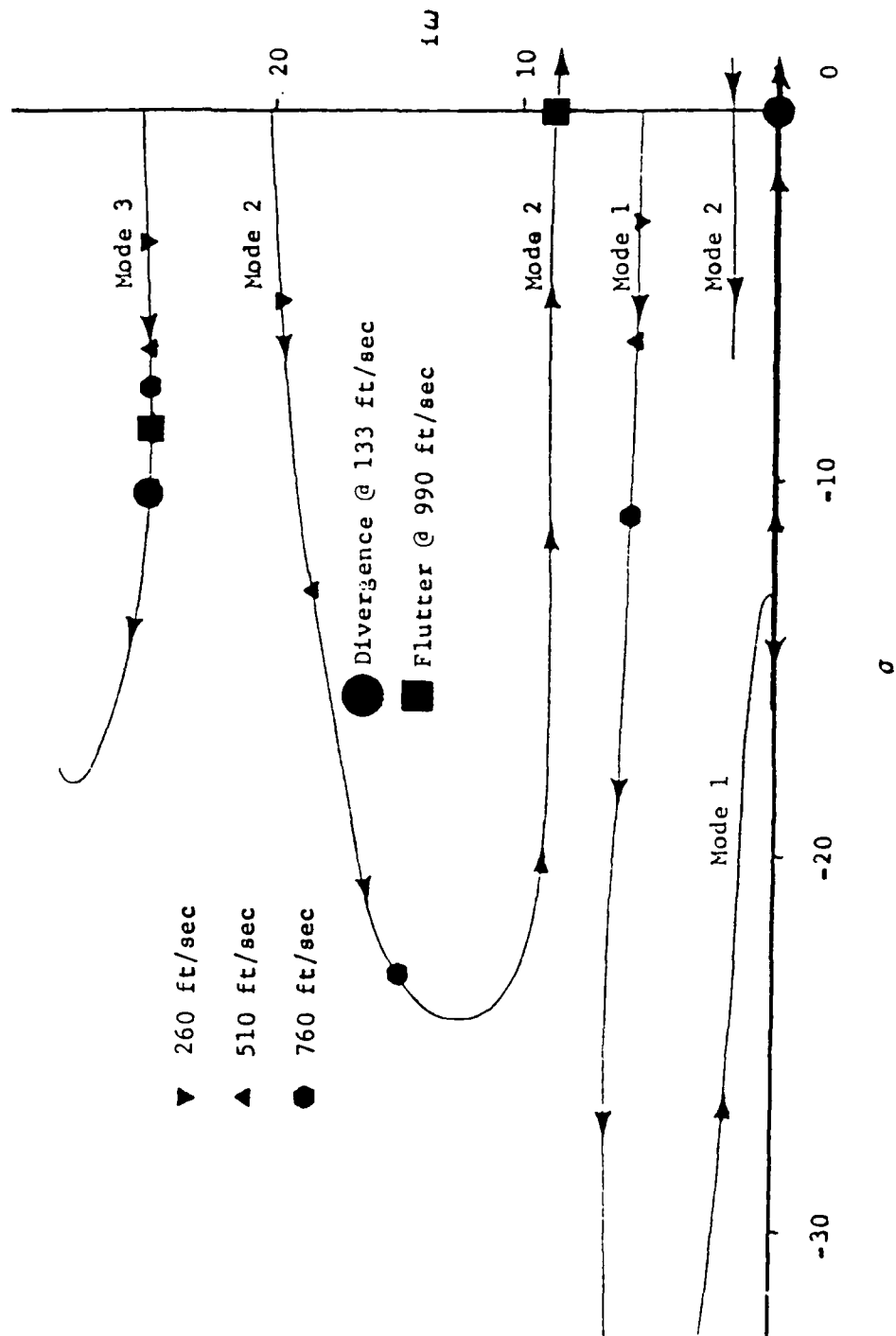


Figure 26 Velocity Root Locus For Case 2  
Sensor A/Flap B  $K_d = -.05 \text{ rad/ft}$

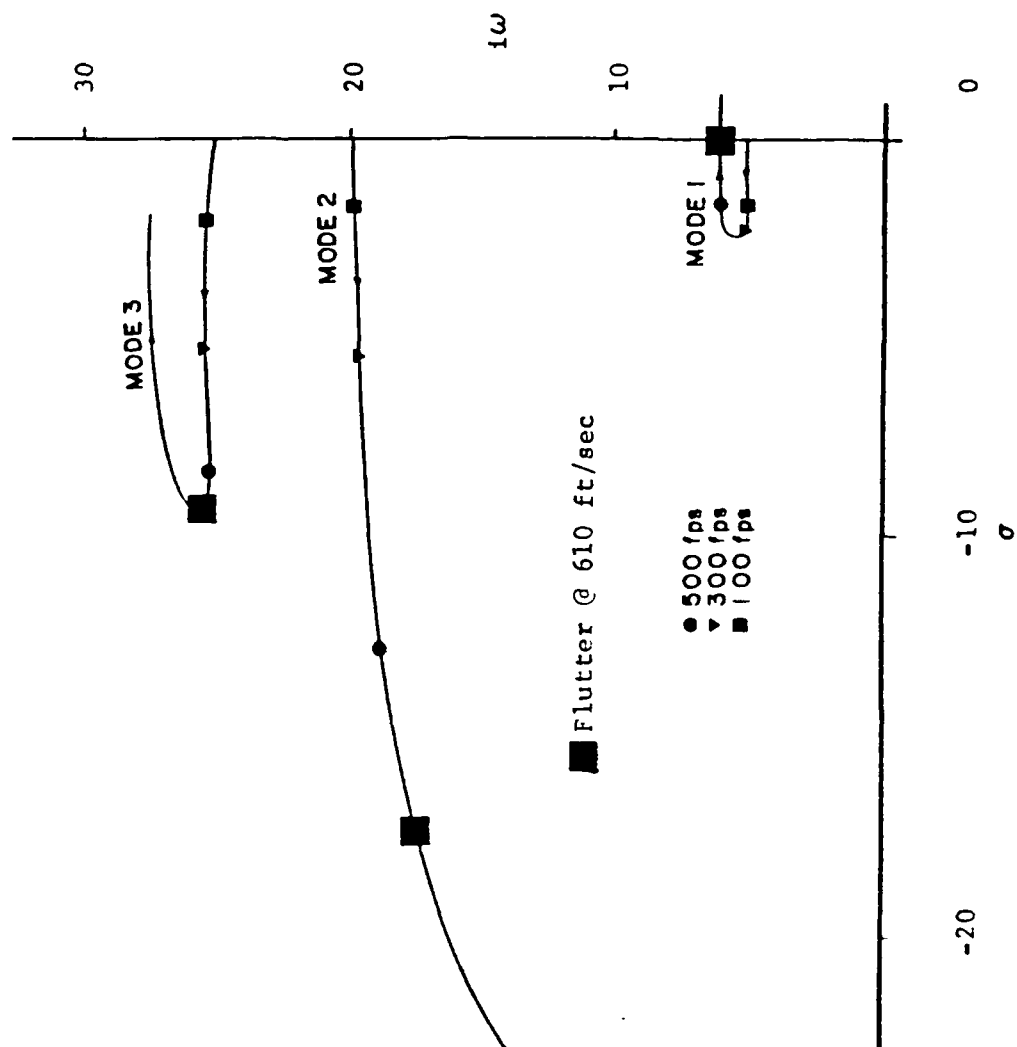


Figure 27 Velocity Root Locus For Case 2  
 Sensor A/Flap B  $K_d = -15.55 \text{ rad/ft}$

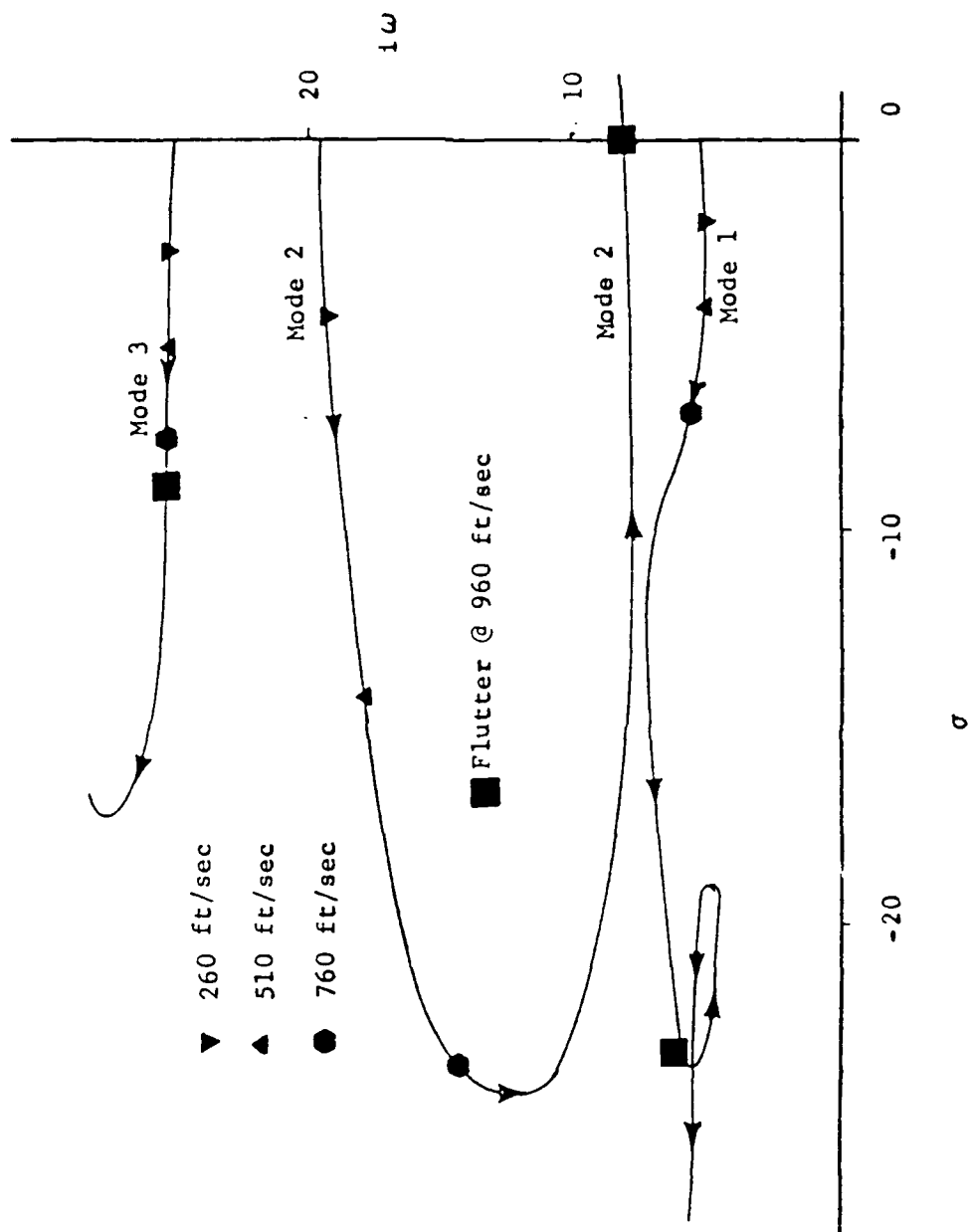


Figure 28 Velocity Root Locus For Case 2  
Sensor A/Flap B  $K_d = -1$  rad/ft

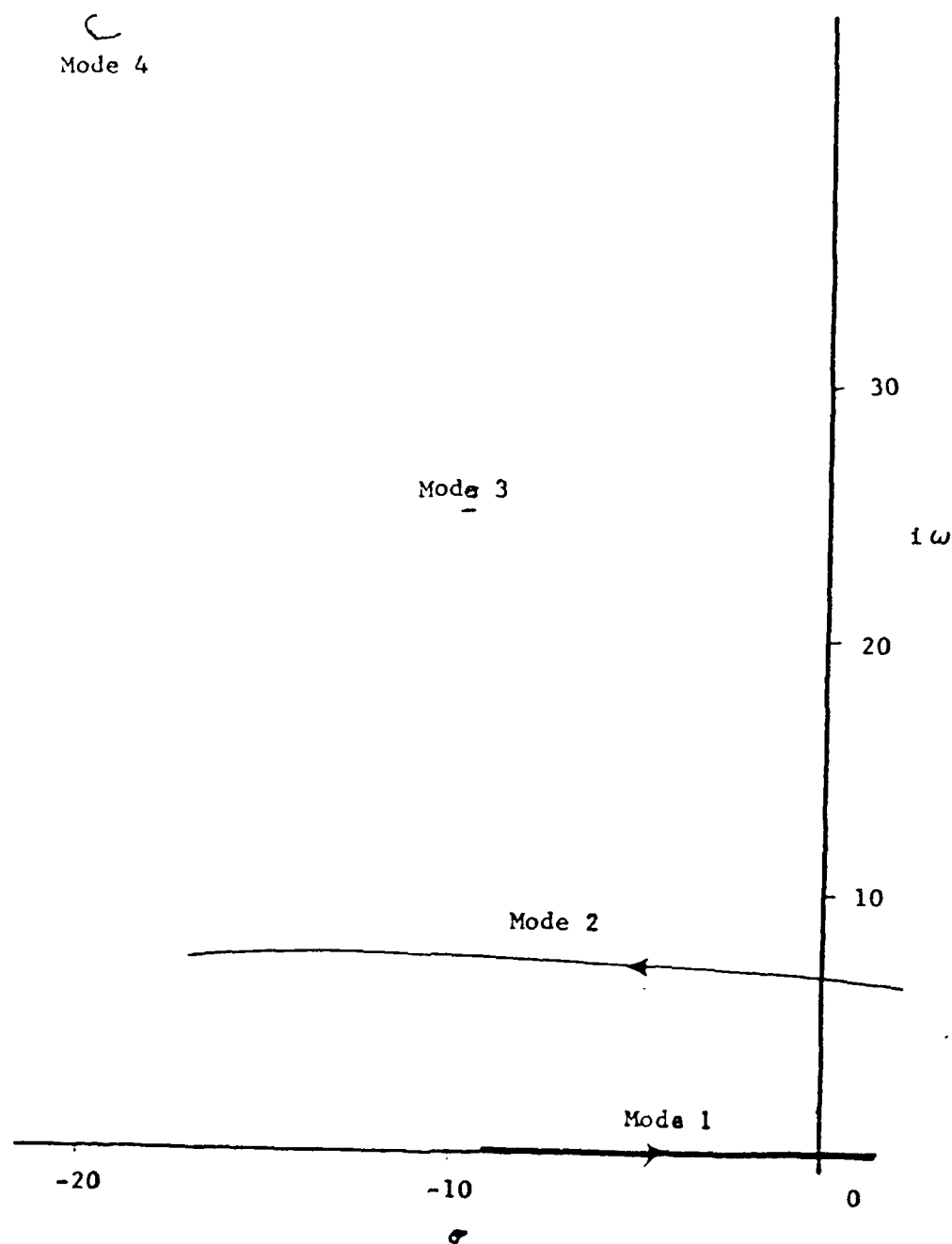


Figure 29 Gain-Parameter Root Locus For Case 2  
 Sensor D/Flap A Negative Feedback  
 Displacement Sensing  $U = 1160 \text{ ft/sec}$



of success results, in part, from the non-linear effect of velocity that is a consequence of the powers of the  $s$  parameters. Therefore all other gain-parameter root loci shown for Case 2 are calculated using a freestream airspeed of 960 ft/sec.

For Case 2, no feedback-control loop using displacement sensing improves the most critical aeroelastic instability to a useful degree. As in Case 1, displacement sensing affects divergence but is not helpful in improving flutter.

#### Velocity Sensing

For the Case 2 wing, velocity sensing is examined for both positive and negative feedback. All gain-parameter root loci are calculated using a freestream flow velocity of 960 ft/sec, with several patterns of root loci emerging. These patterns generally show that negative feedback improves the stability of the actuator root, while positive feedback does not.

Typical of the first pattern is the rapid decrease in stability of the roots of mode 1, while the control root moves in a stable direction. In a second pattern (with negative feedback), the mode 2 root becomes unstable at low negative gain values. Mode 1 shows some loss of stability in this second pattern, but does remain stable. The control root also remains stable. The third pattern is similar to the second pattern except that positive feedback moves the control root toward instability. Pattern four provides improved stabilities for the mode 2 roots, but causes both the mode 1 roots and the control root to lose stability. The loss of stability by the control root, however, is gradual. Significant improvements in the stability of the mode 2 roots is possible before the control root goes unstable. A good example of this last pattern is shown in Figure 30. Here the gain-parameter root locus of the Sensor D/Flap D configuration suggest that a positive gain of .15 rad sec/ft can be useful. At this gain setting, about equal trades can be made in stability of the roots of mode 1 and mode 2. For aeroelastic instabilities, this gain setting would allow a similar trade in airspeeds to that made in the Case 1 divergence solution.

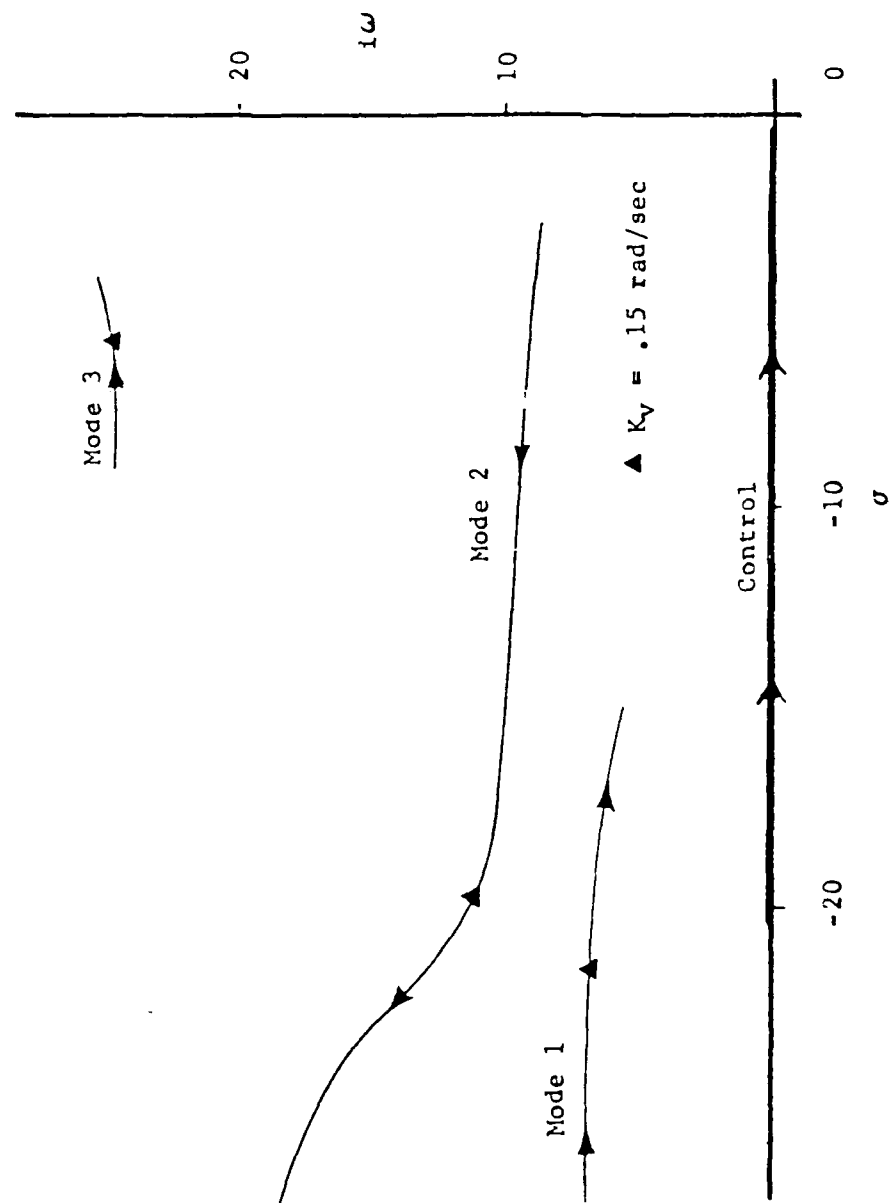


Figure 30 Gain-Parameter Root Locus For Case 2  
Sensor D/Flap D Positive Feedback  
Velocity Sensing

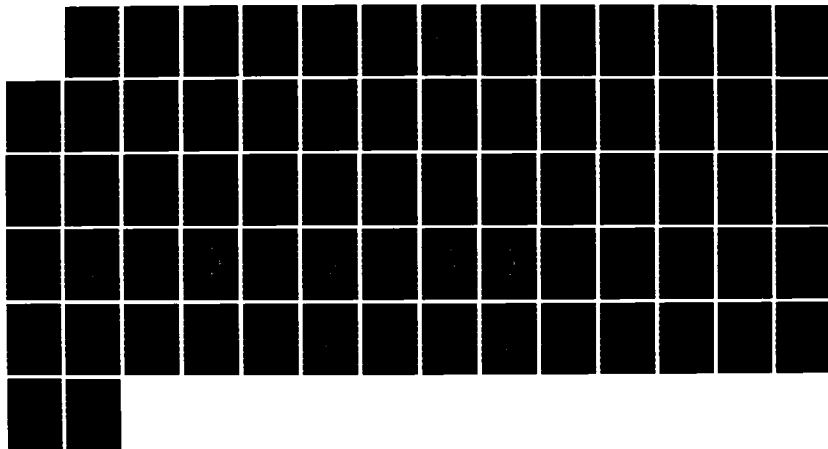
AD-A168 373

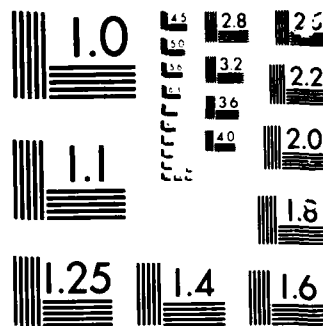
ACTIVE CONTROL OF FORWARD SWEPT WINGS WITH DIVERGENCE  
AND FLUTTER AEROELA. (U) AIR FORCE INST OF TECH  
WRIGHT-PATTERSON AFB OH SCHOOL OF ENGI.. K E GRIFFIN  
01 MAY 84 AFIT/DS/AA/84-1 F/G 20/4

2/2

UNCLASSIFIED

NL





MICROCOPY

CHART

Using a gain of  $.15 \text{ rad sec/ft}$ , a velocity root locus for Sensor D/Flap D is calculated in Figure 31. Note that while the flutter velocity moved from  $960 \text{ ft/sec}$  to  $1110 \text{ ft/sec}$  (at the expense of some loss in divergence airspeed), the improvement does not result in a significant improvement in flutter. This lack of significant improvement is typical of improvements available for the velocity-sensing feedback loops for Case 2, and, therefore, velocity sensing is not really useful for Case 2.

#### Acceleration Sensing

Acceleration sensing provides several useful feedback loops for stabilizing the roots of mode 2. In Figure 32, the gain-parameter root loci for Sensor D/Flap A are plotted. Here the negative feedback from the Sensor D combination is increased, and the roots of mode 2 move away from the imaginary axis toward increased stability. At the same time, the roots of modes 1 and 3 lose stability. With the gain set at  $-.05 \text{ rad sec}^2/\text{ft}$ , a velocity root locus (using Sensor D/Flap A) is calculated and presented in Figure 33. Note that while the roots of mode 2 come close to the imaginary axis, no crossing (and, therefore, flutter) occurs. The divergence instability still occurs at  $1280 \text{ ft/sec}$  and cannot be improved with any of the gain settings. This divergence airspeed then becomes the limit to the amount of improvement in airspeed possible with acceleration sensing in the Sensor D/Flap A combination.

Other feedback configurations offer possibilities for improving the flutter-critical roots of mode 2. Using Sensor D, positive gain can improve mode 2 when either Flaps C or D are employed. With negative gain, Sensor D can be coupled to Flap B. The gain sign change is required for Sensor D/Flap B because of the angle sense of the leading-edge flap deflection. These other flap and sensor combinations, however, do not give improvements in the divergence condition. Therefore, the maximum improvement to the most critical aeroelastic instability remains at the  $1280 \text{ ft/sec}$  level. This maximum value is defined by the unchanged airspeed of divergence and not by limitations on the effect possible of the flutter-critical mode 2 roots.

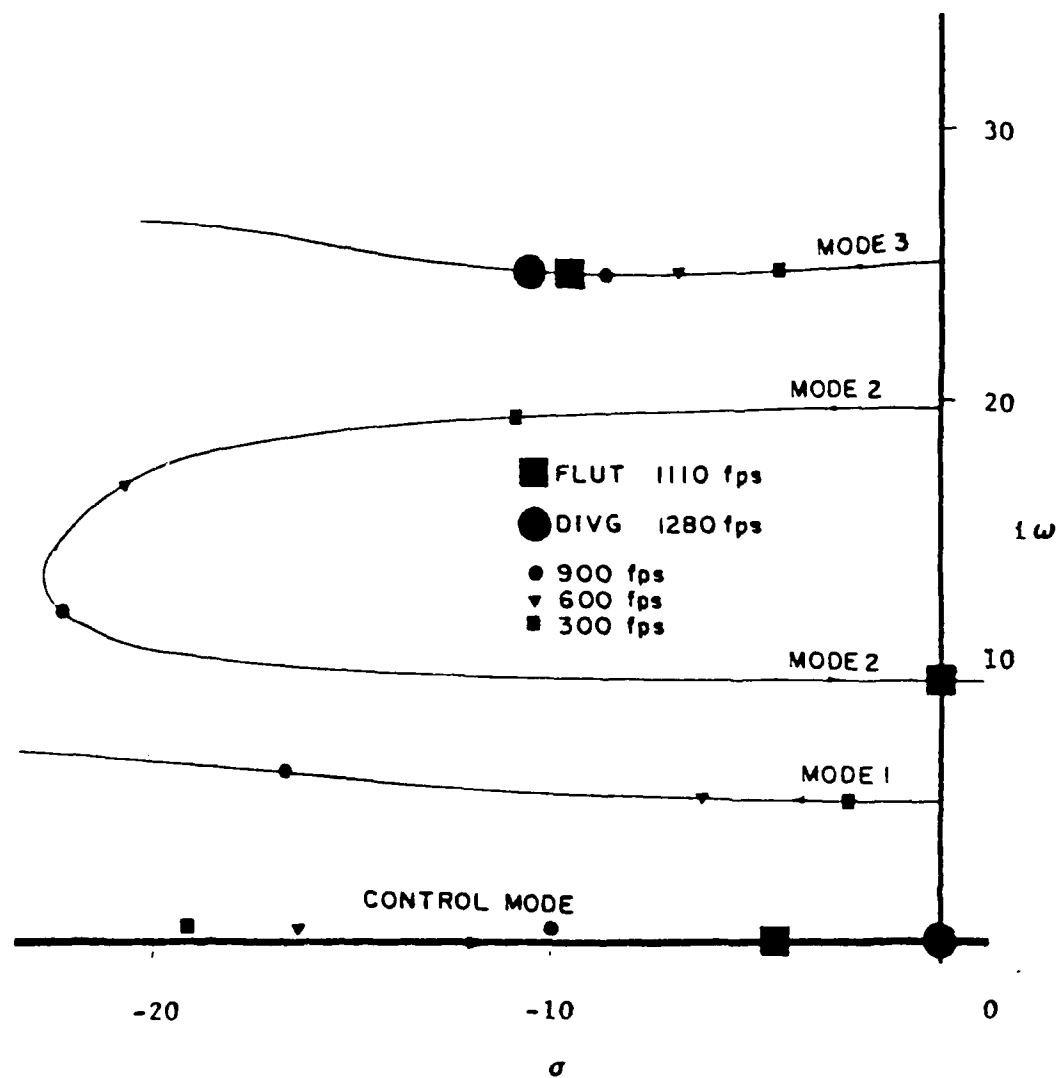


Figure 31 Velocity Root Locus For Case 2  
Sensor D/Flap D  $K_v = .15 \text{ rad sec/ft}$

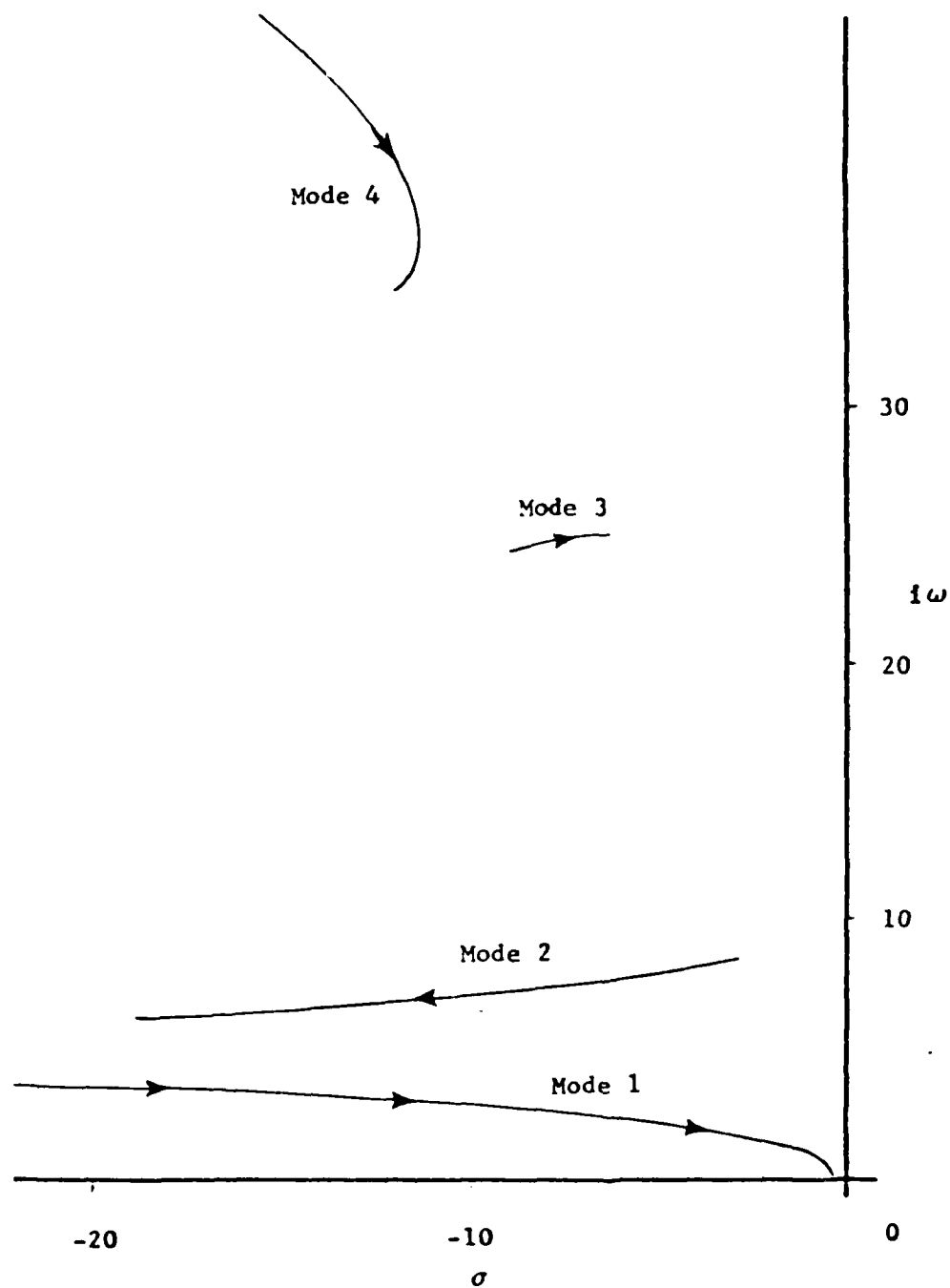


Figure 32 Gain-Parameter Root Locus For Case 2  
 Sensor D/Flap A Negative Feedback  
 Acceleration Sensing

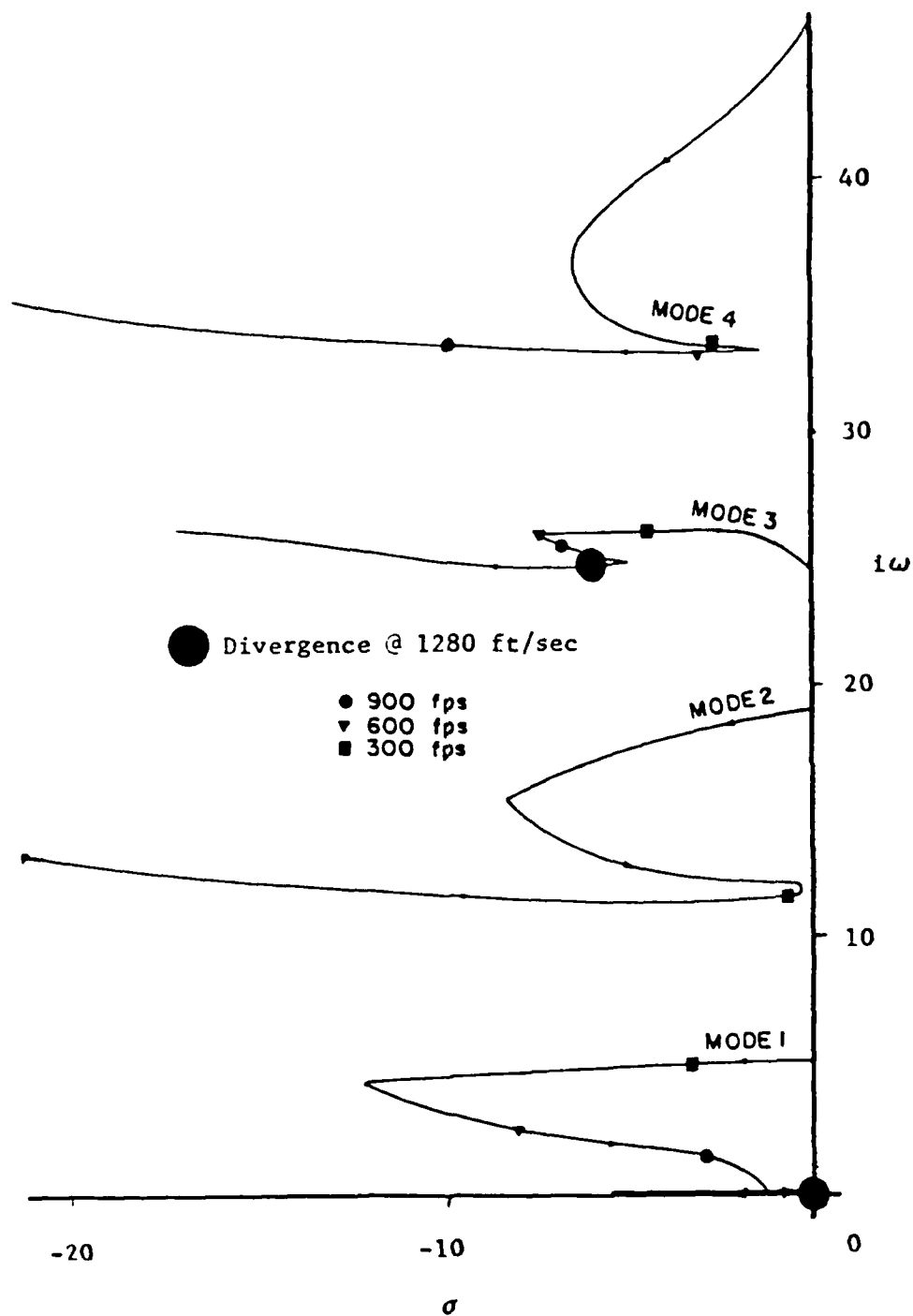


Figure 33 Velocity Root Locus For Case 2  
 Sensor D/Flap A  $K_a = -.05 \text{ rad sec}^2/\text{ft}$



This limitation on improvements for Case 2, resulting from a low-speed divergence condition, does not suggest similar limitations on wings with more conventional velocity spacing between flutter and divergence. The improvements in flutter for any wing design, however, must not be sensitive to small changes in the analysis. As a check on analysis sensitivity, changes are made in the number of vibration modes used as coordinates in the root loci calculations, and the Sensor D/Flap A configuration is re-calculated using a 10-mode basis. This re-calculation is presented in Figure 34. Note that unlike the calculations made with the 4-mode basis, the roots of mode 4 move far enough over to the imaginary axis to touch it. This condition indicates a potential problem for the feedback loop using Sensor D/Flap A. It appears a new low-speed flutter condition has been created using the feedback loop and involving mode 4.

The sensitivity problem just shown may be caused by two possibilities. First, as more modes are included in the basis for the calculations, the number of generalized forces increases, and the frequency range widens that must be spanned by the Padé Approximants. Since the polynomials do not change order, they must represent more information with the same number of terms. Secondly, in Case 2, mode 4 is the second torsion mode rather than another bending mode, as in Case 1. Modes with dominant torsional motion define flutter instabilities in all the root locus calculations. With two low-frequency modes capable of producing flutter, Case 2 has greater potential for creation of secondary flutter modes with active control.

#### Summary of Case 2 Results

Application of feedback control to Case 2 indicated that acceleration sensing is the most useful type of measurement for forward-swept wings that are flutter critical. The successful Sensor D configuration suggests that the pitch-angle acceleration of the outboard portion of the wing provides a useful signal for active control of flutter. Again, the limitation in improvement in velocity of the most critical aeroelastic instability (in this case, flutter) is the secondary instability (in this case, divergence). Fortunately, acceleration sensing does not affect divergence

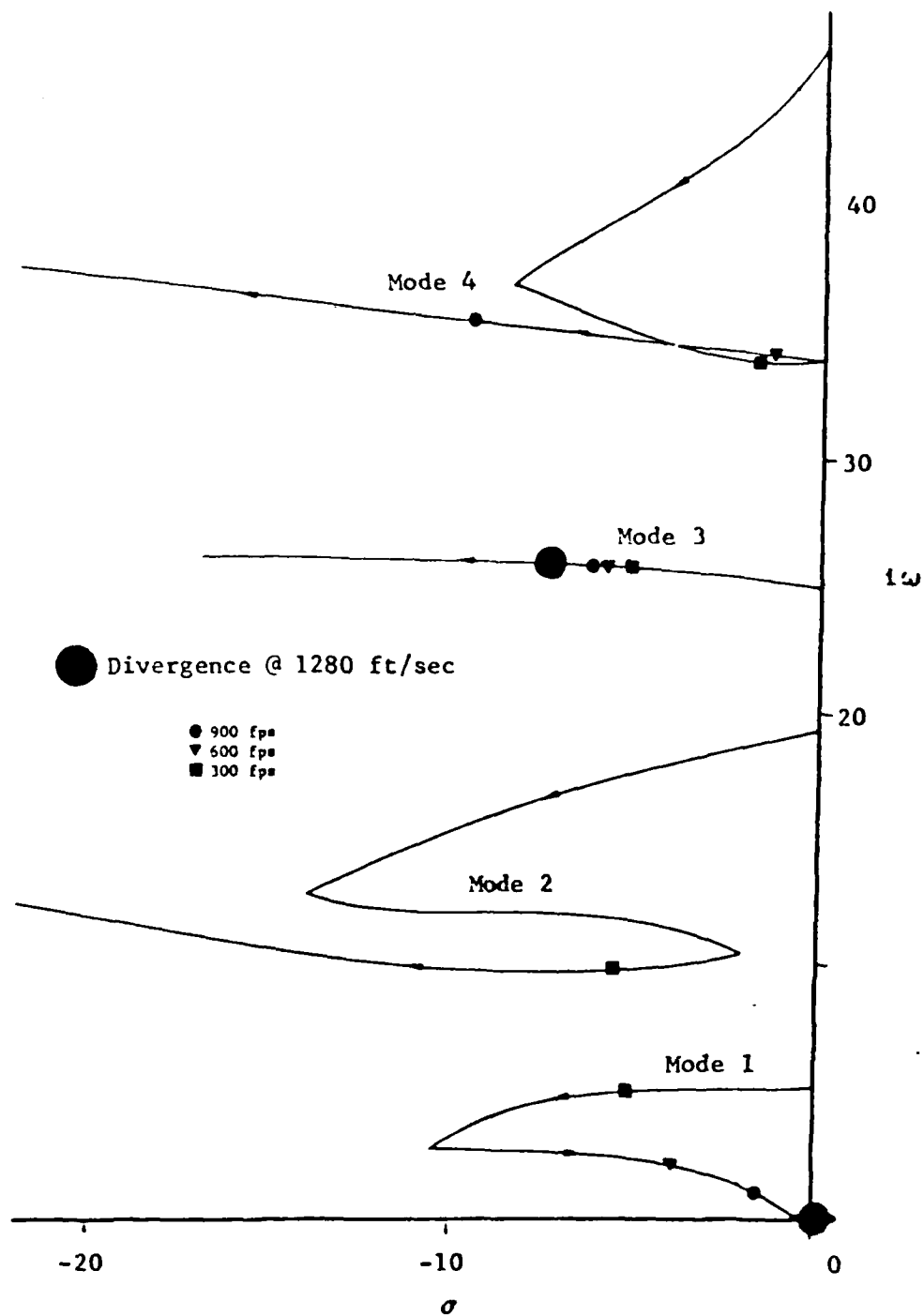


Figure 34 Velocity Root Locus For Case 2  
 Sensor D/Flap A  $K_a = -.05 \text{ rad sec}^2/\text{ft}$   
 10 Mode Basis

instabilities. Thus, the available improvement in overall stability for Case 2 is defined by how high  $U_d$  can be made in the uncompensated wing design.

The calculations of flutter critical wings also indicate that more care must be taken to ensure that all possible flutter modes from the higher modes are accounted for. Unlike divergence (which appears to be a function only of the first wing bending mode), flutter can be defined by modes other than just the first torsion mode, and these higher torsion modes can also produce flutter instabilities. If these higher torsion modes have frequencies low enough so that the flap actuators can respond to them, these modes must be monitored carefully in the analyses. They must not be destabilized by the feedback loops aimed at a flutter condition caused by a lower frequency mode. If flutter from higher modes cannot be avoided, high frequency filters may be required to prevent these higher modes from going unstable at low airspeeds.

These examples of active control applications using the Case 1 and Case 2 wing designs are meant to suggest potential for active control of aeroelastic instabilities. Actual forward-swept wing applications could demonstrate even larger improvements in critical airspeeds, especially for divergence. This can happen since forward-swept wings usually have very high values for  $U_f$  even without feedback compensation. The actual stability improvements will depend on the details of each application. However some general observations and conclusions of active control for forward-swept wing aeroelasticity can be made and follow in the next chapter.

#### IV - CONCLUSIONS

The results of the cantilever wing examples suggest that active control can be used to increase the critical airspeeds of flutter and divergence in forward-swept wings. In order to determine the exact increases in these critical airspeeds that is available using active control, a match-point analysis would be required to match critical airspeeds with their correct Mach number and altitude. This is not done here because that level of detail is not needed to determine the trends sought in this research. Consistent with this approach, improvements of 25% in  $U_d$  for one example and 30% in  $U_f$  are made for another example of cantilever forward-swept wing designs. These improvements would be even greater if the secondary aeroelastic instabilities had higher critical airspeeds. They limited the improvement because as the critical airspeeds for the primary (most critical) instabilities are increased to large values with active control, the secondary instabilities then determine the most critical airspeeds for the wings. Unfortunately, the critical airspeed for the secondary instability is shown in one example to decrease at the same time that the airspeed of the primary instability increases. In Case 1,  $U_f$  drops severely as  $U_d$  increases, with the application of active controls. However, if active controls were applied to a forward-swept wing of conventional construction this loss in flutter speed could be tolerated. The secondary instability of flutter has shown to be high without active control for forward-swept wings of conventional construction. Therefore, with application of feedback control, the critical airspeed for flutter could drop considerably, in trade for increases in the critical airspeed for divergence. By improving this divergence instability active controls can make metal construction of forward-swept wings feasible. This same argument can also be applied to conventional (non-aeroelastically tailored) composite wing construction.

The trade in improvement of  $U_d$  at the expense of a lower  $U_f$  suggests a possible modification of current optimal design logic for designs that will

use active control for aeroelastic instabilities. Typically, optimal design methods (especially those automated on digital computers) attempt to hold the wing's structural weight to a minimum, while moving all aeroelastic failure mechanisms outside the wing's performance envelope. This design optimum is useful for wings that do not employ active control for aeroelasticity. It does however tend to produce designs in forward sweep that have  $U_d$  and  $U_f$  close together and just outside the operating envelope of the aircraft. This optimum criteria may not always be the most useful for wing designs that incorporate active control for divergence instabilities. Since no control law, using any combination of sensor and flap configuration, could be found to improve both flutter and divergence at the same time, a different design optimum may be more useful for forward-swept wings. Techniques (such as aeroelastic tailoring for a composite wing structure) may provide better candidate designs for active control of divergence if the optimal design procedure focuses on providing extremely high airspeeds for flutter. Then active control would be focused on divergence. A drop in the critical airspeed for flutter could then be tolerated if necessary as active control provides the necessary increases in divergence airspeed.

Since divergence is a static aeroelastic instability, it should be expected that displacement feedback provides the only successful active-control suppression of divergence. Unfortunately divergence suppression could not at same time be successfully combined with flutter suppression to compensate a wing that had low values of both  $U_d$  and  $U_f$ . The feedback solution for one instability tended to disable the feedback compensation for the other instability. This lack of compatibility between divergence and flutter compensation suggests that applications of optimal control techniques (that use full-state feedback) could have difficulty with wings that have unacceptable values for both  $U_d$  and  $U_f$ .

Some insight can be gained from these examples into the best locations for sensors and control surfaces to improve the divergence instabilities of forward sweep. For divergence, sensor locations and signal combinations

that provide angle-of-attack information appear to be the most useful. Consequently signal differencing between sensors located streamwise is desirable for divergence compensation. For flutter however, accelerometer locations strongly depend on the wing dynamic responses of each particular application. Therefore optimum locations for sensors used in flutter compensation cannot be suggested for all wing designs using just these examples. When considering control surface configurations, the best flap locations for divergence suppression should be near the wing tips. The leading edge provides great influence for a flap of small size on the pressure distributions of a forward-swept wing. Thus the leading-edge tip region appears to be the best location for control surfaces that must stabilize divergence. The best flap locations for flutter suppression of forward sweep on the other hand requires further study. Again the dynamic responses that contribute to the flutter mechanism depend heavily on the particular characteristics of each wing design. Locations of node lines and maximum amplitude areas for the vibration modes usually dictate the best locations for the flaps providing flutter suppression.

While developing promising active control compensation for aeroelasticity, improvements were also made in the methods for calculating aeroelastic stability. Based on the airfoil stability results, a Padé Approximant aerodynamic-force formulation was used for the damped motion of the cantilever wings and contributed to very good stability predictions. The key modification to the formulation of the Padé Approximants is the common denominator. When the averaging of the denominators is used, the additional roots in the stability analyses (introduced by aerodynamics) are held to a minimum, and none of these "aerodynamic" roots have positive real parts. Thus, the Padé Approximants did not confuse the determination of structural stability using the structural roots with an unacceptable number of "extra" roots from the aerodynamic approximations. Now when good experimental force data from damped lifting surface motion are measured and made available for correlation new insight may then be gained leading to better functions for aerodynamic approximations. These data are especially needed for control surface motion. A prime candidate would be fractional

orders of  $s$  similar to those used by Bagley for viscoelastic materials (Ref. 31). The fractional orders of his method are suggested aerodynamically by the Bessel functions in the doublet-lattice sinusoidal solution used as the basis for the Padé Approximants. The polynomials used in this dissertation, however, are very easy to include in the transformed equations of motion. Also their agreement with known experiments are so good that the solution difficulties when calculating wing stability using other approximating functions may far outweigh improvements new functions could offer in stability predictions.

There were also some consistent trends observed in the root locus plots that may be useful whether active control is considered or not. The root loci for all the uncompensated airfoils and cantilever wings suggest that roots associated with the first bending or plunge mode will always define divergence. A similar observation can be made for flutter. The root associated with the lowest vacuum frequency torsion mode defines flutter as long as there is no active control present. The divergence result stems logically from the great similarity between a wing's deflection shape at divergence and its first bending mode. The equivalent association of flutter with the lowest torsion mode is not as clear. Since flutter of cantilever wings can be obtained using only the degrees-of-freedom associated with the modes of first torsion and first bending (Ref. 2), it would seem that there should be some flutter examples that are defined by loci associated with the bending modes of vibration. No example of this flutter can be found in these cases, however.

In summary, successful applications are made here of active control to the aeroelastic instabilities of flutter and divergence in forward-swept wings, the prime goal of this research. The active control results from the wing examples show specifically that it is possible to improve the aeroelastic stability of forward-swept aircraft wings of conventional construction with active control. The use of conventional design techniques to determine the best compensation configurations provided some insight into the most useful control surfaces and wing measurements for

improving aeroelastic stability. Optimal control techniques should now be used to obtain the maximum improvements available with active control for these aeroelastic instabilities for particular aircraft applications.



# BIBLIOGRAPHY

1. Schlichting, H., Boundary Layer Theory, J. Kestin, trans., 6th ed., McGraw-Hill, New York, 1968.
2. Bisplinghoff, R. L., Ashley, H., and Halfman, R. L., Aeroelasticity, Addison Wesley, Massachusetts, 1955.
3. DeMeis, Richard, "Forward Swept Wings Add Supersonic Zip," High Technology, Jan-Feb, 1982.
4. Weisshaar, T. A., "Divergence of Forward Swept Composite Wings," AIAA Paper No. 79-0722, 1979.
5. Griffin, K. E., "An Aeroelastic Tailoring Study of a High Aspect Ratio Wing," NASA TM-X-337, Nov., 1975.
6. Krone, N. J., "Divergence Elimination With Advanced Composites," AIAA Paper No. 75-1009, 1975.
7. Rauch, F., and Wilkinson, H., Final Report for Air Force Flight Dynamics Laboratory of Contract F33615-78-3223, 1979.
8. Griffin, K. E., and Eastep, F. E., "Active Control of Forward Swept Wings With Divergence and Flutter Aeroelastic Instabilities," AIAA Paper No. 81-0637, 1981.
9. Miller, G. D., Wykes, J. H., and Brosnan, M. J., "Rigid Body-Structural Mode Coupling on a Forward Swept Wing Aircraft," AIAA Paper No. 82-0603, 1982.
10. Chipman, R. R., Zislin, A. M., and Waters, C., "Active Control of Aeroelastic Divergence," AIAA Paper No. 82-0684, 1982.
11. McRuer, B. T., Benun, D., Olick, G. E., "The Influence of Servomechanisms on the Flutter of Servocontrolled Aircraft," AFTR No. 6287, March 1954.
12. Andeer, R. E., "Stabilizing Flexible Vehicles," Astronautics and Aeronautics, Aug 1964.
13. Rogers, K. L., Hodges, G. E., and Felt, L., "Active Flutter Suppression-A Flight Test Demonstration," Journal of Aircraft, Vol.12, June 1975.
14. Hwang, C. and Pi, W. S., "Application of Optimal Control Techniques to Aircraft Flutter Suppression and Load Alleviation," AIAA Paper No. 82-0724, 1982.

15. Peloubet, R. P., Jr., Haller, R. L., and McQuien, L. J., "Feasibility Study and Conceptual Design for Application of NASA Decoupler Pylon to the F-16," NASA Contractor Report 165834, May 1982.
16. Theodorsen, T., "General Theory of Aerodynamic Instability and the Mechanism of Flutter," NACA Report 496, 1935.
17. Fant, J. A., "Conceptual Design of Advanced Composite Airframes," Air Force Materials Laboratory, AFML-TR-73-4, Feb. 1973.
18. Giesing, J. P., Kalman, T. P., and Rodden, W. P., "Subsonic Unsteady Aerodynamics for General Configurations," Air Force Flight Dynamics Laboratory, AFFDL-TR-71-5, April, 1972.
19. Vepa, R., "On the Use of Padé Approximants to Represent Unsteady Aerodynamic Loads for Arbitrarily Small Motions of Wings," AIAA Paper No. 76-17, Jan. 1976.
20. Edwards, J. W., Ashley, Holt, and Breakwell, J. V., "Unsteady Aerodynamic Modeling for Arbitrary Motions," AIAA Paper No. 77-451, 1977.
21. Baker, G. A., Jr., Essentials of Padé Approximants, Academic Press, 1975.
22. Schwanz, R. C. and Heath, C. B., "Application of Aerodynamic Approximating Functions To An Aspect Ratio 6.8 Flexible Wing," Air Force Flight Dynamics Laboratory, AFFDL-TM-78-88-FGC, Feb. 1979.
23. Peloubet, R. P., Haller, R. L., and Bolding, R. M., "F-16 Flutter Suppression System Investigation," AIAA Paper 80-0768, May 1980.
24. D'Azzo, J. J., and Houpis, C. H., Linear Control System Analysis and Design: Conventional and Modern, McGraw-Hill, 1975.
25. Smith, B. T., Boyle, J. M., Garbow, B. S., Ikebe, Y., Klema, V. L., and Moler, C. B., Matrix Eigensystem Routines, Springer-Verlag, 1974.
26. Bjorck, Ake, and Dahlquist, Germund, Numerical Methods, Prentice Hall, New Jersey, 1974.
27. Destuynder, R., "ESSAI E. Soufflerie Dun Suppresseur de Flottemen Sure Une Aile Droite," 40th Meeting of Structures and Materials Panel of AGARD in Brussels, April 1975.
28. Theodorsen, T. and Garrick, I. E., "Flutter Calculations in Three Degrees-of-Freedom," NACA Report 736, NACA, 1941.
29. Nissim, E., "Flutter Suppression Using Active Controls Based on the Concept of Aerodynamic Energy," NASA-TND-6199, March 1971.

30. Hassig, H. J., "An Approximate True Damping Solution of the Flutter Equation by Determinant Iteration," Journal of Aircraft, Vol. 8, Nov. 1971.
31. Bagley, R. L., "Applications of Generalized Derivatives to Viscoelasticity", Air Force Material Laboratory, AFML-TR-79-4103, November 1979.
32. Sherrer, V. C., Hertz, T. J., and Shirk, M. H., "A Wind Tunnel Demonstration of the Principle of Aeroelastic Tailoring Applied to Forward Swept Wings," AIAA Paper No. 80-796, May 1980.
33. The NASTRAN User's Manual, (Level 17.0) NASA SP-222 (04), National Aeronautics and Space Administration, Washington, D. C., December 1979.
34. McCullers, L. A., and Lynch, R. W., "Dynamic Characteristics of Advanced Filamentary Composite Structures," Air Force Flight Dynamics Laboratory, AFFDL-73-111, Sept 1974.

## APPENDIX A

### Solution Method Evaluations Using

#### A 2-D Airfoil

The following presents an evaluation of possible aerodynamic formulations and their solution methods that can be used for wing stability analysis. The lifting surface used for the evaluation is a simple two-dimensional airfoil that was used by Theodorsen (Ref. 16) to develop stability methods for the prediction of aeroelastic flutter and divergence. There are two possible methods that can be used with the stability calculations of the airfoil. First, a direct method suggested by Edwards (Ref. 20); and second, a more indirect method using Padé Approximants as suggested by Vepa (Ref. 19). The results of this airfoil study suggests the Padé Approximant method for the forward-swept cantilever wing.

#### Geometry

The two-dimensional airfoil for these method comparisons is shown in Figure A1. The airfoil is suspended from two linear elastic springs in an airflow moving from left to right in the figure. The spring suspension is shown connected to the shear center location of the camber line in Figure A1A. The forces acting on this same airfoil are shown in Figure A1B. This simple airfoil geometry permits the economical evaluation of two different formulations of aerodynamic forces for damped lifting-surface motion.

The airfoil geometry of Figure A1A uses as a basic dimension the semi-chord  $b$ , with most of the other dimensions represented as fractions of  $b$ . Thus, the chord length is  $2b$ , with the  $y$  axis passing through the mid-chord of the airfoil. The two degrees-of-freedom used to define the airfoil motions are airfoil plunge (vertical displacement,  $h$ , in the negative  $y$  direction) and airfoil pitch angle ( $\theta$ , or rotation). For this pitch angle, clockwise is positive. The plunge motion of the airfoil

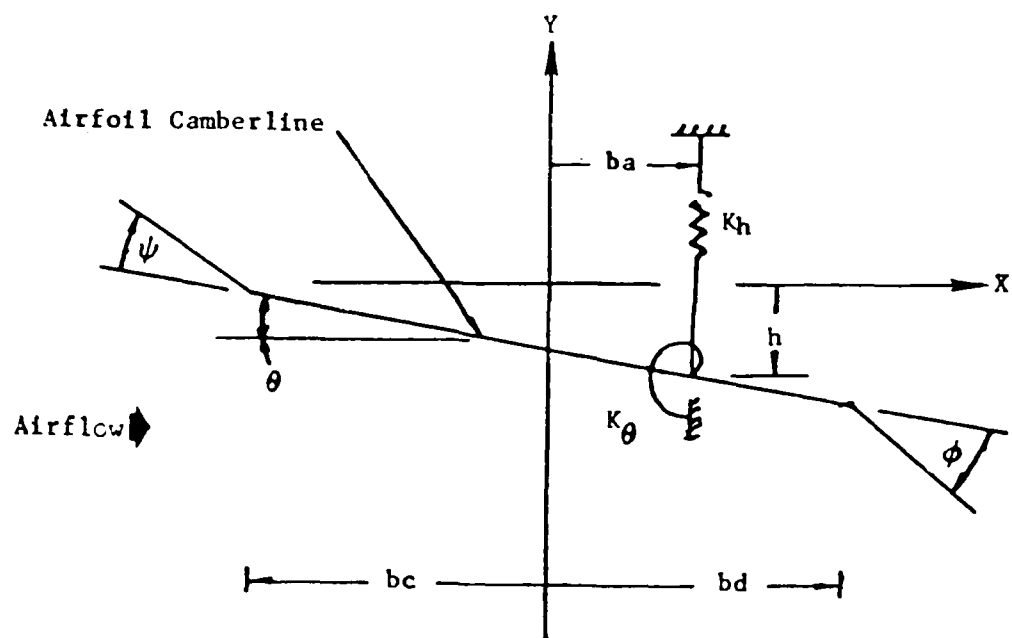


Figure A1A Geometry For The Airfoil And Its Flap Degrees-of-Freedom

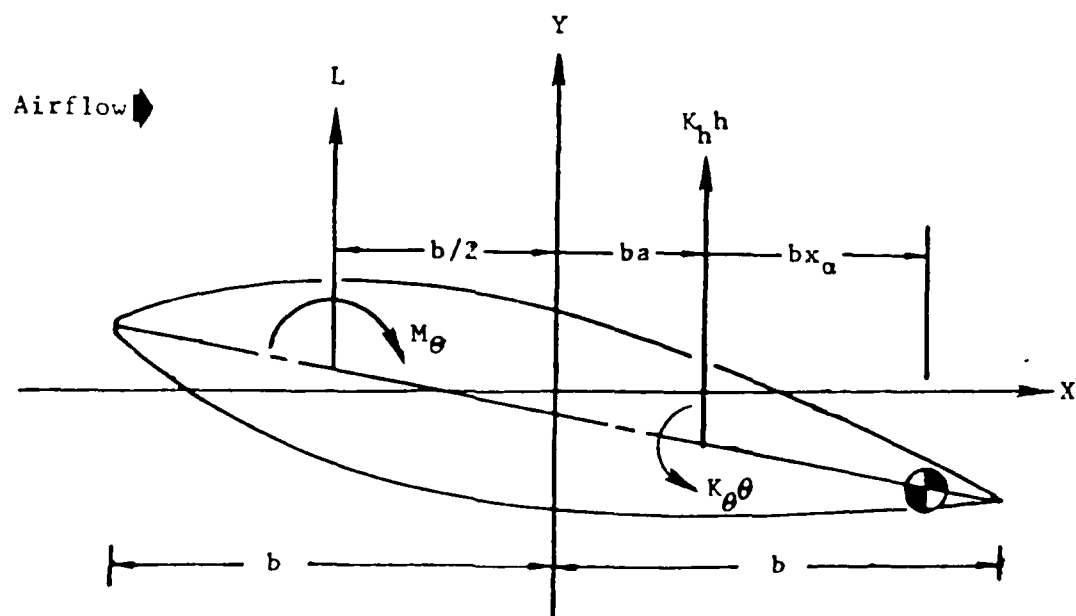


Figure A1B Geometry For The Airfoil Forces

corresponds to the motion of a streamwise section at any span station of an unswept wing, as that wing undergoes bending deformation. The pitch motion corresponds to wing torsional deformations at that same wing section. The airfoil aerodynamic loads are resisted both by the linear torsional spring (twisted with the pitch-angle rotation) and the linear extension/compression spring (deformed with the plunge translation). These springs are attached at the airfoil's shear center, a location that allows the decoupling of its plunge stiffness from its torsional stiffness. This shear center is a distance  $b_a$  downstream from the airfoil mid-chord. The two springs are represented by the spring constants  $K_h$  and  $K_\theta$  for the plunge and torsional stiffness respectively.

Also shown in Figure A1A is the geometry for leading- and trailing-edge flaps used for aeroelastic stability augmentation of the airfoil. The hinge point for the leading-edge flap is located  $c_b$  aft of the mid-chord. Likewise, the trailing-edge hinge point is  $d_b$  aft of the mid-chord. The deflection angles are measured relative to the chord line of the airfoil, with a positive rotation being clockwise.

In Figure A1B, the forces acting on the airfoil and the airfoil's center-of-gravity (c.g.) are shown. The c.g. is located a distance  $b_x$  downstream from the shear center, and it is at this location that the translational (plunge) mass  $M_h$  and the airfoil's rotary-pitch inertia  $I_\theta$  are defined. The aerodynamic forces on the airfoil are represented by two force components, the aerodynamic lift,  $L$ , and pitching moment,  $M_\theta$ , acting at the airfoil's quarter chord. The linear springs provide structural resisting forces to the airfoil deflections  $h$  and  $\theta$  that are linearly related to these deflections by the spring constants  $K_h$  and  $K_\theta$ .

The stability calculations for the airfoil are made using an equilibrium position defined as zero angle-of-attack and zero plunge displacement. Thus, prior to disturbing the airfoil, the equilibrium conditions are zero lift,  $L$ , and zero aerodynamic pitching moment,  $M_\theta$ .

Using this basic airfoil geometry, Theodorsen developed many examples of critical airspeeds for flutter,  $U_f$ , and divergence,  $U_d$ . The differences in the examples were created by varying such airfoil characteristics as  $M_h$ ,  $I_\theta$ ,  $K_h$ ,  $K_\theta$ ,  $x_a$ , etc. Two of these examples are used in the evaluation of the aerodynamic-force formulations to be used for the wing stability calculations. The equations of motion for the airfoil will now be developed.

### Equations of Motion

The airfoil equations of motion are developed in a similar manner as those for the cantilever wing. Lagrange's equation, equation 12, is applied to energy terms developed for the two degrees-of-freedom of the airfoil. Due to the small number of degrees-of-freedom, the  $h$  and  $\theta$  are used directly to describe the airfoil motion rather than using a coordinate change to the vacuum vibration modes.

The kinetic energy  $T$  for the airfoil is calculated using the velocities of each element of mass along the chord of the airfoil. As in the cantilever wing, the assumption of small displacements is again made. Because velocities in the vertical direction are the only velocities large enough to significantly contribute to the kinetic energy, the vertical displacement along the wing chord,  $\tilde{h}(x)$ , is used to calculate these velocities.

$$\tilde{h}(x) = -h - \theta(x - ba) \quad (A.1)$$

The airfoil's kinetic energy then is the sum of the velocity and mass contributions along the chord line:

$$\begin{aligned} T &= \int_{-b}^b \frac{1}{2} (\dot{\tilde{h}})^2 \tilde{\rho} dx \\ &= \int_{-b}^b \frac{1}{2} [-\dot{h} - \dot{\theta}(x - ba)]^2 \tilde{\rho}(x) dx \end{aligned} \quad (A.2)$$

As a function of chord location, the mass of the airfoil is  $\bar{\rho}$ . The kinetic energy can be written in a simplified way.

$$M_h = \int_{-b}^b \bar{\rho}(x) dx \quad (A.3)$$

$$I_\theta = \int_{-b}^b (x - ba)^2 \bar{\rho}(x) dx \quad (A.4)$$

$$\begin{aligned} S_\theta &= \int_{-b}^b (x - ba) \bar{\rho}(x) dx \\ &= bx_\alpha M_h \end{aligned} \quad (A.5)$$

All of these equations allow the kinetic energy to be expressed as:

$$T = 1/2 M_h \dot{h}^2 + 1/2 I_\theta \dot{\theta}^2 + S_\theta \dot{\theta} \dot{h} \quad (A.6)$$

The term  $S_\theta$  is the inertial coupling introduced between  $\theta$  and  $h$ . It is necessary since  $h$  is measured from the shear center and not the c.g. location. The strain energy term  $U$  for the airfoil is the summation of the strain energy in the pitch and plunge springs created by displacements in  $\theta$  and  $h$ .

$$U = 1/2 h^2 K_h + 1/2 \theta^2 K_\theta \quad (A.7)$$

All that is needed for the airfoil stability calculations is the generalized airforces. Two possible formulations of aerodynamic forces will be developed in the following sections. The aerodynamic formulations dictate the stability solution method that can be used.

Applying equation 2 to the kinetic and the strain energy calculations for the airfoil, the equations of motion are derived, one for each degree-of-freedom of the airfoil.



$$M_h \ddot{h} + S_\theta \ddot{\theta} + K_h h = Q_h \quad (A.8)$$

$$S_\theta \ddot{h} + I_\theta \ddot{\theta} + K_\theta \theta = Q_\theta \quad (A.9)$$

The equations are organized in matrix form in a similar fashion to that of the wing.

$$\begin{bmatrix} M_h & S_\theta \\ S_\theta & I_\theta \end{bmatrix} \begin{Bmatrix} \ddot{h} \\ \ddot{\theta} \end{Bmatrix} + \begin{bmatrix} K_h & 0 \\ 0 & K_\theta \end{bmatrix} \begin{Bmatrix} h \\ \theta \end{Bmatrix} = \begin{Bmatrix} Q_h \\ Q_\theta \end{Bmatrix} \quad (A.10)$$

$$[M] \begin{Bmatrix} \ddot{h} \\ \ddot{\theta} \end{Bmatrix} + [K] \begin{Bmatrix} h \\ \theta \end{Bmatrix} = \begin{Bmatrix} Q \\ \end{Bmatrix}$$

Since the airfoil is used to evaluate aerodynamic-force formulations employed later on the cantilever wing in the Laplace domain, the equations of motion for the airfoil must also be transformed using the Laplace operator. Therefore, equation A.10 is transformed in a similar manner to that performed on equation 11.

$$s^2 [M] \begin{Bmatrix} \bar{h} \\ \bar{\theta} \end{Bmatrix} + [K] \begin{Bmatrix} \bar{h} \\ \bar{\theta} \end{Bmatrix} = \begin{Bmatrix} \bar{Q}_h \\ \bar{Q}_\theta \end{Bmatrix} \quad (A.11)$$

When the generalized forces are also transformed to the Laplace domain (as will be shown in the following sections), the stability for the airfoil is then determined by the airfoil's response to a small disturbance as indicated by the value of the roots of the airfoil's characteristic equation.

### Aerodynamic Forces

The aerodynamic forces are developed next for the airfoil in the Laplace domain. For active control applications, these aerodynamic forces must also include contributions made by the movement of leading- and trailing-edge flaps. In order to account for damped airfoil motion, two formulations are examined for suitability with the wing calculations. The first method gives damped-motion airfoil aerodynamics similar to those

developed for sinusoidal airfoil motion by Theodorsen. The second method is a formulation that uses Padé Approximant polynomials to approximate the aerodynamic forces. The discussion of these methods can be made clearer by first recalling Theodorsen's sinusoidal method.

#### Theodorsen's Method

For two-dimensional incompressible flow over a sinusoidally oscillating airfoil, Theodorsen (Ref. 16) developed the aerodynamic lift and moment forces of equation A.12 as functions of time. The sinusoidal lift,  $L$ , and moment,  $M_{s.c.}$ , are defined at the airfoil's shear center by the following equations:

$$L = \pi \rho b^2 [\ddot{h} + U\dot{\theta} - bC_{1\alpha} \ddot{\theta}] + 2\pi \rho U b \mathcal{C}(k) [\dot{h} + U\theta + b(.5 - C_{1\alpha}) \dot{\theta}] \quad (A.12a)$$

$$M_{s.c.} = \pi \rho b^2 [bC_{1\alpha} \ddot{h} - U b (.5 - C_{1\alpha}) \ddot{\theta} - (1/8 + C_{1\alpha}^2) \ddot{\theta}] + 2\pi \rho U b^2 (.5 + C_{1\alpha}) \mathcal{C}(k) [\dot{h} + U\theta + b(.5 - C_{1\alpha}) \dot{\theta}] \quad (A.12b)$$

Here  $\rho$  and  $U$  are the freestream density and airflow velocity respectively;  $C_{1\alpha}$  is the lift-curve slope of the airfoil section; and  $\mathcal{C}(k)$  is the Theodorsen Function of the reduced frequency  $k$  described in equation A.14. The Theodorsen Function  $\mathcal{C}(k)$  is defined as a ratio of Hankel functions in the variable  $k$ .

$$\mathcal{C}(k) = (H_1^{(2)}(k)) / (H_1^{(2)}(k) + iH_0^{(2)}(k)) \quad (A.13)$$

These are zero- and first-order Hankel functions of the second kind. Here  $k$  is the frequency of airfoil oscillation that is non-dimensionalized by the airfoil semichord and freestream velocity.

$$k = \omega b / U \quad (A.14)$$

Using the Theodorsen Formulation for the aerodynamic forces, neutral stability airspeeds for the airfoil can be found. In these stability

calculations, solutions of the equations of motion are obtained for oscillatory motion that is of constant amplitude, the type of motion on which the Theodorsen formulation can be applied.

#### Edwards' Method

The aerodynamic-force formulation used with the active controls must be expanded to include damped motion of the lifting surface. Also the Laplace domain is the most convenient domain for solving design problems in linear controls. The solution methods, in the Laplace domain, involve only algebraic manipulations of the equations of motion. Edwards (Ref. 20) suggests a method for extending the Theodorsen formulation to damped airfoil motion in the Laplace domain. This method provides a direct calculation of these airloads, provided that the value of the Laplace variable  $s$  describing the wing's motion is known a priori.

The development of this method, which is described in detail in Reference 20, is highlighted next. The Edwards' formulation gives the transformed loads of lift and moment (caused by damped motion) at the shear center of the airfoil section in a similar fashion to Theodorsen's sinusoidal formulations. The airloads are essentially the Laplace transforms of equations A.12, where the transform  $\bar{e}(\bar{s})$  of the Theodorsen Function  $e(k)$ , is again calculated from Bessel functions.

$$\bar{e}(\bar{s}) = (K_1(\bar{s})) / (K_0(\bar{s}) + K_1(\bar{s})) \quad (A.15)$$

The terms  $K_0$  and  $K_1$  are modified Bessel functions of the second kind, zero and first-order respectively. The variable  $\bar{s}$  is a non-dimensionalized form of the transformed variable  $s$ . It contains the reduced frequency of oscillation in its imaginary part.

$$\begin{aligned} \bar{s} &= sb/U \\ &= \sigma b/U + ik \end{aligned} \quad (A.16)$$

When put in a matrix form, these transformed aerodynamic forces define an influence coefficient matrix that is compatible with the aerodynamic forces of equation A.11.

$$\begin{Bmatrix} \bar{Q}_h(s) \\ \bar{Q}_\theta(s) \end{Bmatrix} = \begin{bmatrix} \bar{A}_{hh} & \bar{A}_{h\theta} \\ \bar{A}_{\theta h} & \bar{A}_{\theta\theta} \end{bmatrix} \begin{Bmatrix} \bar{h} \\ \bar{\theta} \end{Bmatrix} \quad (A.17)$$

The elements of this matrix can be recognized as the transformed constituents of equations A.12, with a typical example being shown in equation A.18.

$$\begin{aligned} \bar{A}_{\theta\theta} = \pi \rho b^2 [ & -Ub(.5 - C_{1\alpha})s - b^2(1/8 + C_{1\alpha}^2)s^2] \\ & + 2 \pi \rho b^2 (C_{1\alpha} + .5) \bar{c} [U + b(.5 - C_{1\alpha})s] \end{aligned} \quad (A.18)$$

This formulation for the airfoil's aerodynamics causes some difficulty when it is used in the stability calculations of the airfoil. The difficulty is caused by the Bessel functions contained in the  $\bar{c}$  formulation. The variable  $s$  cannot be factored out of these Bessel functions. Thus,  $s$  must be known in order to obtain a value for  $\bar{c}(s)$ . Unfortunately,  $s$  is one of the values sought in the stability analyses. This difficulty with the Edwards' formulation for the airfoil's aerodynamic forces requires a cumbersome iteration method for the stability calculations (discussed later). But what is needed is a way of posing the airfoil (and later, the wing) aerodynamics in such a way that the motion variables can be factored out of the airload predictions. The following approximation method provides just such an aerodynamic formulation.

#### Padé Method

Several sets of aerodynamic forces, calculated for different frequencies and damping levels of airfoil motion, can be used in the development of airload approximations for damped motion by use of Padé Approximants (Ref. 19). First the aerodynamic forces corresponding to selected values of damped airfoil motion can be calculated using Edwards' method. The value of  $s$  corresponding to the motion contains the damping level in its real part and the frequency in its imaginary part. Using a set of different  $s$  values, a corresponding set of damped aerodynamic forces can be calculated that can be used to estimate the forces as functions of  $s$ . Approximations can be made of the airfoil's aerodynamic forces

(calculated for different values of  $s$ ) by requiring a least-squares fit of selected functions of  $s$  to the above aerodynamic forces. The functions used to approximate the aerodynamic forces are chosen based on their accuracy of approximation and their compatibility with the equations of motion. The form used in this research is the Padé polynomial approximation similar to that suggested by Vepa. It provides a functional form for the approximations that easily combines with the other terms in the equations of motion. Note that the special case of sinusoidal motion of constant amplitude can be directly related to a reduced frequency used with sinusoidal aerodynamic-force calculation. This relationship can be seen using the non-dimensional form of  $s$ .

$$\begin{aligned}\bar{s} &= b(0. + i\omega)/U \\ &= ik\end{aligned}\tag{A.19}$$

The form of the Padé Approximant used here for the aerodynamic forces delineates ratios of polynomials in  $s$ .  $P_{fjl}$  and  $Q_{fjl}$  are the real-value coefficients of the variable  $s^f$ , with the limits of  $f$  being  $n$  and  $d$  for numerator and denominator respectively.

$$\bar{A}_{jl} = \left[ \sum_{f=0}^n (P_{fjl}) s^f \right] / \left[ 1. + \sum_{f=0}^d (Q_{fjl}) s^f \right]\tag{A.20}$$

The values of  $n$  and  $d$  determine the orders of the polynomials used to approximate the aerodynamic forces. The orders of the polynomials for the airfoil calculations are selected using criteria based on the upper and lower limits of the frequency of the aeroelastic instability that must be calculated. For the stability analyses, the need for high orders for polynomials is tempered with the need to minimize the computational effort that increases as  $n$  and  $d$  increase. The relative order of numerator polynomial versus the denominator polynomial is based on the high and low frequency limits of the lifting force  $L$ . The orders of  $s$ ,  $O(s^i)$ , from a Laplace transformation of equation A.12 would be as follows.

$$\bar{L}(s) = f_1(0(s^2)) + f_2(0(s)) \bar{C}(s) \quad (A.21)$$

Here the function  $f_1$  is the non-circulatory lift term containing second-order terms of  $s$ , and the function  $f_2$  is the circulatory lift term containing first-order terms of  $s$ . When the orders are determined for the approximation to  $\bar{C}(s)$ , the overall orders for lift and moment approximations can be calculated.

The polynomial approximation of  $\bar{C}(s)$  is suggested by its equivalent formulation for indicial responses. The basic form of the  $\bar{C}$  approximation is a polynomial ratio of  $s$ .

$$\bar{C}(s) = \left[ \sum_{i=1}^{\hat{n}} P_i s^i \right] / \left[ \sum_{j=1}^{\hat{d}} Q_j s^j \right] \quad (A.22)$$

Here  $P_f$  and  $Q_f$  are real coefficients of  $s$ . The best choice for the ratio of  $\hat{n}$  to  $\hat{d}$  can be obtained from Wagner's Indicial Function  $\bar{\Gamma}(s)$  (Ref. 20). This function  $\bar{\Gamma}(s)$  is found in the response caused by indicial input in the same way that the sinusoidal Theodorsen Function  $C(k)$  is found in response to sinusoidal input. The limits that  $\bar{\Gamma}(s)$  exhibit are displayed in terms of the variable  $s$ .

$$\lim_{s \rightarrow \infty} \bar{\Gamma}(s) = .5 \quad (A.23)$$

$$\lim_{s \rightarrow \infty} \bar{\Gamma}(s) = 1.$$

If a ratio of polynomials is used to approximate  $\bar{\Gamma}$ , the above limits would require the numerator and denominator to be the same order. This ratio for  $\bar{\Gamma}$  suggests that the  $\bar{\Gamma}$  counterpart,  $\bar{C}(s)$  should also have equal-order polynomials. Therefore,  $\hat{d}$  equals  $\hat{n}$  for the  $\bar{C}(s)$  polynomial approximations.

With the ratio of polynomial orders set for  $\bar{e}$ , the approximation can be included in equation A.21 to obtain the ratio of polynomials needed for the aerodynamic forces. An example of the evaluation needed polynomial ratios can be made with the transformed lift forces created by the airfoil plunging degree-of-freedom. The force  $\bar{L}_h$  is put in the form of equation A.21, and the approximation for  $\bar{e}$  is included.

$$\bar{L}_h(s) = f_1(0(s^2)) + f_2(0(s)) \bar{e}(0(s^{\hat{d}}/s^{\hat{d}})) \quad (A.24)$$

Equation A.24 can be rearranged to show the orders of  $s$  needed for the polynomial approximation for this force.

$$\bar{L}_h = f_3(0(s^{\hat{d}+2}) / 0(s^{\hat{d}})) \quad (A.25)$$

Equation 25 shows that the order of the numerator for  $\bar{L}_h$  should be two higher than the order of the denominator. This same relative order can be found for each degree-of-freedom contribution to the loads.

With the ratio of the polynomial orders determined, the absolute value of these orders is defined by a series of comparisons. These comparisons are made between airloads calculated using Padé Approximants for several values of  $\hat{d}$  and those calculated by the Edwards' formulation. Examples of these comparisons are given in Table A1. In these examples the component of lift caused by constant amplitude-plunge oscillations is calculated for several values of frequency using Edwards' exact method. These forces are then compared to forces calculated using Padé Approximants. The Padé calculations are made with three different orders for the polynomial approximations. By comparing between the exact calculations of  $\bar{L}_h$  and those made using the approximations (both real and imaginary), the choice of 1 for  $\hat{d}$  is best.

The aerodynamic forces just discussed are forces resulting from motion caused by the airfoil alone. When the control-surface motion is added to the airfoil, this influence on the lift and moment of the airfoil requires

Table A1 Comparisons Of Polynomial Orders\* For Padé Fit  
Of Aerodynamic  $\bar{L}_h$

$\bar{L}_h$

s	Edwards'	$\hat{d}=1$	$\hat{d}=2$	$\hat{d}=3$
.01i	.003 +i.062	.003 +i.059	.003 +i.059	.002 +i.062
.05i	.033 +i.286	.027 +i.289	.024 +i.283	.035 +i.283
.1i	.077 +.523	.082 +i.539	.051 +i.508	-.166 +i.447
5.i	-77.8 +i15.8	-77.9 +i15.8	-156. +i431.	9350. -i3885

\* The value of  $\hat{d}$  is the polynomial order of the denominator and the numerator is of order  $\hat{d} + 2$ .



a higher order for the denominator of the approximations to obtain a good agreement. This added order for the denominator results in the polynomial orders for the Padé Approximants as order three for the numerator and order two for the denominator. Using these Padé Approximant orders, some examples are given in Table A2 of polynomial coefficients for the lift and moment airloads. In the upper portion of Table A2 an example set of coefficients is presented for the numerator and denominator polynomials of the lift and moment approximations. These coefficients will later be recalculated using a simplification of the denominators.

In the upper half of Table A2, a Padé Approximant polynomial ratio is created for each degree-of-freedom contribution to each aerodynamic force component  $\bar{A}_{ij}$  of the airloads. These polynomial ratios could then be organized into elements of an aerodynamic influence coefficient matrix. However, the denominator from each polynomial ratio would introduce two roots into the characteristic equation for the airfoil equations of motion. To simplify the aerodynamic force representation and reduce to a minimum the number of roots added to the stability calculations, the Padé fitting process is modified. A second aerodynamic least-squares approximation is made using a fixed and non-variable denominator for the Padé Approximants. The denominator polynomials from the first least-squares fit are averaged (giving equal weight to each force component) to form this new fixed denominator polynomial. Thus, this second fit allows the polynomial approximations of all the aerodynamic forces to be expressed with a common denominator. This form for the Padé Approximants will introduce into the overall stability calculations of the airfoil a total of two roots rather than two for each element of the matrix aerodynamic influence coefficients.

Using this common denominator, the transformed aerodynamic forces for the airfoil can be organized in a simplified matrix form. In the airfoil airloads, the denominator's polynomial coefficients can be factored out from the matrix expression of the Padé Approximants.

Table A2 Padé Polynomial Coefficients Of The Airfoil  
Before And After Denominator Averaging

$\bar{A}_{ij}$	$P_3$	$P_2$	$P_1$	$P_0$	$Q_2$	$Q_1$	$Q_0$
	<u>Individual Denominators</u>						
$\bar{A}_{hh}$	15.5	23.3	6.16	0.	-.474	5.82	1.
$\bar{A}_{h\theta}$	62.2	154.	116.	18.6	2.05	8.01	1.
$\bar{A}_{\theta h}$	18.0	-10.6	-3.7	0.	.361	6.29	1.
$\bar{A}_{\theta\theta}$	30.1	159.	-38.5	-11.2	-.739	7.81	1.
	<u>Average Denominator</u>						
$\bar{A}_{hh}$	20.7	27.1	6.2	0.	.3	6.98	1.
$\bar{A}_{h\theta}$	28.2	121.	101.	18.6	.3	6.89	1.
$\bar{A}_{\theta h}$	20.5	-12.2	-3.72	0.	.3	6.98	1.
$\bar{A}_{\theta\theta}$	45.9	131.	-32.1	-11.2	.3	6.98	1.

$$\begin{Bmatrix} \bar{q}_h \\ \bar{q}_\theta \end{Bmatrix} = \frac{1.}{\bar{q}_2 s^2 + \bar{q}_1 s + 1.} \begin{bmatrix} [P_3 s^3 + \dots + P_0]_{hh} \\ [P_3 s^3 + \dots + P_0]_{\theta h} \\ [P_3 s^3 + \dots + P_0]_{h\theta} \\ [P_3 s^3 + \dots + P_0]_{\theta\theta} \end{bmatrix} \begin{Bmatrix} \bar{h} \\ \bar{\theta} \end{Bmatrix} \quad (A.26)$$

With rearrangement, this equation simplifies to equation A.27. The coefficients of the numerators for each force component can be organized into matrices of constants, corresponding to the orders of  $s$ . Each coefficient  $P_{fij}$  is the numerator polynomial coefficient for order  $f$  of  $s$ . It is in the Padé Approximant for force  $i$ , resulting from degree-of-freedom  $j$ .

$$\begin{Bmatrix} \bar{q}_h \\ \bar{q}_\theta \end{Bmatrix} = [\bar{A}] \begin{Bmatrix} \bar{h} \\ \bar{\theta} \end{Bmatrix} \quad (A.27)$$

Table A2 shows the results of using the denominator averaging for the Padé Approximants of the airfoil. In the lower half of the table, the coefficients of the numerator and denominator are listed that result from applying the denominator averaging and second least-squares fit. There are only small changes in the numerator coefficients, except for the  $\bar{A}_{h\theta}$  Padé Approximant. The  $P_{3h\theta}$  in this term (the coefficient of  $s^3$  in  $\bar{A}_{h\theta}$ ) is changed. Fortunately, even with the simplification of the polynomial denominator, examples shown in Appendix C demonstrated exact agreement of neutral-stability airspeeds between airfoils using the Padé Approximant aerodynamic forces and the neutral stability airspeeds first calculated by Theodorsen.

With the choice of polynomial orders determined, the values of  $s$  used to generate the airloads that provide the best least-squares fitting results must be selected. In selecting values of  $s$  to generate forces for the least-squares fittings, the most important measure of merit is the ability for the resulting force approximations to predict the correct

flutter and divergence airspeeds. Secondary criteria are the responses of the wing section below the critical velocities for flutter and divergence. However, the instability velocities must be predicted correctly, or the sub-critical responses are not useful. For predictions of  $U_d$ , values of  $s$  defining reduced frequencies at or near zero are essential. This requirement results from the zero-frequency nature of aeroelastic divergence. For predictions of  $U_f$ , values of  $s$  that define reduced frequencies in the range of .3 are needed for the airfoil examples used in this research. This reduced frequency is an average of the critical reduced frequencies (occurring at the neutral stability point for flutter) in the examples used from Theodorsen's airfoil studies. Higher values of reduced frequency do not improve the predictions of  $U_f$  for any of the configurations of this study. Since higher values of reduced frequency widen the frequency range the fitting process must span, they are not used.

The selection of values of  $s$  used in the least-squares fit for the Padé Approximants is illustrated in Table A3. On the bottom of the table, exact values for  $U_d$  and  $U_f$  are given, calculated by using the damped motion aerodynamic forces suggested by Edwards, which agree exactly with those originally calculated by Theodorsen. In the listings found above these exact values, there are lists of values of  $s$  used to generate airloads for the least-squares fit. The values of  $U_d$  and  $U_f$  (calculated using the force polynomials from the fitting of each list of  $s$ ) are recorded just below the values of  $s$ . In choosing an array of values for  $s$ , both the real and the imaginary values in  $s$  must be selected. Table A3 is typical of several comparisons that can be made. Zero is the best selection for the real parts of  $s$  to be used in calculating Padé Approximants. Therefore, the Padé Approximant polynomials can be calculated using only sinusoidal forces as their basis, since they provide the most accurate approximations for the predictions of  $U_d$  and  $U_f$ .

#### Control Surface Aerodynamics

For the airfoil, calculating aerodynamic forces of the control surfaces can be done using the trailing-edge flap/tab equations that were

Table A3 Comparisons Of Instability Predictions Using Different Data Arrays For The Padé Fit

Data Points for Fitting	S		Padé Predictions	Closed Form Predictions
	S	S		
0	+i.1x10 <sup>-4</sup>	0	U <sub>d</sub> =119 ft/sec	U <sub>d</sub> =129 ft/sec
0	+i.2x10 <sup>-4</sup>	0		U <sub>f</sub> =108 ft/sec
0	+i.7x10 <sup>-4</sup>	.1x10 <sup>-4</sup>		
0	+i.1x10 <sup>-3</sup>	-.2x10 <sup>-4</sup>		
0	+i.2x10 <sup>-3</sup>	-.3x10 <sup>-4</sup>		
0	+i.3x10 <sup>-3</sup>	-.001		
0	+i.7x10 <sup>-3</sup>	-.002		
0	+i.01	-.005		
0	+i.05	-.01		
0	+i.09	-.015		
0	+i.1	-.05		
0	+i.3	-.1		
0	+i.5	-.2		
0	+i.7	-.3		
0	+i.9	-.4		
		-.5		
		+i.1x10 <sup>-4</sup>		
		+i.2x10 <sup>-4</sup>		
		+i.7x10 <sup>-4</sup>		
		+i.1x10 <sup>-2</sup>		
		+i.2x10 <sup>-2</sup>		
		+i.3x10 <sup>-2</sup>		
		+i.7x10 <sup>-2</sup>		
		+i.01		
		+i.05		
		+i.09		
		+i.1		
		+i.3		
		+i.5		
		+i.7		
		+i.9		
			U <sub>d</sub> =118.5 ft/sec	
			U <sub>f</sub> =113 ft/sec	

developed in Reference 28. A coordinate transformation is used that was suggested by Nisum (Ref. 29) to convert the geometry of an airfoil with a trailing-edge flap and trim tab to an airfoil with leading- and trailing-edge flaps. The transformed forces caused by the flaps are added to the equations of motion in the matrix form of equation A.28. The influence coefficient matrix provides forces as functions of the transformed flap-deflection angles  $\bar{\phi}$  and  $\bar{\psi}$ .

$$\begin{Bmatrix} \bar{Q}_h \\ \bar{Q}_\theta \end{Bmatrix} = \begin{bmatrix} \bar{A}_{h\phi} & \bar{A}_{h\psi} \\ \bar{A}_{\theta\phi} & \bar{A}_{\theta\psi} \end{bmatrix} \begin{Bmatrix} \bar{\phi} \\ \bar{\psi} \end{Bmatrix} \quad (\text{A.28})$$

The elements of this matrix contain flap geometry, flow conditions, and the variable  $s$ . These elements were defined first by Theodorsen and converted into the leading- and trailing-edge geometry using the Nisum transformation. A typical element is shown in equation A.29.

$$A_{h\phi} = -\rho u^2 b (-\bar{T}_4 s - \bar{T}_1 s^2 + 2 \bar{T}_{10} + \bar{T}_{11} s) \quad (\text{A.29})$$

The terms  $\bar{T}_1$  and  $\bar{T}_4$  are constants defined by the geometry of the flaps and airfoil in Reference 28. The control surface's aerodynamic forces can be calculated directly using Edwards' method when values of  $s$  are specified, or approximated with Padé Approximants when  $s$  must be factored out of the force formulation. The control-surface forces calculated with the Edwards' method have the same limitation as those forces calculated using his method for general airfoil motion. This limitation is the stipulation that the value of  $s$  must be known before calculating the control-surface forces. Since  $s$  is the root to be solved for in the stability analyses, an iteration method must be used. Again a value of  $s$  is estimated and then checked with the equations of motion to see if it is a desired root. But more direct stability analyses can be made if the control-surface forces are represented by polynomials of a Padé Approximant.

To make the Padé approximation of the control surfaces compatible with those of the airfoil's pitch and plunge motion, the denominator used for

the flaps' aerodynamic forces is taken directly from that used for approximating the airfoil's pitch and plunge motion. The complex constants for equation A.30 are calculated from the same series of  $k$  values used to generate the Padé Approximants for airfoil pitch and plunge motion. Order-three numerator polynomials in  $s$  for each element are calculated. This calculation matches the polynomial orders used with numerator polynomials of the airfoil pitch and plunge motion. The results can be organized in matrix form just like that in equation A.27.

$$\begin{Bmatrix} \bar{q}_h \\ \bar{q}_\theta \end{Bmatrix}_{\text{flap}} = \frac{1.}{\bar{q}_2 s^2 + \bar{q}_1 s + 1.} \left[ \begin{bmatrix} P_{3h\phi} & P_{3h\psi} \\ P_{3\theta\phi} & P_{3\theta\psi} \end{bmatrix} s^3 + \cdots + \begin{bmatrix} P_{0h\phi} & P_{0h\psi} \\ P_{0\theta\phi} & P_{0\theta\psi} \end{bmatrix} \right] \begin{Bmatrix} \bar{\phi} \\ \bar{\psi} \end{Bmatrix}_{\text{flap}} \quad (\text{A.30})$$

$$\begin{Bmatrix} \bar{q}_h \\ \bar{q}_\theta \end{Bmatrix} = \frac{1.}{\bar{q}_2 s^2 + \bar{q}_1 s + 1.} \begin{bmatrix} [P_3] s^3 + \cdots + [P_0] \\ \text{flap} \quad \text{flap} \end{bmatrix} \begin{Bmatrix} \bar{\phi} \\ \bar{\psi} \end{Bmatrix} \quad (\text{A.31})$$

The Padé Approximant of aerodynamic forces for the control-surface deflections are now compatible with the other aerodynamic forces of the airfoil and can easily be included in the airfoil's equations of motion.

#### Control Laws

The feedback loops for the airfoil are shown in Figure A2. They define the relationships between the airfoil's motion (in the degrees-of-freedom of the airfoil) and the deployment of the flaps. In equation form, these relationships are functions that contain linear combinations of the degrees-of-freedom  $h$ ,  $\theta$ , and their derivatives. The flap-rotation angles are then determined by these weighted combinations of the degrees-of-freedom. These weighted combinations are contained in the  $H$  functions.

$$\begin{aligned} \phi &= H_{\phi h}(K_{\phi h}, K_{\dot{\phi} h}, K_{\ddot{\phi} h}) + H_{\phi \theta}(K_{\phi \theta}, K_{\dot{\phi} \theta}, K_{\ddot{\phi} \theta}) \\ \psi &= H_{\psi h}(K_{\psi h}, K_{\dot{\psi} h}, K_{\ddot{\psi} h}) + H_{\psi \theta}(K_{\psi \theta}, K_{\dot{\psi} \theta}, K_{\ddot{\psi} \theta}) \end{aligned} \quad (\text{A.32})$$

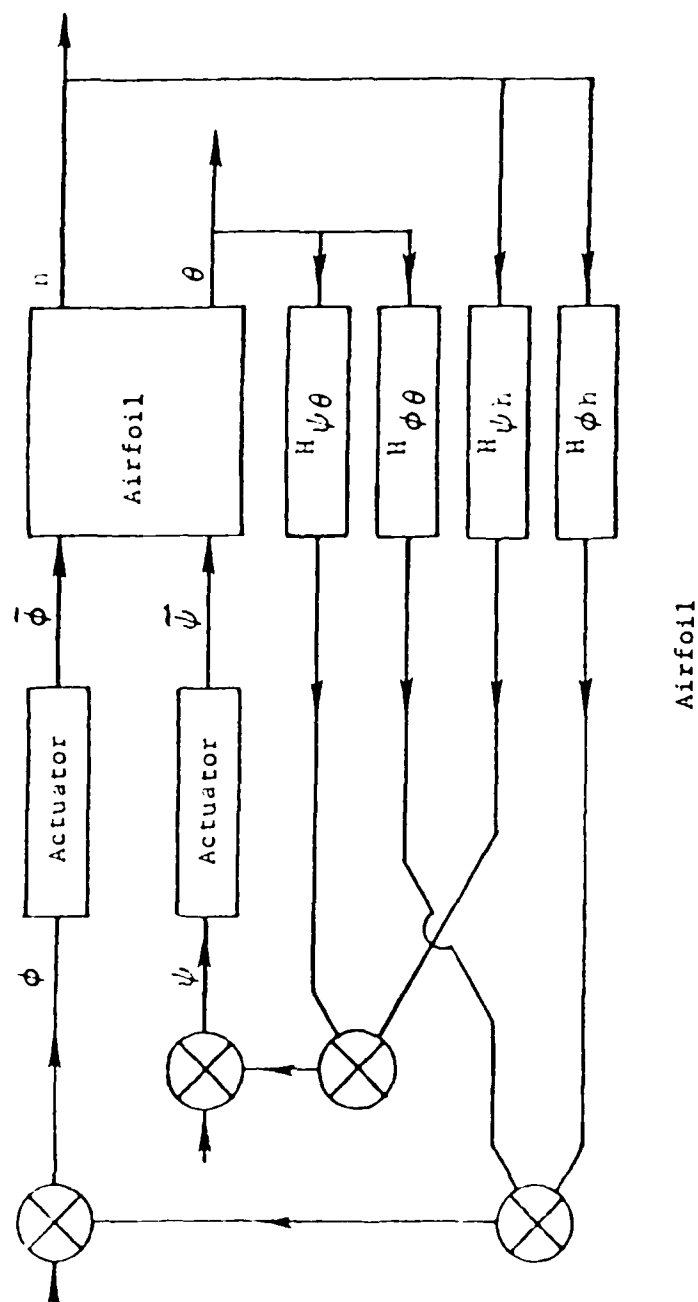


Figure A2 Feedback Loops For The Airfoil Compensation



In the specification of flap motion, the constants  $K_{ij}$  determine, the relative weight of the degrees-of-freedom and their derivatives. Mathematically, the constants represent gain settings used for linear amplifiers in the feedback loops of an actual control system. An example control law is shown in equation A.32. The relationship between the trailing-edge flap movement and the elastic-plunge displacement, velocity and acceleration are contained in  $H_{\phi h}$ . The gain constants  $K$  weigh the displacement, velocity, and acceleration in the  $H$  function.

$$H_{\phi h} = K_{\phi h} h + K_{\dot{\phi} h} \dot{h} + K_{\ddot{\phi} h} \ddot{h} \quad (A.33)$$

When the  $H_{\phi h}$  function is transformed into the complex plane, a quadratic compensation loop in the variable  $s$  results.

$$\bar{H}_{\phi h} = (K_{\phi h} + K_{\dot{\phi} h} s + K_{\ddot{\phi} h} s^2) \bar{h} \quad (A.34)$$

All of the feedback-control laws can be put in the form of equation A.34. With these control laws now posed as functions of  $s$ , these functions can be organized into a matrix form compatible with the displacement vector for the airfoil. For ease in combining these feedback loops with the transformed equations of motion, the terms of the polynomials (for the flap deflections in relation to the airfoil degrees-of-freedom) are organized in matrix notation.

$$\begin{Bmatrix} \bar{\phi} \\ \bar{\eta} \end{Bmatrix} = \begin{bmatrix} \bar{H}_{\phi h} & \bar{H}_{\phi \theta} \\ \bar{H}_{\eta h} & \bar{H}_{\eta \theta} \end{bmatrix} \begin{Bmatrix} \bar{h} \\ \bar{\theta} \end{Bmatrix} \quad (A.35)$$

Equation A.34 is combined with the equation of the flap's aerodynamic forces (equation A.31). For the equations of motion, the stabilizing forces can now be written in terms of the displacements of the airfoil.

$$\begin{Bmatrix} \bar{Q}_h \\ \bar{Q}_\theta \end{Bmatrix}_{\text{flap}} = \frac{1}{\bar{Q}_2 s^2 + \bar{Q}_1 s + 1} \begin{bmatrix} [P_3] s^3 & \cdots & [P_0] \\ \text{flap} & & \text{flap} \end{bmatrix} \begin{bmatrix} \bar{H}_{\phi h} & \bar{H}_{\phi \theta} \\ \bar{H}_{\eta h} & \bar{H}_{\eta \theta} \end{bmatrix} \begin{Bmatrix} \bar{h} \\ \bar{\theta} \end{Bmatrix} \quad (A.36)$$

The equation of motion for the airfoil (equation A.11) can now be written in terms of influence coefficient matrices made up of complex constants that can be used to pre-multiplying the airfoil.

### Solution Methods

The method for finding these roots (or poles) is dictated by the formulation of the aerodynamic forces in the equations of motion. When the damped aerodynamic forces are represented by Bessel functions (as in the Edwards' method for the airfoil), a search method is used to find values of  $s$  that make the characteristic determinant go to zero. When the damped aerodynamic forces are represented by the Padé Approximants, the roots of the characteristic determinant can be found, using standard eigenvalue routines that have been put on digital computers. Both of these methods are discussed for the airfoil.

### Edwards' Damped Aerodynamics

When using the Edwards' method for calculating the aerodynamics of damped airfoil motion, the value of  $\bar{C}(s)$  is needed to calculate the terms of the aerodynamic forces. But the desired value of  $s$  contains the root of the characteristic determinant. This determinant, however, can only be formed after the aerodynamic forces are calculated. Therefore, a value of  $s$  must be assumed so that the aerodynamics can be calculated. Then this  $s$  must be checked to see if it forces the determinant to zero. This procedure requires an iteration method to organize the search for the roots of the characteristic equation. The iteration method used here is an adaptation of the method used by Hassig (Ref. 30) in his  $p$ - $k$  approach for classical flutter solutions. In this determinant-iteration method, a regula falsi search algorithm (Ref. 26) calculates values of  $s$  that systematically drive the determinant to zero. The determinant-iteration process must be started with wing and flow conditions where the roots are known. The starting point used here is the in-vacuum vibration frequencies at zero flow velocity. Using these roots as initial estimates, parameters in the equations of motion can be slowly varied. Then the regula falsi search method guides the search for the roots. The loci of the roots with

selected parameter changes are thus constructed. By gradually increasing the parameter to be varied, the characteristic roots will change slowly and not confuse the regula falsi search algorithm.

The search procedure required to find each of the characteristic roots must be carefully programmed. Since the iteration method must search for each value of  $s$  that makes the characteristic determinant zero, sometimes many evaluations of the determinant are required to identify a root. Each determinant evaluation requires a calculation of the unsteady aerodynamic forces. But this procedure can involve large amounts of computer time if, for example, the velocity increments must be small enough to accommodate radical changes in the slopes of the loci. Radical slope changes occur, for example, when two complex conjugate roots coalesce into the real axis (break-in point) or leave the real axis (break-out). Another difficulty in this method is the possibility of overlooking a root. Sometimes, when several loci are near one another, the iteration method can mistakenly follow the wrong root loci. To avoid this problem, small velocity increments and close monitoring of the loci developments are required. The difficulty of tracking individual roots of loci that are very close can also be aggravated as the order of the equations increases. Sometimes, several vibration modes can have similar frequencies. This condition puts many roots near one another at low velocities.

#### Padé Approximant Damped Aerodynamics

When using the Padé Approximant method for calculating the airfoil aerodynamic forces, the polynomials of the approximations are in powers of the Laplace variable  $s$ . These constants, organized in the form of matrices of influence coefficients of equations A.27 and A.30, can be directly combined with the mass and stiffness matrices to form matrix equations of motion. The characteristic equation and the associated roots can be obtained by standard eigenvalue programs available on digital computers. The loci of the roots can be obtained then by choosing all gain and velocity variables and exercising standard eigenvalue routines.

### Method Applications

The calculations used to compare aerodynamic force formulations are the divergence and flutter predictions that these methods provide. The many combinations of magnitude and location of airfoil inertia and stiffness characteristics in Reference 16 allow a wide variety of comparisons to be made. While sweep angle has no direct meaning for the infinite-span airfoil, the relative locations of shear center and aerodynamic center can produce airfoils that have divergence as their most critical aeroelastic instability. These airfoils can be used as check cases representing the divergence-critical nature of forward-swept wings. The two aerodynamic force methods, the Edwards' method and the Padé Approximant method, are examined using two example cases. The Case D (for divergence) example has divergence as its most critical aeroelastic instability, and the Case F (for flutter) example has flutter as its most critical instability. The physical characteristics are defined in Figure A1 and the values used to describe these cases are given in Table A3.

#### Edwards' Method

Aerodynamic forces from Edwards' method are used in the airfoil stability calculations, illustrated in the velocity root loci of Figure A3. This velocity root locus shows the movement of the characteristic roots of Case D as a function of changes in freestream airspeed. Only the upper half of the complex plane is plotted because of the complex conjugate nature of the roots that have non-zero imaginary parts.

At zero airspeed, the roots lie on the imaginary axis. These axis locations correspond to the values of the natural vibration frequencies of the elastic structural modes. Vacuum vibration mode 1 of the airfoil Case D (whose motion is dominated by the plunge degree-of-freedom) has a natural frequency of 10 rad/sec. Therefore, the root locus having its zero velocity location on the imaginary axis at that value is referred to as mode 1. In similar fashion, reference is made to the mode 2 locus. Its zero velocity value is located on the imaginary axis at a value corresponding to the second vacuum vibration frequency, 25 rad/sec.

Table A4 Physical Characteristics Of The Airfoil Examples

	Case D	Case F
a	-.4	-.4
$r_\alpha$	.5	.5
$x_\alpha$	.05	.1
b ft	3.	3.
$\omega_\theta$ rad/sec	25.	25.
$\omega_h$ rad/sec	10.	10.
c	-.6	-.6
d	.6	.6
$\rho$ slugs/ft	.002378	.002378
$U_f$ ft/sec	224.	218.
$U_d$ ft/sec	188.	375.
$\mu$	5.	20.

$$\omega_h = (K_h/K_h)^{1/2}$$

$$\omega_\theta = (K_\theta/I_\theta)^{1/2}$$

$$\mu = K_h/(\pi \rho b^2)$$

$$r_\alpha = (I_\theta/(K_h b^2))^{1/2}$$

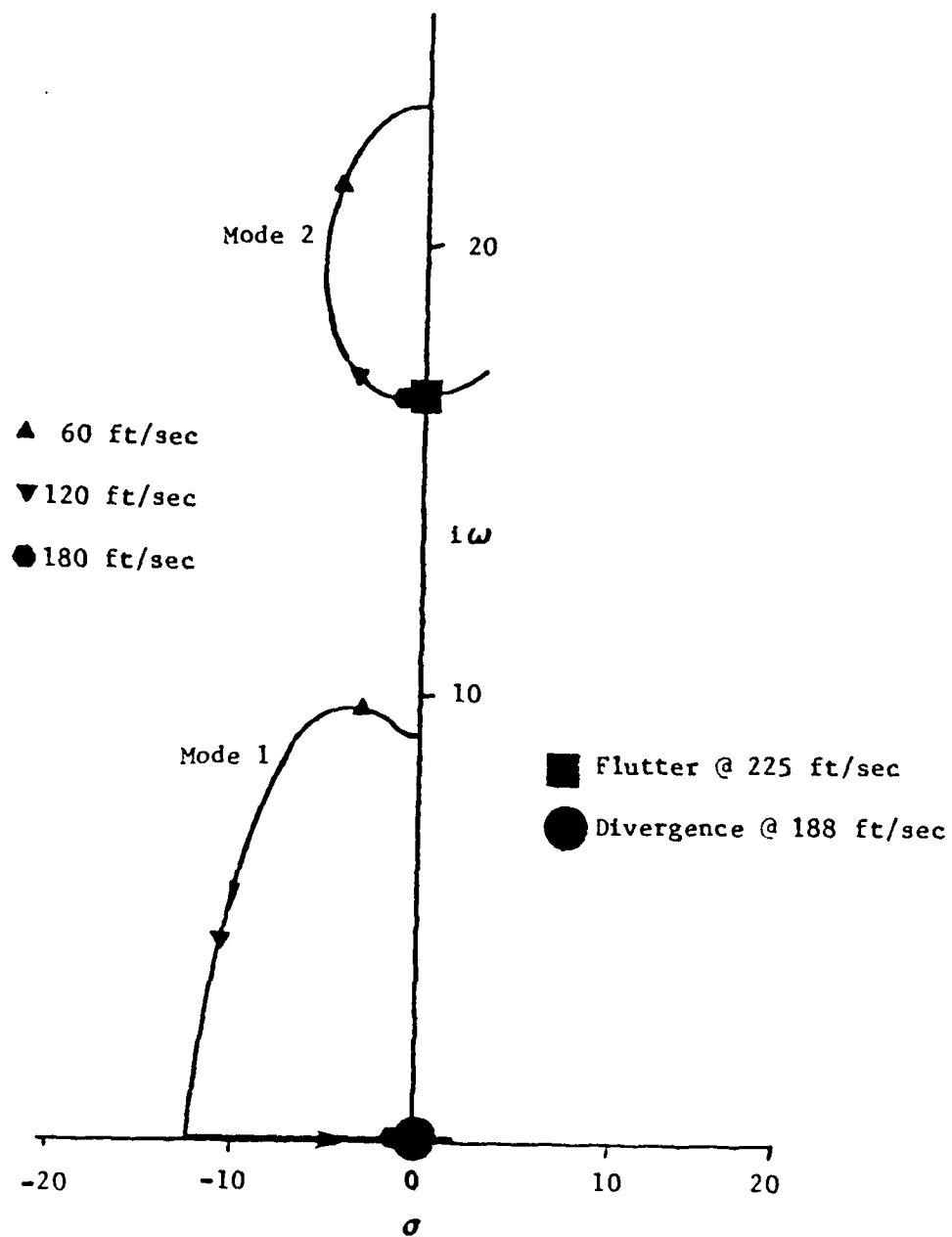


Figure A3 Velocity Root Locus For Case D  
No Feedback

As airspeed is increased, movement of the roots of mode 1 and mode 2 described basic patterns which are repeated throughout all the airfoil results. The plunge-dominated mode 1 shows a reduction in frequency by movements of its roots towards the real axis. At the same time, an increase in damping is shown by their movement to the left. Once the conjugate roots meet on the real axis (break-in point), one root moves in a positive direction along the real axis while the other root moves in a negative direction. At a velocity of 188 ft/sec, a root of the mode 1 root pair crossed the imaginary axis, moving towards the right (negative damping direction). The airspeed at this crossing is defined as  $U_d$ . A similar pattern in the mode 1 loci is repeated with all the airfoil (and later, the wing) examples. That is, the divergence velocity is defined by a root that began as the lowest frequency vibration mode dominated by plunge motion when velocity was zero.

The second complex conjugate pair of roots move such that as airspeed is increased, damping is first gained, then later lost. This is shown by the movement at first to the left and then back right towards the imaginary axis. Damping finally becomes negative as the roots cross the imaginary axis at  $U_f$ . Because this imaginary axis crossing occurs with non-zero imaginary parts, the crossing defines flutter rather than divergence. The airfoil experiences flutter at a velocity of 225 ft/sec. The pattern for this root locus defining flutter is typical for the other examples of flutter. All the loci defining flutter have roots at zero freestream velocity with a frequency of the first torsional (pitch dominated) mode. Both the divergence- and flutter- critical airspeeds for Case D, using the Edwards' method for aerodynamic forces, agree with airspeeds that are predicted by the solutions of Reference 2.

The stability characteristics of Case F are described graphically by the velocity root locus of Figure A4. The divergence instability is again defined by the roots of mode 1, now at an airspeed of 375 ft/sec, while the roots of mode 2 define flutter at an airspeed of 218 ft/sec. Again the Edwards' method for aerodynamics agree with the solutions of Reference 2.

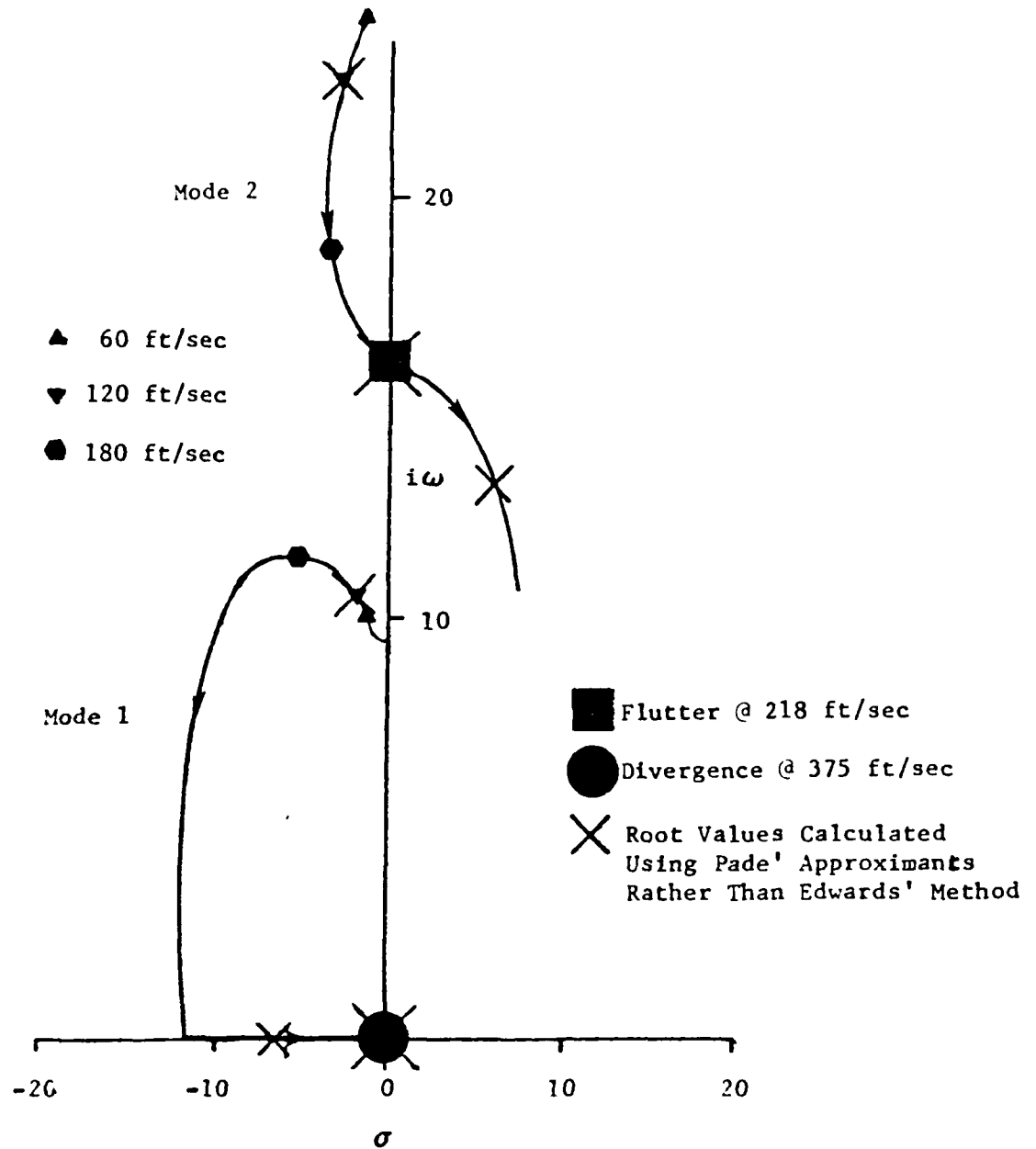


Figure A4 Velocity Root Locus For Case F  
No Feedback



With the proper prediction shown for the instabilities without active controls, the investigation into possible feedback control loops can be made. By actuating the trailing-edge flap proportionally as a function of the plunge deflection of the airfoil, the velocity root locus of Case D (shown in Figure A5) is calculated. Here the plunge signal is multiplied by a simple gain value chosen to be  $.1 \text{ rad/in.}$  This positive-feedback signal drops the divergence velocity from a value of  $188 \text{ ft/sec}$  (without controls) to  $121 \text{ ft/sec}$  (with controls). Along with this, the shape of the locus of mode 2 has been changed drastically.

The Case D velocity root locus can be further modified with active control if the flap is deflected proportionally to the negative of the pitch angle of the airfoil. Figure A6 shows a velocity root locus for this feedback loop at a gain value of  $-.1 \text{ rad/in.}$  Flutter has now been lowered to  $121 \text{ ft/sec}$ , but divergence is absent.

Figures A7 and A8 show similar modifications to the velocity root locus of Case F. The leading edge flap deflection is related to the plunge deflection by a gain of  $.1 \text{ rad/in.}$ , using positive feedback for Figure A7 and negative feedback for Figure A8. Note that the flutter speed is strongly influenced by the sign of the feedback signal.

The determinant iteration method of obtaining roots works well for these simple airfoil configurations. Realistic subcritical damping and frequency information is obtained by using the Edwards' method for forces from damped airfoil motion. But a basic difficulty arises with this method. The regula falsi scheme for new root prediction can easily become confused when discontinuous changes occur in the root loci. Considerable logic must be included in the computer routines of this method to deal with discontinuities. This situation is especially difficult where complex conjugate roots move to the real axis at a break-in point. At these points, the roots split in positive and negative real directions. When this split occurs, the estimation and refinement process of the regula falsi scheme must be artificially forced to examine (for higher velocity

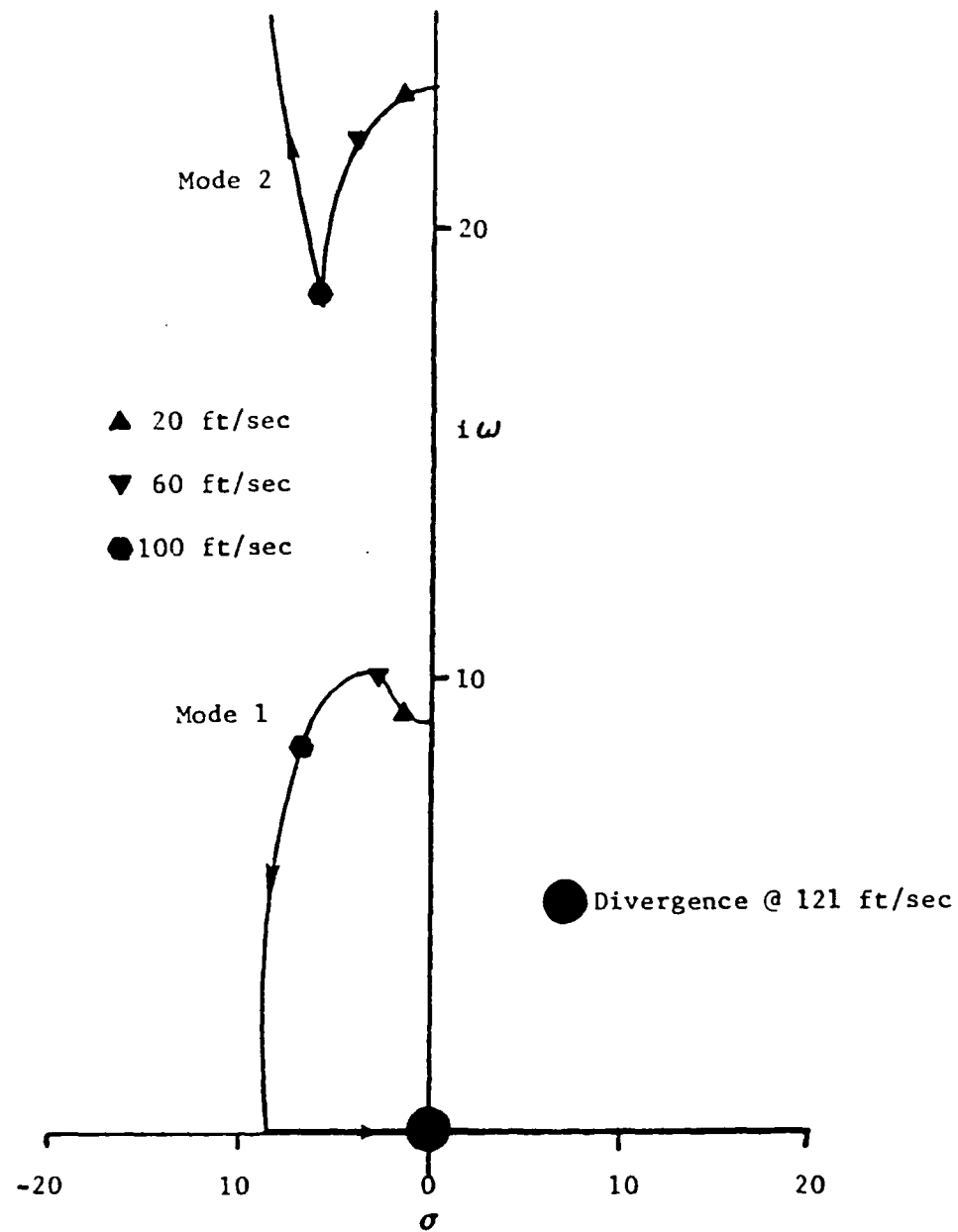


Figure A5 Velocity Root Locus For Case D  
 $K_{\phi h} = .1 \text{ rad/in}$

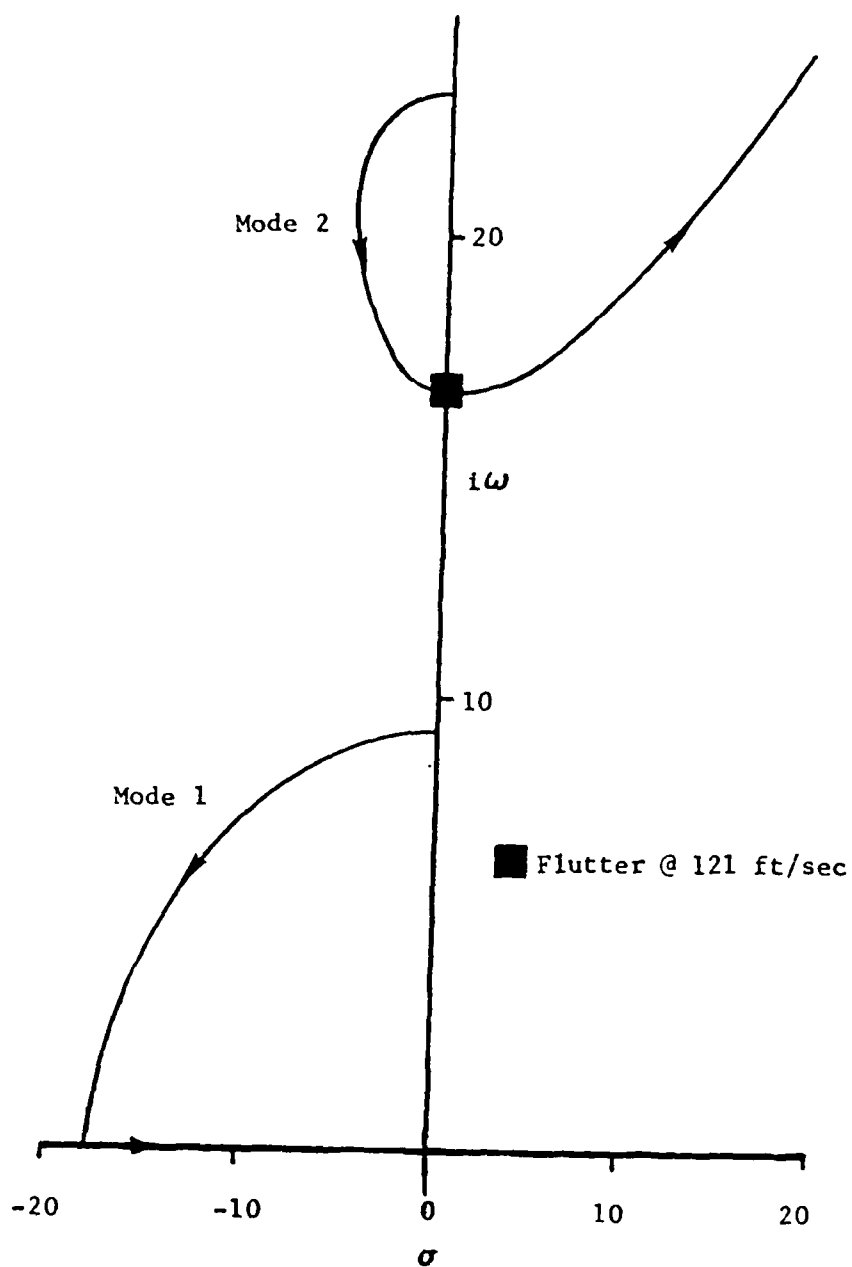


Figure A6 Velocity Root Locus For Case D  
 $K_{\phi h} = -.1 \text{ rad/in}$

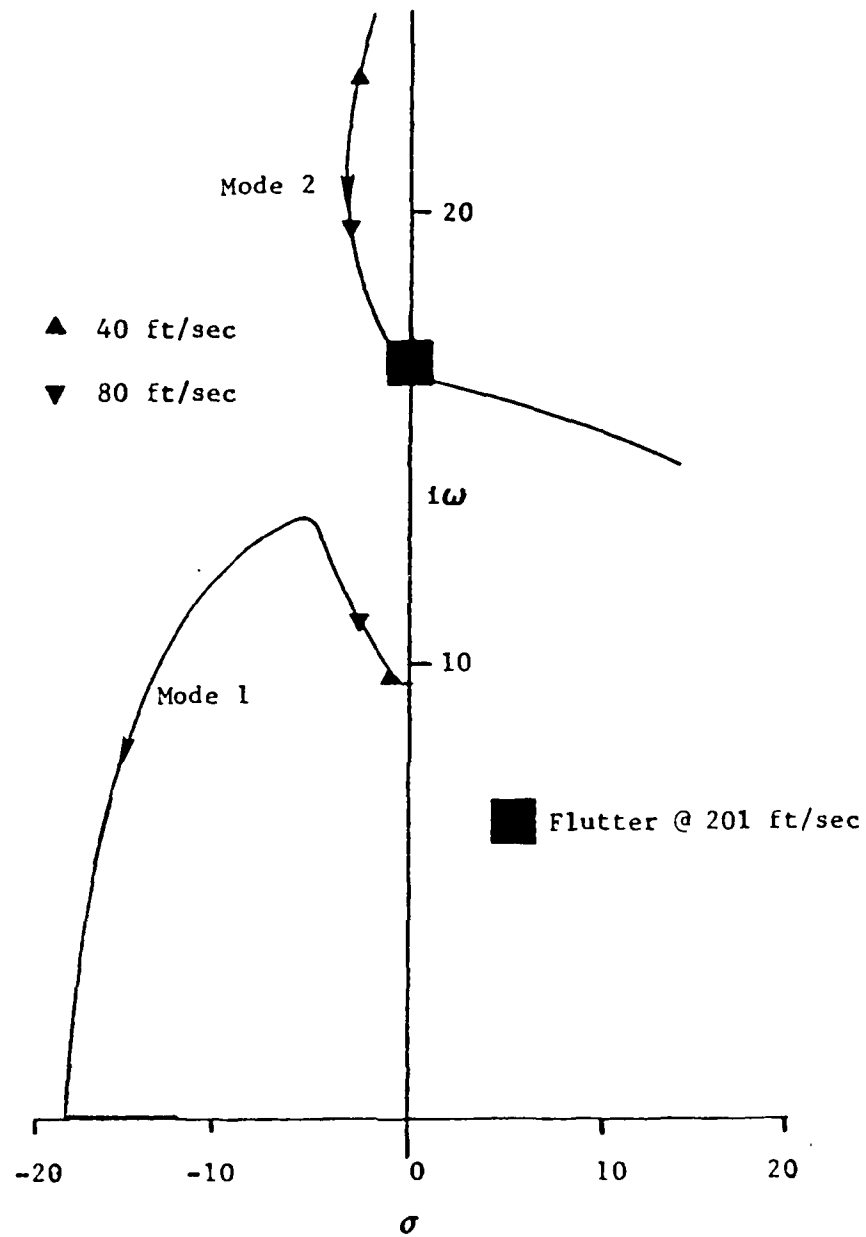


Figure A7 Velocity Root Locus For Case F  
 $K_{ph} = .1 \text{ rad/in}$

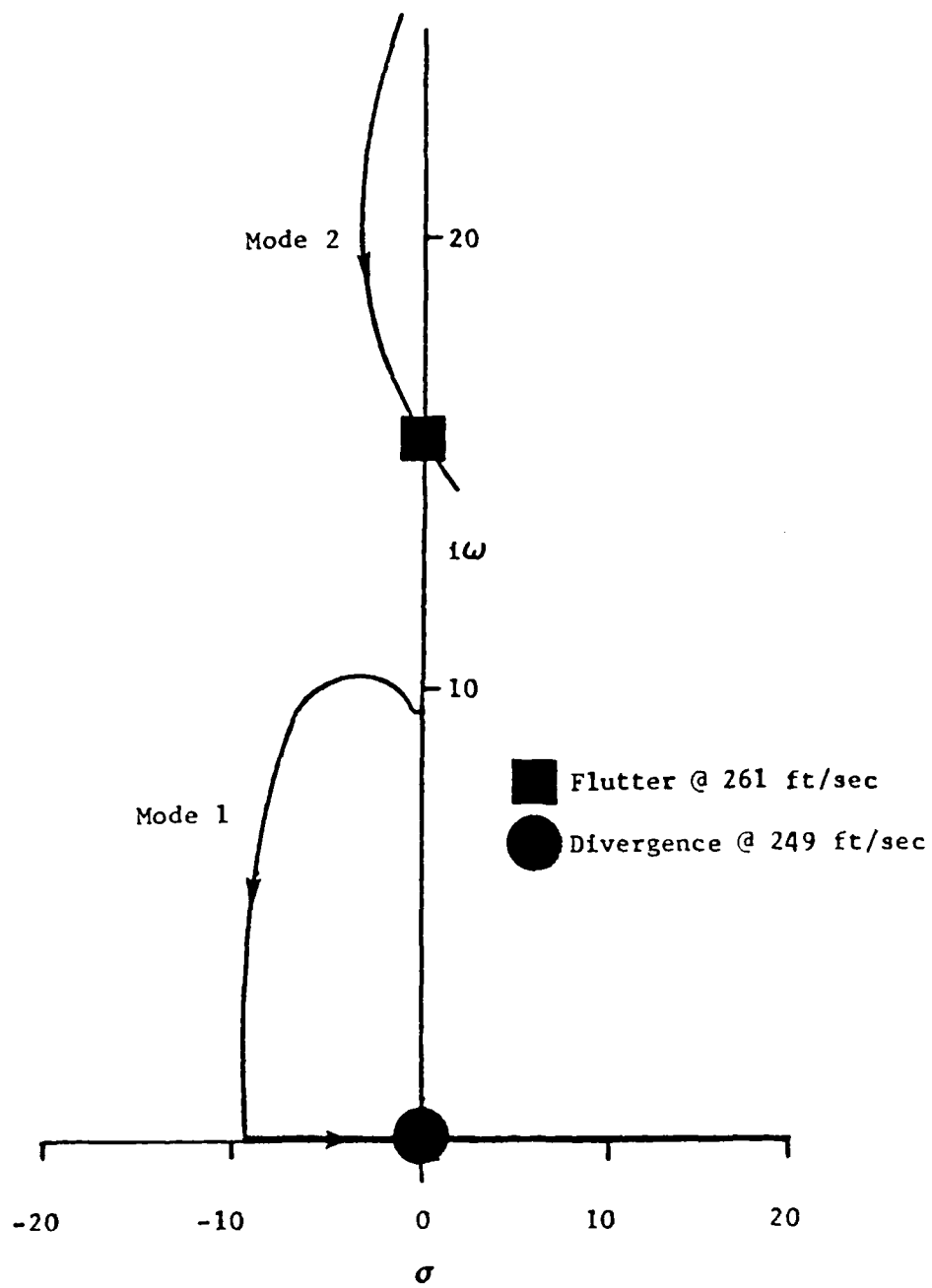


Figure A8 Velocity Root Locus For Case F  
 $K_{ph} = -.1 \text{ rad/in}$

roots) only the real axis and not project into the non-zero imaginary coordinate space for the higher velocity roots. At these points of possible confusion in the process of generating the root loci, the process generally requires monitoring of the computer development of the loci by the investigator, and very small steps in velocity must be imposed to prevent the roots from changing too much from step to step. Since the aerodynamic forces are evaluated at each velocity step, these small steps in velocity require many evaluations of the aerodynamic forces. These evaluations can result in unacceptable expense for any stability problem larger than this two degree-of-freedom airfoil.

Similar care must be exercised when roots pass close to one another in their loci. In these instances, the regula falsi method tends to jump at times from one root locus to another nearby. As more degrees-of-freedom are introduced into the equations, this jumping from one locus to another becomes more of a problem (configurations with many modal frequencies in close proximity cause this difficulty, such as large bomber and transport wings). The regula falsi search requires very small increments in velocity, sometimes increments as small as 1 ft/sec.

#### Padé Approximant Method

The airfoil is also used to confirm the ability of the Padé Approximant aerodynamics to predict flutter and divergence. This method permits the selection of any velocity range for the root loci without the requirement to start from velocities with known root values. Therefore, only a small number of velocities in the vicinity of  $U_d$  and  $U_f$  are used for the airfoil cases.

Recall that Figure A4 presents the velocity locus for Case F when no active control is present. The locus lines are drawn using the Edwards' method for the aerodynamics. Located with the letter X on these loci are sample root locations calculated using the Padé Approximants aerodynamics. These root locations are representative of several correlation checks made between the Padé Approximants and the Edwards' method. Exact agreement is

shown by the Padé roots with the loci calculated by Edwards' method. Therefore, the Padé Approximants' economy of calculation can be exploited in lieu of Edwards' method, without loss of accuracy at these low levels of damping.

### Evaluation

The results from the airfoil examples suggest that the best method for calculating aerodynamic loads of the wing examples is by use of the Padé Approximants. Using this method, the aerodynamic loads must be calculated for a small number of frequencies only once to perform the squares fitting process. Any range of velocities can be used in the calculations of the root loci since the regula falsi search is not required. Finally, there is no possibility of losing a root since all eigenvalues are calculated at each freestream airspeed. The limitations of this method evolve from the fitting process needed to establish a useful relationship between the motion of the lifting surfaces and the resulting aerodynamic forces. Extra roots are introduced into the equations of motion from the denominator of the Padé polynomials. For proper predictions of critical airspeed, the force data used for the fitting process must be purely sinusoidal. Thus, calculations for highly damped motion can lose accuracy because the aerodynamic force approximations are developed using zero damping motion. Perhaps most disturbing is the possibility of roots from the equations of motion with positive real parts, caused only by the aerodynamic force approximations (Ref. 22). If the least-squares fitting for the Padé Approximants produces a denominator that has roots that have positive real parts an instability would exist in the airloads themselves, which should not occur in nature. Fortunately, for the wing examples used in these studies, no positive roots from the airloads' approximations were calculated.

## APPENDIX B

### The Doublet-Lattice Method

The application of the doublet-lattice method is the first step in calculating aerodynamic forces due to damped motion of a forward-swept wing. This method is applicable to the forward sweep geometry and provides for control surfaces on the wing planform. The following is a brief description of this sub-sonic compressible flow method.

The doublet-lattice method provides a small-disturbance solution for unsteady airloads of arbitrary three-dimensional wings (Ref. 18). This solution is calculated using an array of doublet singularities that satisfy the small perturbation acceleration potential equations. The acceleration potential is used to simplify the specification of singularities that represent the wing. The desired specifications for the near field boundary conditions are downwash values on the wing planform. By assuming simple harmonic motion the magnitude of the downwash  $|w(x,y)|$  at  $x,y$  due to a sinusoidal pressure difference  $|\Delta p(\eta,\xi)|$  at  $\eta,\xi$  can be calculated using equation B.1.

$$|w(x,y)| = -(4\pi\rho U)^{-1} \iint |\Delta p(\eta,\xi)| \mathcal{K}(x-\eta,y,\xi,\omega,M) d\eta d\xi \quad (B.1)$$

Here the kernel of the integral is a function of geometry, oscillation frequency, and Mach Number. The doublet-lattice procedure uses an array of doublets to provide the pressure difference over the wing planform. Their strength can be defined when their downwash from equation B.1 is required to match the downwash field of a wing. The  $\Delta p$  pressures then provide the forces on the wing planform.



In Figure 4 the doublet-lattice idealization is presented for the cantilever wing used here in the active control calculations. An example of one of these doublet-lattice panels is shown in Figure B1. In Figure B1 the line of doublets, the force point, and the control point are also marked. In order to properly array the singularities and control points to avoid numerical singularities the boxes must be oriented to have streamwise edges but may have arbitrarily swept leading or trailing edges. The panels become the basic geometric building blocks for the idealization of lifting surfaces.

The paneling technique provides an orderly way to array the doublet singularities and specification points for boundary conditions (control points) to represent the wing. As shown in Figure B1 each panel contains an array of doublets along the quarter chord that have a parabolic strength distribution along the line. Their strength is zero at the ends of the line. An arbitrary constant scales their absolute value interior to the line endpoints. The force point is the point of application of the resultant force created by the doublets moving through the freestream flow. It is located at the mid-span quarter chord position of the panel. Each panel also has a control point for prescribing boundary conditions. The downwash from the entire wing doublet array must match the actual wing downwash at the control point. This control point is at the mid-span three-quarter chord location of the panel. Thus each panel needs one value to be specified (the strength of the doublets) and supplies one downwash boundary condition. The doublet strengths can be determined uniquely when all of the downwash values are specified. These are determined when the wing motion (such as the vibration mode shapes) is prescribed at each control point.

The doublet-lattice computer program calculates the influence of each panel on the other panels and stores these. When combined with the panel areas, the result is an influence coefficient matrix. Since the doublet-lattice method is linear, this influence coefficient matrix is stored and can be used repeatedly to calculate loads for any wing motion that occurs at the frequency for which the matrix is calculated.

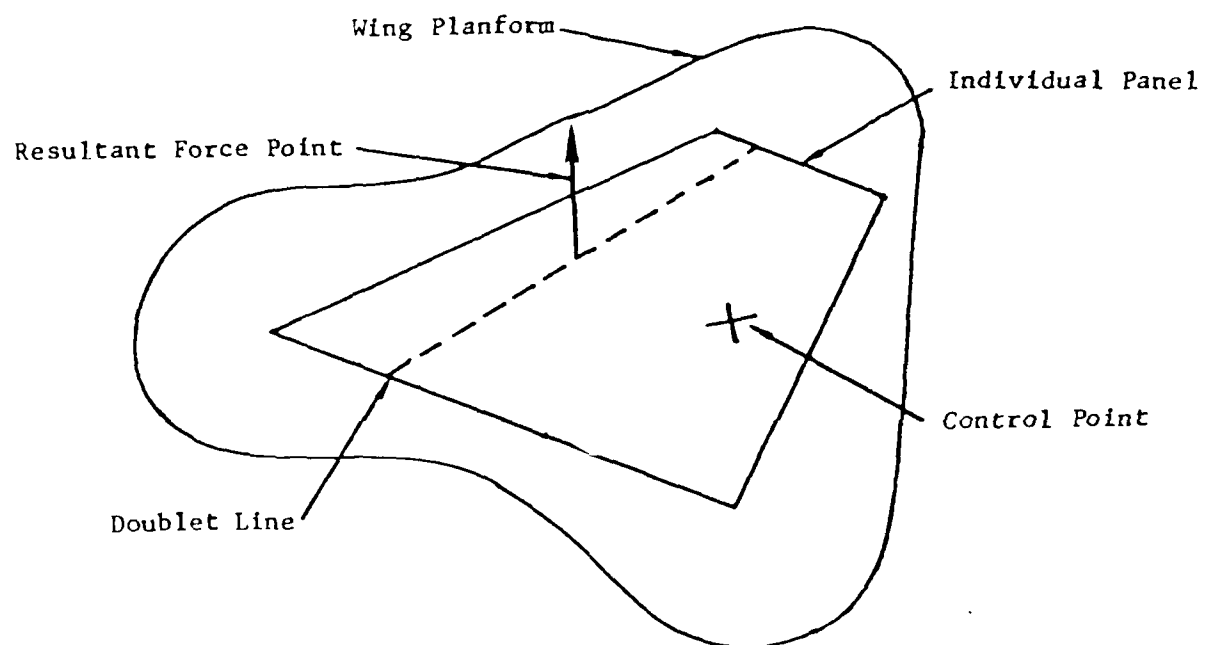


Figure B1 Typical Doublet-Lattice Panel

## APPENDIX C

### Wind Tunnel Correlations

The following presents comparisons between wind tunnel experiments and Padé Approximant predictions of forward-swept wing stability. The ability of analyses using Padé Approximant based aerodynamics to predict aeroelastic instabilities of forward-swept wings, especially divergence, is validated by the following correlations with wind-tunnel tests. Flutter-prediction capabilities for Padé Approximants have previously been established in Reference 13. However, the research documented here is the first application of Padé Approximants for the prediction of aeroelastic divergence. The Air Force Wright Aeronautical Laboratories (AFWAL) developed divergence wind-tunnel data using flexible, forward-swept, cantilever wing models in the subsonic wind tunnel at the Air Force Institute of Technology (Ref. 32). These test data are used to validate the use of Padé Approximants for divergence.

The wind-tunnel models use composite plates to represent several variations of full-scale wing-box construction. These model wings are constructed to produce different structural elastic couplings in deformation under load. These different couplings provide variations in divergence airspeeds for the same sweep angle of the model wing. When the variations of sweep angle are included with the structural variations, these data provide several examples with which to compare analytic divergence predictions. The model geometry is pictured in Figure C1. Shown in the picture is the cantilever root attachment which is mounted to the wind-tunnel roof during the tests. Also pictured are three different structural plates. The aerodynamic (but non-structural) fairing that covers these plates is shown at the top of the picture, with the wind tunnel attachment bracketry in place at the wing root. The fairing maintains the proper airfoil shape while allowing freedom for deformations

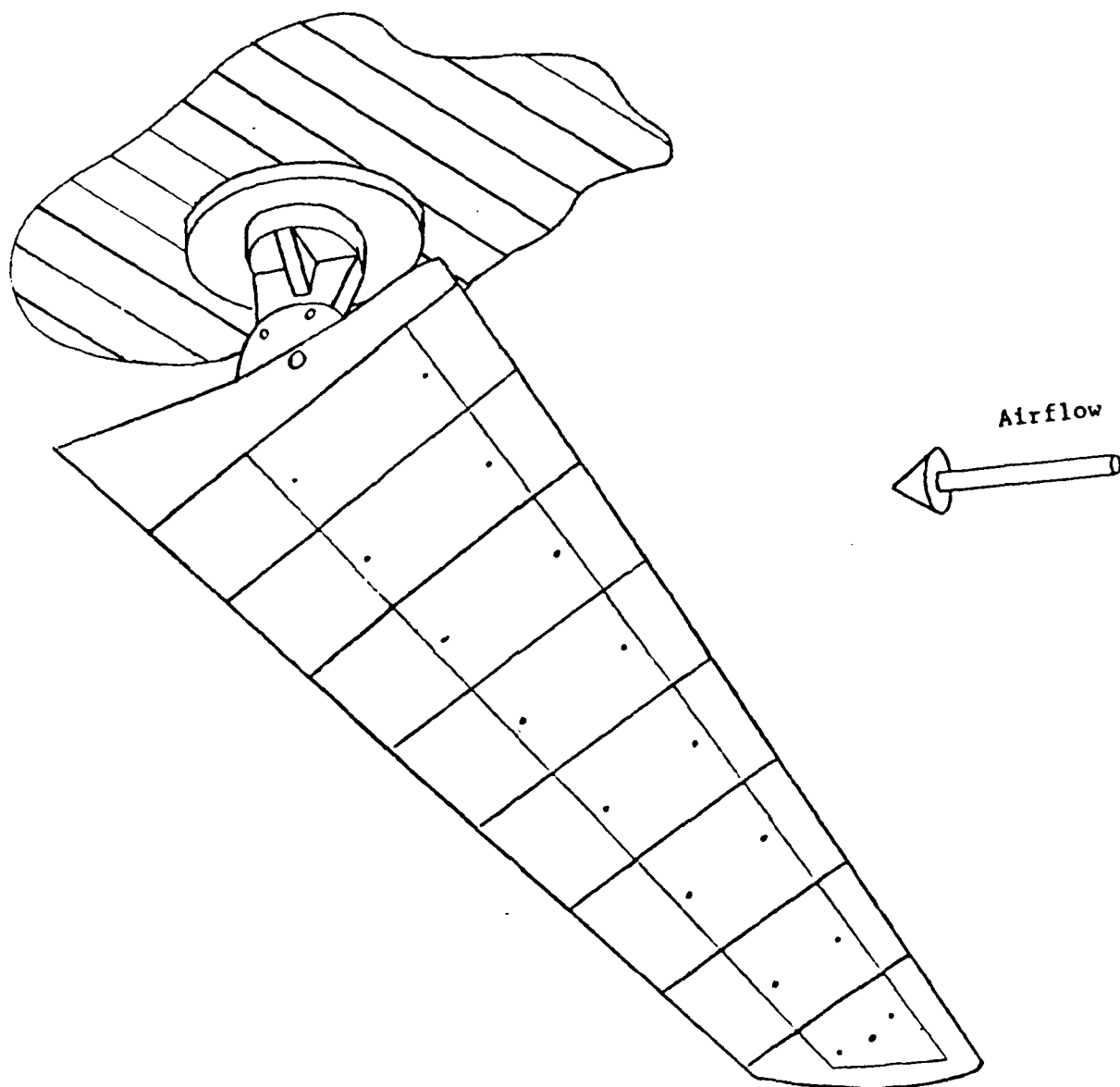


Figure C1 Wind Tunnel Model

Table C1 Wind Tunnel Model Comparisons: Test Versus Analyses

$\Delta^k$ (deg)	$\Delta$ (deg)	$q_d$ (lb/in <sup>2</sup> )				Difference* %
		Test	Pade'	NASTRAN	TSO	Pade' vrs. Test
0	-15	11.9	12.9	12.8	12.8	-8
0	-30	10.3	10.4	10.3	10.3	-1
0	-45	9.7	10.	10.	10	-2.5
15	-15	Vague	21.4	21.4	21.4	
15	-30	12.2	11.3	11.3	11.3	7
15	-45	10.	9.3	9.3	9.3	7

\* Between Results Of Tests And Pade Predictions

in the internal structural plates. The root attachment fitting allows adjustments of the leading-edge sweep to various negative sweep angles without changing the elastic characteristic of the flexible wing. The internal plates providing the structural stiffness for the wings are constructed using layers of graphite/epoxy material. These layers contain unidirectional graphite fibers in an epoxy matrix. The layers are laminated together with each layer providing a different fiber direction. The relative angles the fibers make with the mid-chord line of the wing define the basic layup of that structural plate. For these tests, the different plates constructed for the model are fabricated using variations of a basic layup of  $0^\circ/+45^\circ/-45^\circ$ . These fiber directions are measured with respect to the wing's leading edge. The variations are made by rotating the  $0^\circ/+45^\circ/-45^\circ$  layup by a small angle (called the kick angle  $\Delta_k$ ) with respect to the wing's leading edge. Thus, a layup that has a  $7.5^\circ$  kick angle is a layup that has fiber angles of  $-7.5^\circ/-37.5^\circ/+52.5^\circ$  with respect to the wing's leading edge. As this kick angle is changed, the deformation coupling between wing bending and torsion also changes, producing a corresponding change in the critical airspeeds for flutter and divergence.

The test results for two model internal plates, each tested at three leading-edge sweep-angle settings, are presented in Table C1. The data represent comparisons between wind-tunnel test data and the dynamic pressure at divergence,  $q_d$ , calculated with three analytic techniques. The first technique presented uses the Padé Approximant method, which is the basis for the calculations in this research. The second is the finite-element structural- and doublet-lattice aerodynamic program NASTRAN (Ref. 33). The third method is the continuous-plate structural- and doublet-lattice aerodynamic program TSO (Ref. 34). The last column lists the percentage differences between the Padé Approximant method and the wind-tunnel test values for  $q_d$ . Along with the table, some examples are included of the root locus plots from the Padé Approximant stability calculations for these models. These examples show the effect that sweep-angle changes have on the sub-critical damping of the roots.

Noting the comparisons of the various methods in Table C1, a maximum error of 8% is shown between tests and the predictions made with the Padé Approximant aerodynamics. These approximations use results from the doublet-lattice method as a basis for their least-squares fitting. But errors of up to 10% using doublet-lattice are considered acceptable. Since the Padé Approximants provide predictions that are equal to or better than what is considered acceptable for the method on which they are based, the Padé Approximants provide an acceptable analytical model for the aerodynamic forces.

Figure C2 is the velocity root-locus plot for the model configuration with  $\Lambda_k$  of  $0^\circ$ . The leading-edge sweep is  $-15^\circ$ , with the in-vacuum frequencies for the structural vibration modes appearing at root locations on the imaginary axis. Mode 1 is the first wing-bending mode at 3.51 rad/sec; mode 2 is the second wing-bending mode at 17.68 rad/sec; mode 3 is the first wing torsion at 27.29 rad/sec; and mode 4 is the third wing bending at 44.96 rad/sec. In this figure, the divergence condition is defined with a zero-frequency modal crossing of the imaginary axis by the mode 1 root at a dynamic pressure of  $12.9 \text{ lbs/in}^2$ . This instability is followed at a higher freestream flow velocity by a flutter instability indicated by mode 3. Again the modes defining both flutter and divergence in this root locus illustrate root-locus characteristics which are found in all root-loci examples of this research that contain no feedback circuits. The divergence condition is defined by the mode whose zero airspeed ancestry is the lowest frequency bending mode. The flutter condition is defined by a mode whose zero airspeed ancestry is the torsion mode of lowest frequency. In this example,  $q_d$  is smaller than  $q_f$  so the wind-tunnel model exhibited aeroelastic divergence in test, with the flutter instability not observed.

Figures C3 through C5 present root locus calculations using Padé Approximants of the wind-tunnel model with a  $\Lambda_k$  of  $15^\circ$ . In Figure C1, the model is mounted with a  $\Lambda$  of  $-15^\circ$ ; Figure C2 presents the same wing model with a  $\Lambda$  of  $-30^\circ$ ; and Figure C3 has this model at a  $\Lambda$  of  $-45^\circ$ . In all

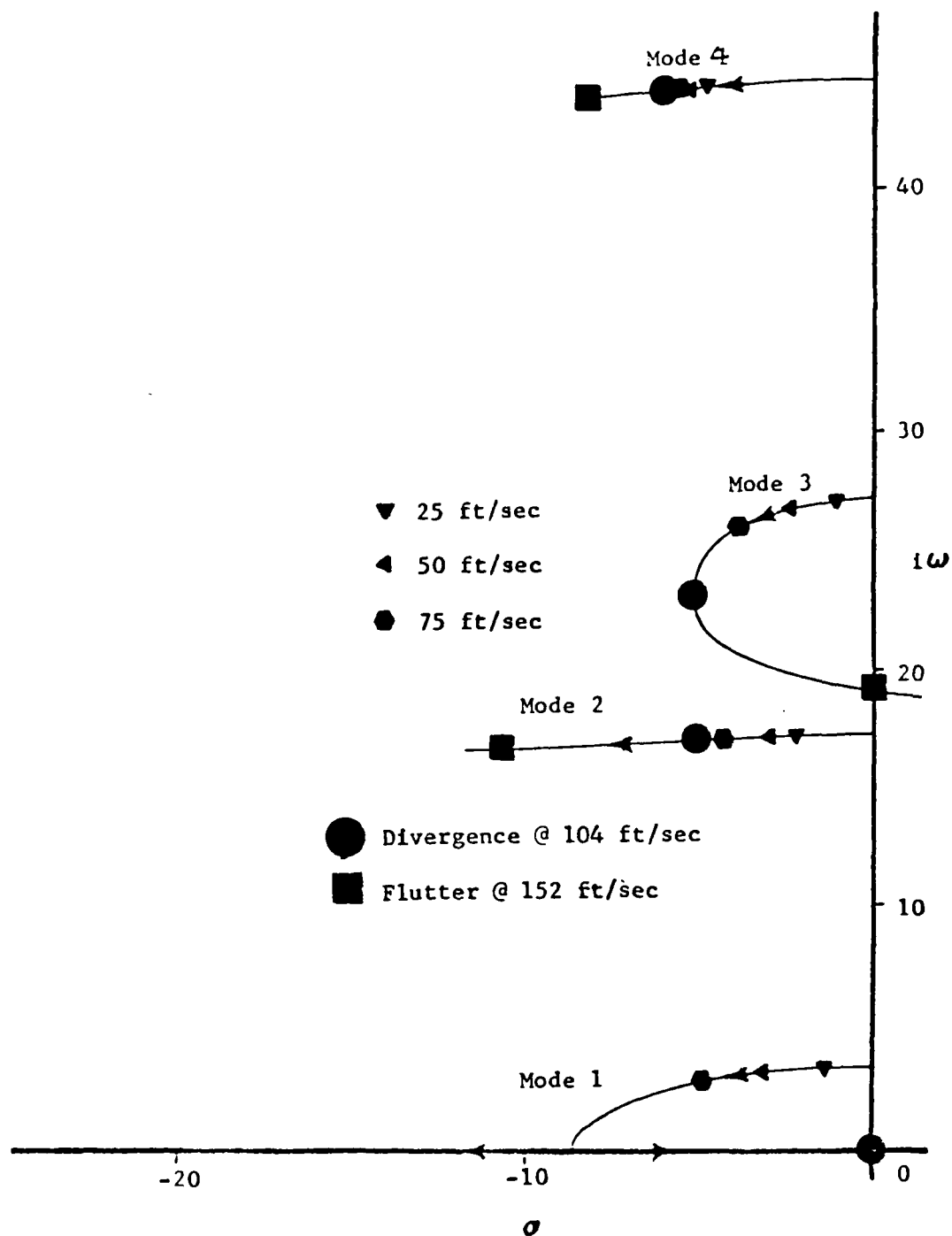


Figure C2 Velocity Root Locus For Wind Tunnel Model  
 $\Delta_k = 0^\circ$   $\Delta = -15^\circ$



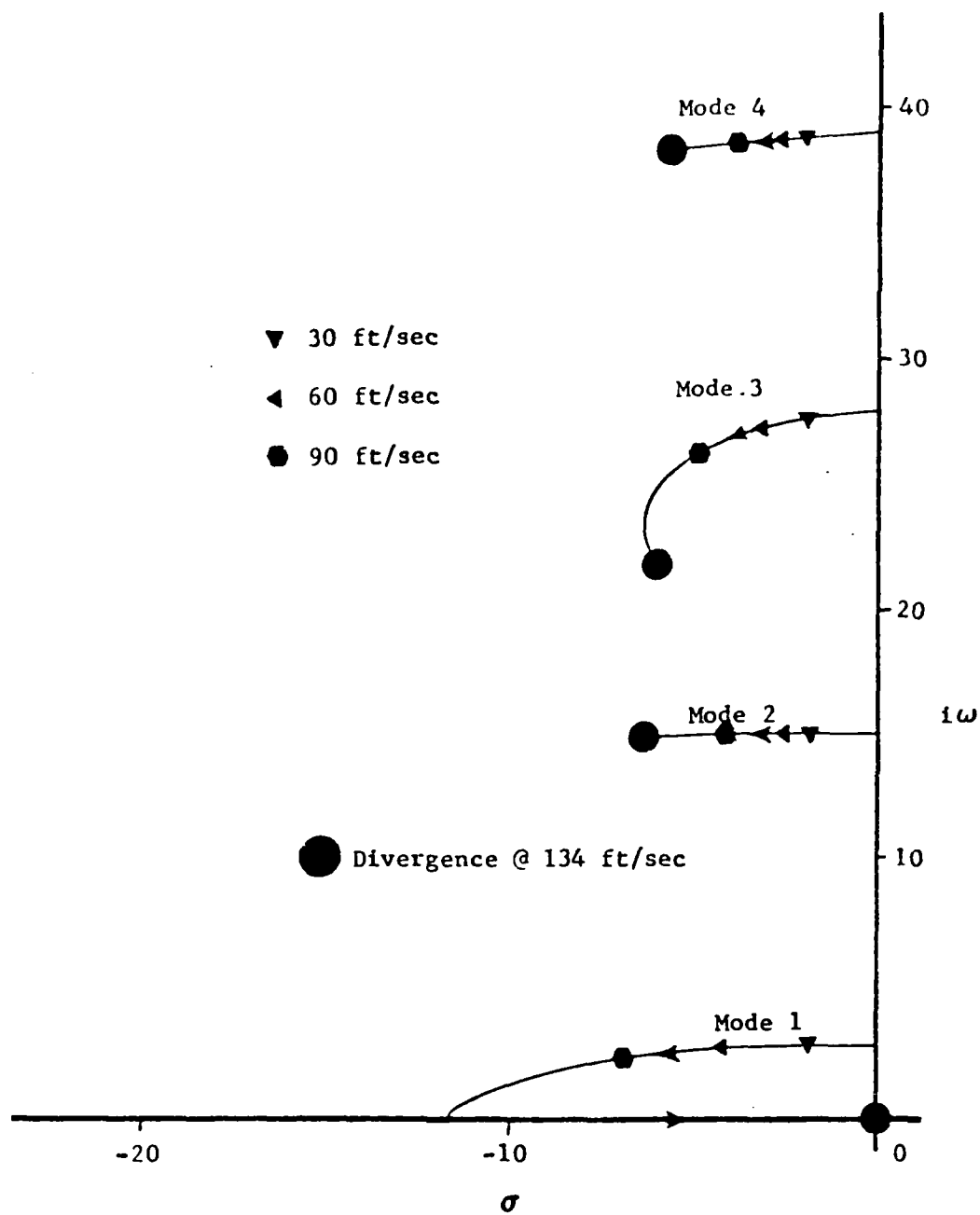


Figure C3 Velocity Root Locus For Wind Tunnel Model  
 $\Lambda_k = 15^\circ$   $\Lambda = -15^\circ$

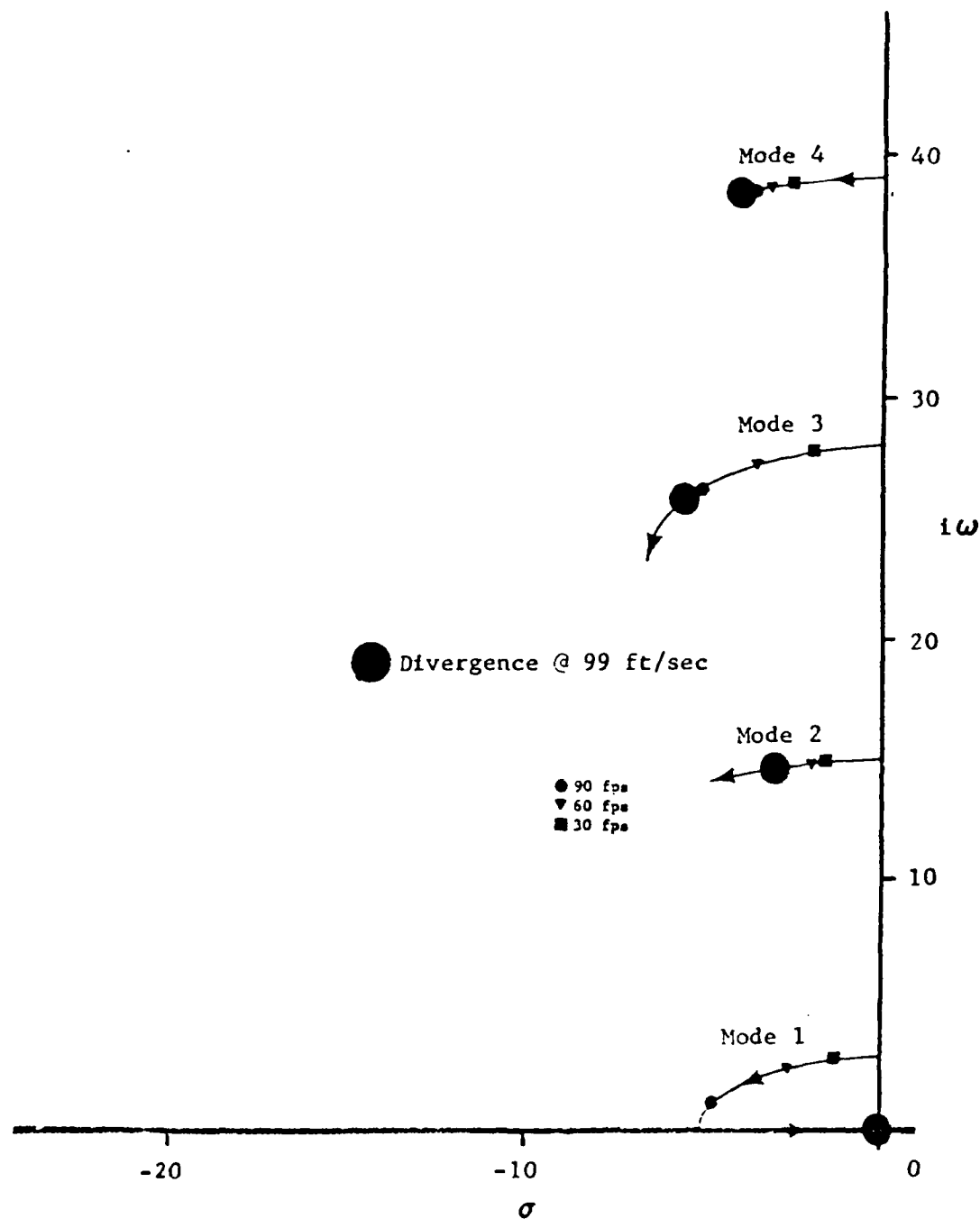


Figure C4 Velocity Root Locus For Wind Tunnel Model  
 $\Lambda_k = 15^\circ$   $\Lambda = -30^\circ$

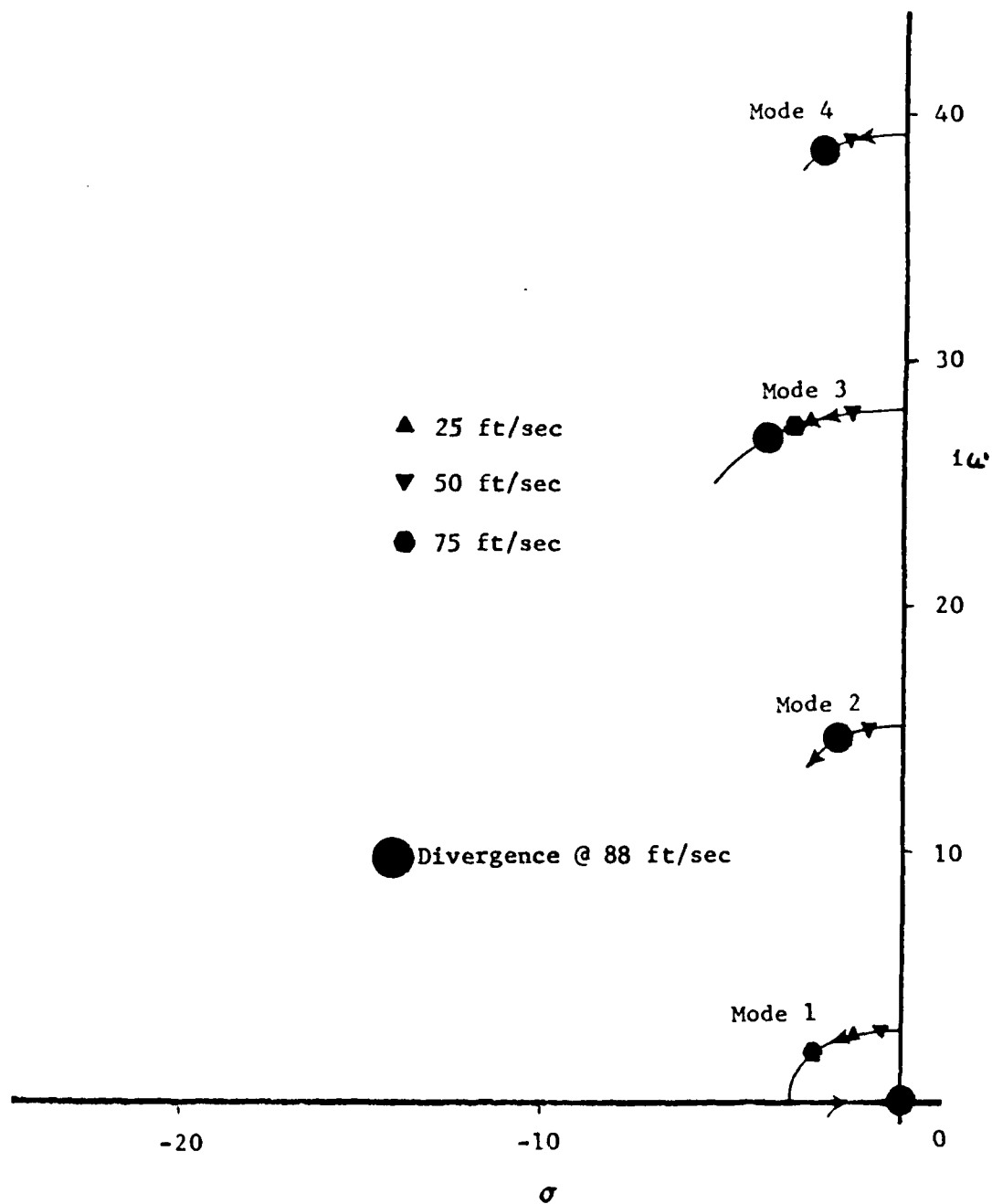


Figure C5 Velocity Root Locus For Wind Tunnel Model  
 $\Lambda_k = 15^\circ$        $\Lambda = -45^\circ$

three sweep configurations, the most critical aeroelastic instability predicted (and observed in testing) is divergence.

By comparing Figures C3 through C5, the changes in the root loci (due to progressive increases in negative leading-edge sweep) are evident. As the leading edge becomes more forward-swept, both the root locus associated with divergence and the root locus associated with flutter show changes. As the forward sweep is increased, the break-in location of the mode 1 roots moves progressively towards the imaginary axis, and the divergence velocity also decreases. Also, with increased forward sweep, the curvature of the locus for mode 3 decreases. This is the mode that would define the most critical flutter speed if the airspeed were sufficiently increased. This change in curvature suggests that the flutter instability should occur at progressively higher flow speeds for forward sweep angles.

The changes in sweep angle of the model are aerodynamic only and do not change the model's stiffness. Because the wing is cantilevered at the pivot-attachment (essentially rigid) outboard of the pivot pin, changes in the vacuum vibration modes are not measurable as the leading-edge sweep changes. Thus, sweep angle effects on the model's aeroelastic characteristics are due only to the aerodynamic sensitivity to sweep.

Even though the vibration modes and frequencies of the model wings do not change with sweep, sweep does effect the elastic contributions of the wing to the aeroelastic instabilities. For example, as loads increase, and the wing bends under these loads, this bending produces more and more angle-of-attack changes at each span station as wing sweep increases. This condition is shown in Figure C6. These angle-of-attack changes can either be positive or negative, depending on whether the sweep is negative or positive. The effects of torsional deformation on local angles-of-attack are also similarly modified by sweep. These changes due to sweep suggest an explanation for the test point at  $\Lambda$  of  $-15^\circ$  and  $\Lambda_k$  of  $15^\circ$ . A vagueness in the type of response is demonstrated by the model at this test condition. The model did not diverge, nor did it flutter. It exhibited an

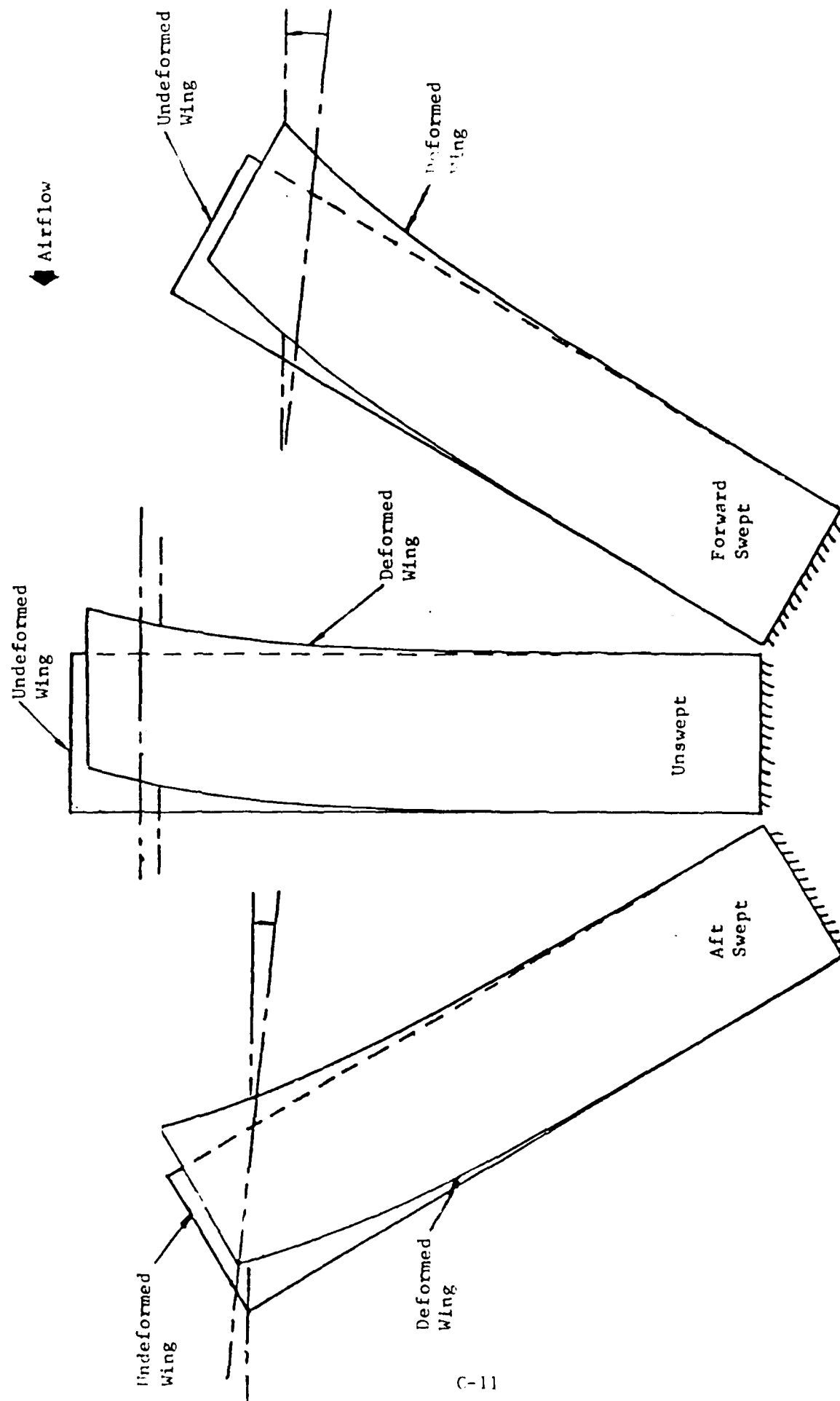


Figure C6 Sweep Effects On Section Angles-Of-Attack Due To Wing Loading

irregular random movement that fit neither of the above descriptions. Now, at large values of forward sweep, the wing deflection at divergence is primary bending. As the forward sweep is reduced, the wing deflection at divergence contains more torsional deformation. At some low value of forward sweep, the importance in divergence of primary bending deformation versus primary torsion deformations reverses. It appears this transition may be occurring at the  $-15^\circ$  sweep condition with a  $\Lambda_k$  of  $15^\circ$  for the wind-tunnel model. To investigate this vague test point further, the rate of change of damping (with changes of velocity at the onset of aeroelastic divergence) is examined as sweep is changed.

A way of describing the rate at which the loss of stability occurs with increases in velocity is the degree of explosiveness of the instability. Classical bending-torsion wing flutter has the property that the system goes from a very stable to a very unstable system with only a small change in freestream velocity. This can be described mathematically using a damping derivative. A numerical approximation of this damping derivative is useful in the root locus formulation employed here. It is constructed from the real part of the roots,  $\sigma$ , at two slightly different velocities,  $U_n$  and  $U_{n+1}$ .

$$\frac{d\sigma}{dU} \approx \frac{\Delta\sigma}{\Delta U} = \frac{\sigma_{n+1} - \sigma_n}{U_{n+1} - U_n} \quad (C.1)$$

Two velocity values, at  $n$  and  $n+1$  increments in the root locus development, are compared with the associated real parts of a root of interest. As the velocity increment is made smaller, a good approximation can be obtained for the damping derivative, and the approximation gives a numerical value to the degree of explosiveness of a root crossing the imaginary axis.

Table C2 presents the numerical damping derivative for some of the test points of the wind tunnel model. Collected in this table are data for selected sweep angles using a fiber kick angle of  $15^\circ$ . For each angle the value of the damping derivative is calculated using the velocity value just

Table C2 Wind Tunnel Model's Damping Derivatives

$\Lambda$ (deg)	$\frac{\Delta \sigma}{\Delta U}$ (rad/ft)
$\Lambda_k = -15^\circ$	
-15	- .31
-30	- .86
-45	- 1.46

prior to and the one at divergence. By comparing the damping derivative for the given geometries, the case with the smallest damping derivative at divergence is shown to be the sweep case of  $-15^{\circ}$ . The small damping derivative suggests that relatively large changes in velocity are required to observe significant changes in damping. This level of the damping derivative could appear in testing as vague responses around the neutral-stability velocity, and it is this geometry that demonstrated the vague test response. This correlation of predicted response versus test response reinforces the assumption that in the neighborhood of the imaginary axis the subcritical airloads of the Padé Approximants produce good sub-critical response predictions.

In summary the comparisons of the Padé Approximant solution with the wind-tunnel data show that this analytical technique can predict low-speed divergence instabilities as well as flutter. The sub-critical predictions of the damping derivative also suggest that the Padé Approximant airloads work well for lightly damped wing motion. These correlations provide some confidence in the Padé Approximant aerodynamics and their application to active control solutions of wing aeroelastic divergence and flutter.



## VITA

Kenneth Edward Griffin was born 24 September 1947, in Waco, Texas. He graduated from McGregor High School in 1965. He attended the University of Texas at Austin from 1965 through 1972 where he received both his Bachelor of Science (1970) and Master of Science (1972) degrees in Aerospace Engineering. He went on active duty in the United States Air Force with the Flight Dynamics Laboratory at Wright-Patterson Air Force Base, Ohio in June 1972. From there he entered the School of Engineering of the Air Force Institute of Technology in September 1976.

Permanent address: 1010 Tyler

McGregor, Texas 76657

END

DTIC

7-86